STRUCTURE, MECHANICAL PROPERTIES AND ACOUSTIC EMISSIONS OF STARCH EXTRUDATES

Submitted as part of PhD by

Andrew G Plews
Department of Materials
Imperial College London

Supervisors:
Prof Alan Atkinson, Imperial College London
Dr Scott McGrane, The WALTHAM Centre for Pet Nutrition

January 2008

ABSRACT

This project is concerned with food stuff extrudate acoustic emissions, mechanical properties and pore structure. The literature reviewed demonstrates pore structure is the probable driver of extrudate mechanical destruction acoustic emissions and mechanical properties and only fundamental acoustic properties should be investigated in this study.

Methods for structural characterisation (pore sizes, volume fraction porosity and pore wall thickness) were successfully evaluated. Three-dimensional X-ray Microtomography using a 3-D watershed algorithm and density analysis were the preferred methods. An Expansion Control Chamber (ECC) which varied the pressure differential across the extruder die face was used to control expansion having no effect on skeletal material properties. Volume fraction porosity and average pore wall thickness were found to be controlled by the ECC whilst pore size was not.

ECC samples showed fracture stress and elastic modulus to be primarily driven by volume fraction porosity (hence amount of solid material). Mechanical destruction acoustic emissions most probably originate from pore wall vibrations indicated by approximate modelling of pore wall vibrations. It is suggested as volume fraction porosity decreases the structure changes from primarily struts to primarily membranes having clear impact on acoustic frequency spectra with struts vibrating in the frequency region of 1200-2000Hz and membranes vibrating at 3000-4300Hz (for this skeletal material). Crispness has been linked to mechanical destruction acoustic emission ring down count.

These relationships mean it is possible to control, to some extent, mechanical properties and acoustic emissions through extrusion expansion hence pore-structure. However, if pore structure is varied via standard extrusion parameters (i.e. not using the ECC) skeletal material will also change. Account must be given to this. Future work should consider the effect recipe and extrusion process parameters have on skeletal material and ultimately acoustic and mechanical properties. The sensory impact of achievable acoustic differences should then be considered.

CONTENTS

List of Figure

List of Tables

1. INTRODUCTION

There are many foamed products within the food industry. One process by which these are created is starch based extrusion resulting in solid biopolymer food foams. This is a continuous process and produces products ranging from snacks and breakfast cereals, to pet food and biodegradable packaging materials (Campbell and Mougeot 1999; Fang and Hanna 2000; Trater, Alavi et al. 2005).

Internal structures of these biopolymer foams (extrudates) are of great importance for their physical properties (such as density, acoustic emissions and mechanical strength), which in turn influence important product attributes such as sensory texture (Wilkinson, Dijksterhuis et al. 2000; Duizer 2001; Van Vliet 2002). Textural properties are thought to be important quality indicators contributing to consumer acceptance, as well as the identification/categorisation of food. Schiffman (Shiffman 1977) showed that by blending food products the lack of structure, and hence sensory texture, resulted in only 40% of the food products being identified through flavour, and aroma alone. Sensory texture is the texture as perceived by the eater. It will be perceived by a combination of visual, tactile, kinaesthetic and auditory senses (Dacremont and Colas 1993) and has been widely studied within the food science community. Much of this previous work has focussed on quantification of mouth feel by a trained sensory panel and mechanical testing. However, importance has been placed on the contribution of acoustic emissions to texture.

Auditory senses have been studied in relation to texture for many years, with the idea initially introduced by Drake (Drake 1963) in 1963 to take texture study to the next level. They have never been studied as product attributes in their own right, but much work has shown texture to have an acoustic component. If upon biting a product the expected sound is not emitted, it can be hypothesised a judgement of product quality will be made. This demonstrates the probable importance of the acoustic emission.

The ultimate aim in texture based research is to understand the links between texture-related mechanical tests, acoustic emissions as produced during mechanical destruction, product mastication acoustic emissions and sensory texture. It can be hypothesised that the linking factor for all these product variables is the internal structure of the extrudate. For this reason characterisation of their pore structures is an important area of study.

The immediate objective of this project is to understand product structure and its characterisation, combined with the links to extrudate acoustic emission as created during mechanical destruction. This basic understanding will make work on the more complex sensory/mastication acoustic emissions more effective in later projects, as well as allowing for easy discussion of the links between mechanical measures and acoustic emissions through internal extrudate structure easier. If acoustic emissions are well understood it will be possible to design products to have a specific sound (Piazza, Gigli et al. 2006).

The report will begin with a literature review of relevant areas. Work that has been conducted on sensory/mastication acoustic emissions will be reviewed if considered directly relevant to the understanding of mechanical destruction acoustic emissions. More specific aims and objectives for subsequent work will be developed through the review and further discussion/introduction presented then. The project is sponsored by The WALTHAM Centre for Pet Nutrition.

2. LITERATURE REVIEW

The literature review will be separated into three major sections; Food Industry Acoustics (2.1), Structural Characterisation (2.2) and Extrusion Expansion (2.3).

2.1. Food Industry Acoustics

Studies have looked at the contribution of acoustic emissions to sensory texture and their relationship to force-deformation behaviour of material, as well as using acoustics to gain a quantitative measure of texture. Only work relevant to this project will be discussed, hence work focussing on sensory perception will not be included unless deemed important.

Destruction of a dry product produces acoustic vibrations in the surrounding air. These vibrations are propagated by alternate regions of compression and rarefaction moving through the air. The amplitude of the displacement of the air molecules is proportional to the amplitude of the acoustic emission (Speaks 1999). It could be thought that acoustic emission amplitude is related to stresses applied during destruction. That is, the greater the applied force at fracture, the greater the amplitude of the acoustic time signal.

Recording the acoustic emission during destruction results in a sound pressure wave-form. This wave-form can be further analysed, including transformation to the frequency domain. Some studies have non-destructively measured food texture through the amplitude of penetrated acoustic signals (Juodeikiene and Basinskiene 2004), however, this is beyond the scope of this project.

2.1.1. Sound pressure wave studies

An example of a sound pressure wave-form can be seen in Figure 2.1. The sound pressure wave will also be termed the acoustic wave in this report. Many different acoustic properties have been considered by different authors within food science, of which their work has been reviewed here. This includes aspects of the signal not directly taken from the acoustic wave. In many of these papers the acoustic data were being related to a sensory attribute.

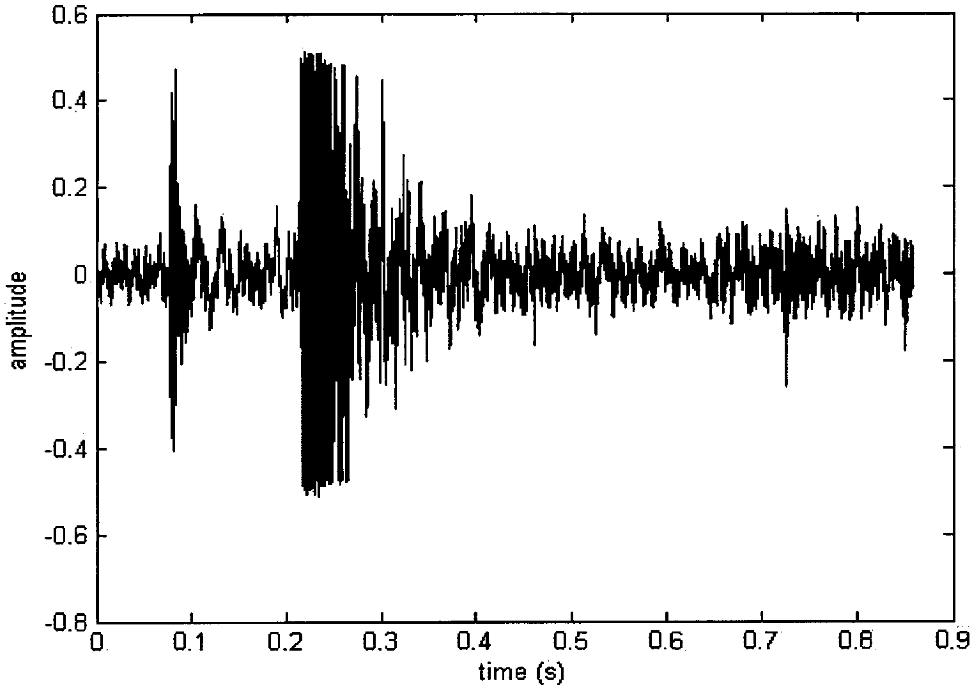

Figure 2.1: An example plot of a sound pressure wave (acoustic wave). This is taken from the mechanical destruction of an extruded starch snack product.

Chen et al. (Chen, Karlsson et al. 2005) looked at maximum sound pressure and number of acoustic instances for different biscuits. There work was related to sensory data but they demonstrated that for each detected acoustic event there was a simultaneous drop in compression forces. This is as would be expected.

Additional work has previously considered maximum sound pressure. Kapur (Kapur 1971) showed maximum sound pressure increased for wafers as they went from soggy to dry. Drake demonstrated the same for the controlled biting of bread as degree of toasting increased (Drake 1963). Both studies showed frequency of acoustic instances and duration of acoustic emissions held no important information with regards product changes.

Mechanical destruction instruments have been used to gain more objective sound emission data files (Mohamed, Jowitt et al. 1982; Seymour and Hamann 1998; Taniwaki, Hanada et al. 2006). Taniwaki et al. (Taniwaki, Hanada et al. 2006) used a conically tipped probe with a piezoelectric sensor attached to it. They assumed vibrations from sample fracture would be transmitted through the probe and calculated the lowest resonance of the probe, using standard equations, to be much greater than those recorded. They demonstrated signal amplitude reduced over time (10 days) for pear samples.

Work conducted by Seymour and Hamann (Seymour and Hamann 1998) considered mean sound pressure and total sound energy. In order to obtain the acoustic signal a compression test was performed inside an anechoic chamber. Calibrated microphone voltage levels were used to measure acoustic pressure.

The study found potato chips with lower water activity had higher mean sound pressure and sound pressure level. Total signal energy did increase as water activity decreased; however, it was less than with mean sound pressure and sound pressure level. The sound recordings were sensitive in the frequency range 0.5-3.3kHz. They believed, with no scientific evidence, this to be the important frequency range.

Mohammed et al. (Mohamed, Jowitt et al. 1982) studied the equivalent continuous sound level. This was calculated using a statistical distribution analyser to describe the time each acoustic signal remained in 5dB steps. Equivalent continuous sound level was calculated from this. Their study, again looking at water activity, showed equivalent continuous sound level increased as water activity increased (for numerous sample types) with a co-efficient of regression, 0.701 (Mohamed, Jowitt et al. 1982).

Roudaut et al. (Roudaut, Dacremont et al. 1998) showed product acoustic emission intensity gradually decreased as water content increased up to 9%, at which point it drastically decreased. Other work reviewed showed similar results (Seymour and Hamann 1998; Gondek, Lewicki et al. 2006). This sudden decrease was attributed to a glass transition phenomenon in the solid (i.e. glass transition temperature becomes lower than the test temperature).

Further work has shown the maximum amplitude of the acoustic signature is linearly related to maximum stress (r = 0.90), while duration of the acoustic signal was most closely related to Young's modulus (r = 0.83) as analysed by snapping tests for brittleness of pasta (Al Chakra, Allaf et al. 1996). Acoustic-mechanical properties have been used in combination to describe differences in toasted bread (Piazza, Gigli et al. 2006) and starch extrudates (Cheng, Alavi et al. 2007).

2.1.2. Frequency studies

Frequencies can be studied by transforming sound pressure waves of an acoustic signal using a Fourier Transform, generally the Fast Fourier Transform (FFT) computer algorithm. Once in the frequency domain dominant frequencies and their intensities can be identified. An example of a frequency spectrum is shown in Figure 2.2.

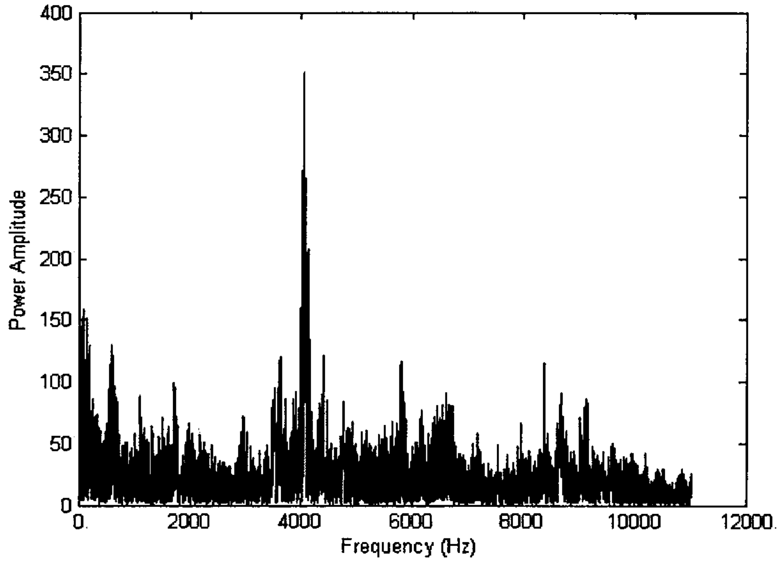

Figure 2.2: Example of frequency spectrum as achieved by a Fourier Transform of a sound pressure wave. This particular example is the Fourier Transform of the signal shown in Figure 2.1.

Much work has considered what spectral differences relate to product differences (Lee, Deibel et al. 1988; Lee, Schweiter et al. 1990; Dacremont 1995; Al Chakra, Allaf et al. 1996; McGrane 2002; Plews 2003). Most work was sensory based and concluded, without clearly defining spectral differences, that frequency spectra did hold important information. Work on starch extrudates concluded that important information was evident up to at least 5kHz (McGrane 2002; Plews 2003).

Liu and Tan (Liu and Tan 1999) further developed frequency analysis to gain more numerical information. Fourier Transforms are also used on images. Haralick et al. (Haralick, Shanmugam et al. 1973) proposed a method to extract numerous values from the Fourier Transform of images. This was further developed to extract information from acoustic signals (Liu and Tan 1999). These data were then used in sensory studies.

Time-frequency properties of acoustic signals have also been studied (Brochettie and Penfield 1992; Dacremont 1995; Cheng, Alavi et al. 2007). Techniques that can be used to study frequency over time have been developed for speech analysis (Brochettie and Penfield 1992; Cheng, Alavi et al. 2007). This analysis is similar to the Fourier Transform, and is known as the short-time Fourier Transform (STFT). The resultant data is in the form of numerous frequency spectra corresponding to different time bands of the acoustic signal. This data is difficult to objectively analyse (Dacremont 1995) and hence has not been tested further.

2.1.3. Structure and acoustics

The structure of a near dry elastic product will have a large impact on the acoustic emissions produced during mastication and mechanical destruction. Lillford (Lillford 2000) has shown, by looking at progressive breakdown of food during mastication, that texture is a property of microscopic structure, while molecular composition determines the material properties of the structural elements of food. No mention was given to macroscopic structure (size/geometry). Al Chakara (Al Chakra, Allaf et al. 1996) suggested acoustic emissions depend on several macroscopic and microscopic factors of the food.

Al Chakra suggested that microscopically the arrangement of cells, chemical bonds, impurities and pre-existing cracks, all affect destruction acoustic emissions (Al Chakra, Allaf et al. 1996). But, it has also been noted that there is little difference acoustically, or with the perception of human sensory 'crispness', between a crispy potato chip and an apple (Edmister and Vickers 1985), whilst there are large structural differences. The cells in an apple contain fluid, whilst the cells, or pores, in a potato chip are filled only with air. This work is concerned with products that have air filled pores.

Pores of extrudates can be considered as air filled cavities with brittle walls. Under an applied load the structure is stressed until a critical point is reached: the external forces cause the rupture of the brittle walls of the cellular structure which start to vibrate along with any fragments produced during breakage as they snap back to their original shape. It can be hypothesised this movement sets off vibrations in surrounding material and air creating an acoustic emission (Vickers and Bourne 1976; Plews 2003; Piazza, Gigli et al. 2006). This implies the acoustic emission is due to the rupture of one cell or many cells, hence all aspects of the cell may affect the acoustic emission produced during destruction. That is shape, size, wall thickness, wall strength, composition, etc.

It has also been hypothesized that acoustics emitted during mastication may be related to the elastic properties of the product up to the point of fracture (Sherman and Deghaidy 1978). This follows from general acoustic emission literature where frequency of vibration models include an elastic modulus term (Harris 1988). Some of the acoustic emission may also come from crack propagation (Lund 1998). Resonance of fracture pieces themselves or fully intact structural components may contribute to the acoustic emission. This has not been considered previously and investigation would be required to test this. However, it has been hypothesised that stress-energy released during mechanical testing is via new surface creation at weak yield points and acoustic vibration, with that vibration spreading through in-tact structural components (Chen, Karlsson et al. 2005).

Lee et al. (Lee, Schweiter et al. 1990) have provided evidence that loss of product structure reduces acoustic emissions. During mastication cell walls are continuously broken down and hydrated by saliva, reducing structure. Acoustic emissions are perceived as a maximum during the first bite and decline through mastication as structure is lost.

Little work has considered macroscopic structure, essentially product geometric properties. Work investigating the effects of extruded starch product diameter on the acoustic emissions produced during mechanical destruction showed there to be no obvious difference in frequency spectra (Plews 2003). Pore properties were indicated as key parameters but not tested.

Al Chakara has shown acoustic emissions change during the mastication process which is accompanied by dimensional change (W Al Chakra 1996). The report does not comment that, along with size, other product attributes such as structure will also be changing during mastication, as mentioned previously.

Much work has focussed on combinations of sensory textural tests, mechanical tests and acoustic signals from both mechanical destructions and mastication. It would seem product structure is the likely link between all these factors. The relationship between acoustic and instrumental (mechanical) measures is a complex area and basic understanding of mechanical failure and the resulting sound waves must be gained to truly understand the area (Tesch, Normand et al. 1996). Structural properties contribute to this failure and also impact upon product texture (Bouvier, Bonneville et al. 1997).

2.1.4. Other methods

One suggested but unused acoustic parameter is auditory density (Vickers 1985). Auditory density is a combination of acoustic frequency and acoustic intensity; increases acoustic frequency and increased acoustic intensity increase auditory density. It is a measure of the penetrating quality of the sound (Guirao and Stevens 1964).

Neural networks have also been used to analyse acoustic signal frequency data from various selected snack foods (Srisawas and Jindal 2003). The neural networks used 102 amplitudes as input for training and it was shown sensory crispness could be predicted 96-98% of the time. This demonstrates important information is held in the frequency data of the acoustic signals.

Fractal dimensions describe how well a fractal appears to occupy a space and characterises the geometry or jaggedness of lines (Barnsley 1993). Recent work has looked at fractal dimensions to quantify sound pressure waves. Whilst useful information was obtained from the fractal dimension it is not an actual physical acoustic parameter.

2.1.5. Mars Inc.

In their initial stages of acoustic research Mars Inc., in conjunction with Food Science Australia (FSA), ran a small scoping project (McGrane 2002). This work will be reviewed here along with a project that was conducted as a direct result of that work (Plews 2003). Please note, this work is not available in the public domain and is contained within confidential reports to Mars Inc. so all major results pertinent to this thesis are reproduced here.

The initial Food Science Australia project developed a method for the capture and analysis of mechanical destruction acoustic emissions and investigated whether mechanical destruction acoustic differences were seen for different extrudates. This work will now be reviewed, followed by the additional project.

The mechanical destruction methodology, in order to gain a loud acoustic emission, used a special attachment - the blade set attachment with a blunt edge as shown in Figure 2.3 (also shown diagrammatically in Chapter 3, Figure 3.6). This set-up gave an audibly louder 'crushing' sound. It was speculated this attachment produced both compressive and three-point bend forces.

For the mechanical destruction methodology, the number of extrudates, extrudate position, microphone position and all other test settings were standardised, but no work conducted to justify the chosen settings. Justification of these settings will be required for full development of the methodology and interpretation of results. Ten repeat recordings were taken for each test.

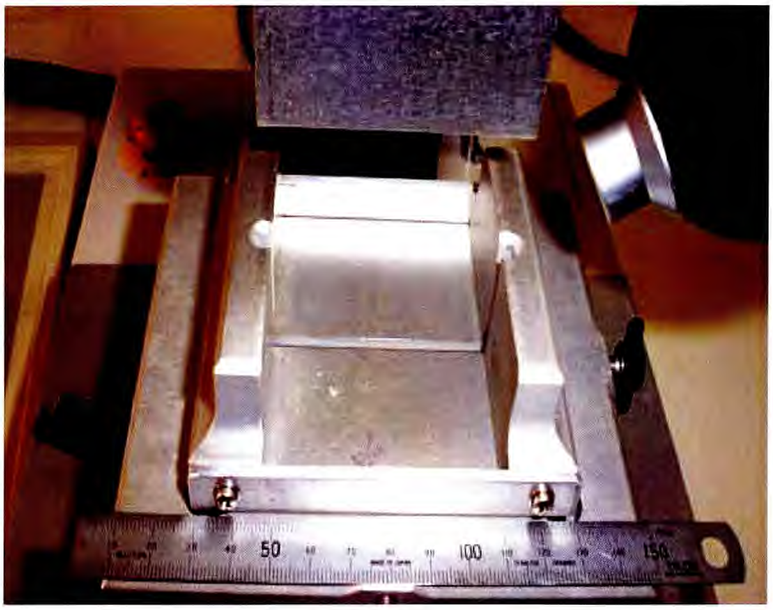

Figure 2.3: A picture of the blade set attachment with a blunt edge. Taken from (Plews 2003).

Analysis of acoustic signals was done using a Fourier Transform and considering the frequency range 1000-5000Hz. It was conjectured that below 1000Hz was machine noise and, due to the acoustic emission recording sample rate, 5000Hz was near the maximum frequency that could be resolved. To discount frequencies outside this range more scientific evidence is required as it may hold important spectral information.

Figure 2.4 shows the frequency spectra for 10 extruded different products used in the work. It is clear there are seven distinct peaks at the same frequencies for each product. It was suggested a sample's acoustic signature could be described by seven amplitudes relating to these frequencies. This seems reasonable, however it must be remembered this work only considered frequencies up to 5000Hz.

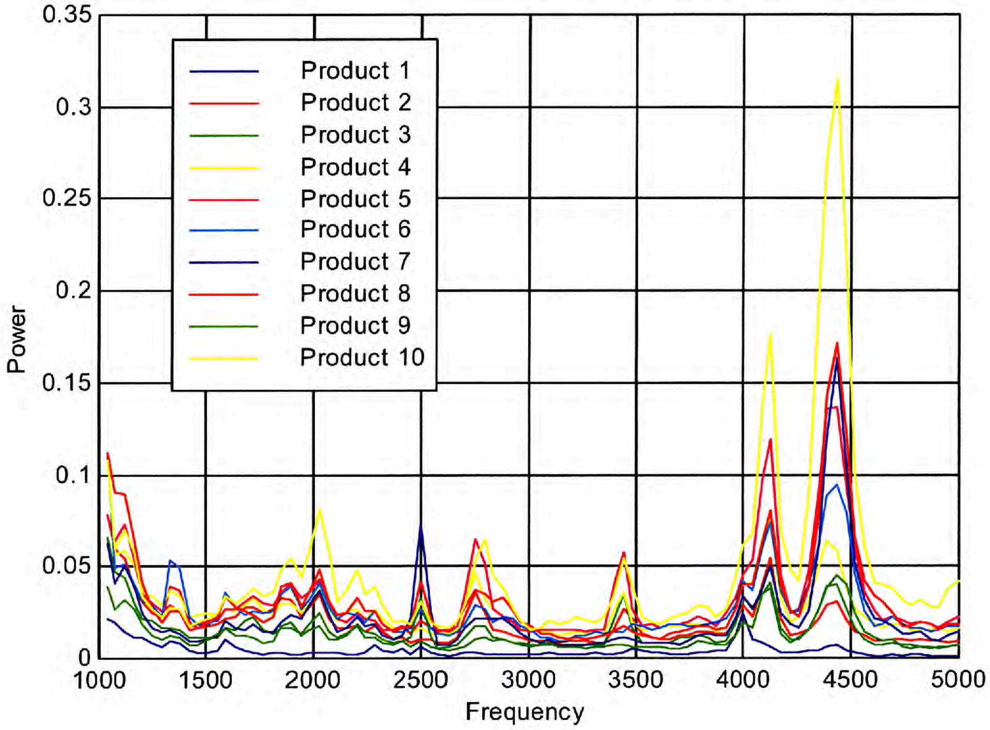

Figure 2.4: Raw frequency spectra of mechanical destruction acoustic emissions for 10 of the products used in the FSA work (McGrane 2002).

The work showed acoustic differences did occur in the frequency spectra. Using correlation analysis, similarity analysis and fuzzy c means clustering products were grouped according to their acoustic signature. Each technique gave similar clusters of products. It was not clear if acoustic differences were due to the product, different excitation of the test rig or both.

In a further project to above (Plews 2003), still conducted by Mars Inc., the effect of extrudate diameter on acoustic emission frequency spectra was considered. Samples were produced to have everything constant except diameter, with this ranging from 5.5mm – 17.5mm. The same methods for capture and analysis as above were used, with the difference that a frequency range of 150Hz – 12000Hz was considered;

12000Hz is the upper audible frequency for an adult (Briggs 1967) whilst below 150Hz was assumed DC levels in equipment and mains 'hum'.

The frequency spectra for the five different diameter extruded products can be seen in Figure 2.5. The results showed all five products to have the same frequency peaks and similar amplitudes with the exception of the peak at approximately 4000Hz for the 5.5mm product, the bottom spectra in Figure 2.5. Further investigation showed this product to have larger pores than other samples. It was hypothesised the difference was due to this porosity rather than sample diameter.

The work concluded sample diameter had no effect on acoustic emission frequency spectra and information was held in the signal up to 12000Hz.

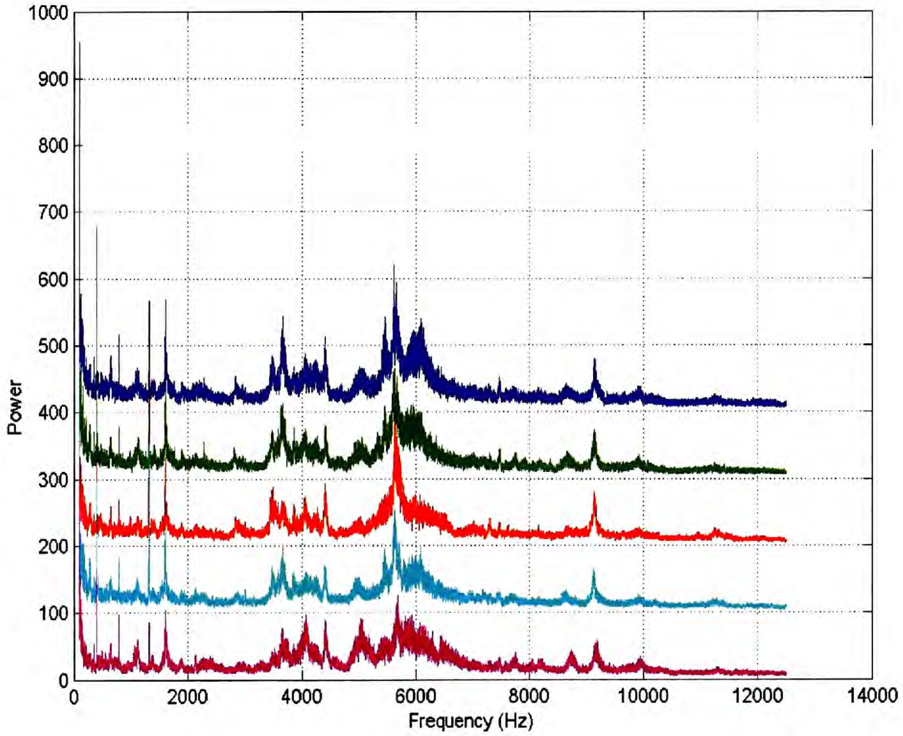

Figure 2.5: The average frequency spectra for the five different diameter products. The smallest product is at the bottom and largest at the top, with each being offset by 100 on the y-axis (Plews 2003).

2.2. Structural Characterisation

The literature reviewed in section 2.1 suggested the pore structure of the product to be important with regard to acoustic emissions. For this reason it is important to have robust and reliable techniques for structural characterisation.

Numerous techniques have been used to characterise internal structure and porosity of porous food stuffs. Imaging methods used include cross-sectional optical scanning (Babin, Della Valle et al. 2005), video imaging (Liu, Chuah et al. 2002), nuclear magnetic resonance imaging (Ablett 1992; O'Brien 1992; Babin, Della Valle et al. 2005), microscopy (Kalab, Allan-Wojtas et al. 1995; Hermansson, Langton et al. 2000; van Dalen, Blonk et al. 2003) and X-ray micro-tomography [XMT] (van Dalen, Blonk et al. 2003; Lim and Barigou 2004; Babin, Della Valle et al. 2005; Falcone, Baiano et al. 2005; Trater, Alavi et al. 2005). Mercury porosimetry has also been used (Karathanos and Saravacos 1992) to characterise the sizes of apertures between interconnected pores.

Of these techniques XMT shows the most promise for structural characterisation, a view generally held within the food engineering community (van Dalen, Blonk et al. 2003). XMT is a non-destructive 3-D imaging technique. Radiographs of the sample are taken at small angular increments over 180° of sample rotation. A computer algorithm then deconvolutes the set of radiographs to create a 3-D representation of the internal structure in which different densities are shown by different contrasts within the image (Stock 1999). Resolution of a few microns can be achieved with high resolution XMT units (Stock 1999; Farber, Tardos et al. 2003). The three-dimensional image can be used for qualitative discussion, visualisation of internal structure and structural quantitative analysis (van Dalen, Blonk et al. 2003). This makes it an ideal technique for characterisation of internal pore-structure.

When characterising (food) structure the main features of interest, including for this work, are pore size distribution, void fraction and cell wall thickness. XMT has been used to study pore size distributions of foods by many authors. However, this is only straightforward for closed cell foams (van Dalen, Blonk et al. 2003; Lim and Barigou 2004), which have also been successfully studied by integrating across a sequential stack of 2-D images (van Dalen, Blonk et al. 2003; Lim and Barigou 2004; Falcone, Baiano et al. 2005; Trater, Alavi et al. 2005). Figure 2.6 illustrates how 2-D imaging gives only an apparent pore size and does not give reliable information on connectivity between pores. That is, the position of the slice through the pore affects its perceived size and/or the slice may cut through two connected pores taking them to be one larger pore. The first issue can be overcome by integrating 2-D image stacks; but the second problem still remains. Extrudates have predominantly open porosity (Hicsasmaz and Clayton 1992; Bhatnagar and Hanna 1996; Jones, Chinnaswamy et al. 2000) and therefore it is important to be able to study pore connectivity by segmenting connected pores (i.e. distinguishing pore cavities and interconnects).

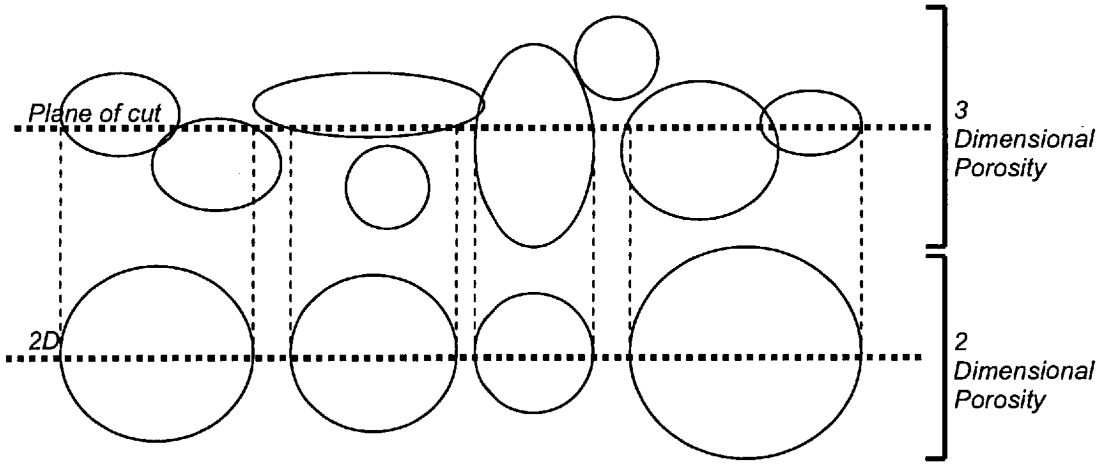

Figure 2.6: Schematic illustration of the appearance of a 2-D slice through a 3-D porous structure.

Granulometry is a morphological technique that can overcome such problems and has been used in both materials science (Elmoutaouakkil, Salvo et al. 2002; Maire, Elmoutaouakkil et al. 2003; Maire, Fazekas et al. 2003) and food engineering (van Dalen, Blonk et al. 2003). This technique retrieves cell size distribution directly from the image taking the smallest dimension if cells are not equiaxed (Maire, Fazekas et al. 2003). However, the method does have some draw backs. Granulometry needs distinct boundaries and a volume of interest must be specified if a sample has an irregular shape. This is not appropriate for extrudates, with which this work is concerned, due to the inhomogeneous nature of the porosity over their cross section. Furthermore, as granulometry retrieves only pore size distribution, no information is available on the apertures of interconnected pores or individual pores themselves.

A method for segmenting interconnected pores, which has been applied to engineering materials, is the use of a 3-D watershed algorithm (Atwood, Jones et al. 2004; Jones, Lee et al. 2004), watershed segmentation being a technique regularly used in 2-D analysis (Sun, Yang et al. 2004; Tek and Aras 2004). Application of the watershed algorithm results in a 3-D image in which interconnected pores are segmented. True pore sizes and shapes can be taken directly from the resulting segmented image. The sizes of the interconnected pore apertures, if required, can also be gained from this technique.

Cell wall thickness distributions have been obtained from XMT images using granulometry in both food engineering (van Dalen, Blonk et al. 2003) and materials science (Maire, Elmoutaouakkil et al. 2003; Maire, Fazekas et al. 2003). However, the most important characteristic parameter is the average cell wall thickness and this can be obtained from image analysis of two-dimensional slices (Trater, Alavi et al. 2005). Average cell wall thickness can also be taken from image analysis of scanned or photographic images of exposed internal extrudate surfaces. However, numerous slices can be taken through the sample volume using XMT and an average calculated. This is more likely to give accurate results than a single scanned/photographed surface.

2.3. Extrusion Expansion

Extrudate internal structure forms due to expansion during extrusion. As has been discussed in section 2.1 (Food Industry Acoustics) and 2.2 (Structural Characterisation) internal structure is the probable product characteristic linking mechanically measured texture and acoustic emissions, the areas of concern for this thesis; hence extrusion expansion is important to understand from an experimental control perspective.

Expansion during extrusion occurs due to a pressure differential across the die plate (Kumagai, Kumagai et al. 1993), with the inside of the extruder being at high pressure and the exit normally being at atmospheric pressure. This pressure differential causes water in the extruder dough to flash-off as superheated steam when it passes from high pressure to atmospheric pressure, resulting in expansion of the dough (Fan, Mitchell et al. 1994).

Control of expansion, hence pore structure, through the extrusion process has been studied by many authors. Expansion can be controlled by altering barrel temperature and water/steam addition (Owusu-Ansah, Van de Voort et al. 1983; Chinnaswamy 1993; Ding, Ainsworth et al. 2003; Thymi, Krokida et al. 2005), feed rate (Ding, Ainsworth et al. 2003; Thymi, Krokida et al. 2005), die nozzle geometry (Chinnaswamy 1993) and screw speed/configuration (Lee and McCarthy 1996; Ding, Ainsworth et al. 2003). During extrusion the starch undergoes different types of conversion, that being via mechanical and/or thermal degradation as shown in Figure 2.7. Adjusting extrusion parameters will affect the degree and type of starch conversion (Lai and Kokini 1990; Ryu and Walker 1995), which will in turn change the properties of the extrudate skeletal material. In Figure 2.7 pure states indicate those obtained through solely thermal conversion in excess water whilst alternate states describe those due to mechanical damage of the starch granule and/or starch polymer chain. Extrusion will produce some combination of the two conversion routes.

For this reason the effect of pore structure alone has not yet been studied. Furthermore, high density extrudates cannot be manufactured without compromising the degree of cook of the starch. To truly understand the effect of pore structure on mechanical properties, textural parameters, acoustic emissions, etc., a method to expand the product whilst affecting no other product characteristics must be developed.

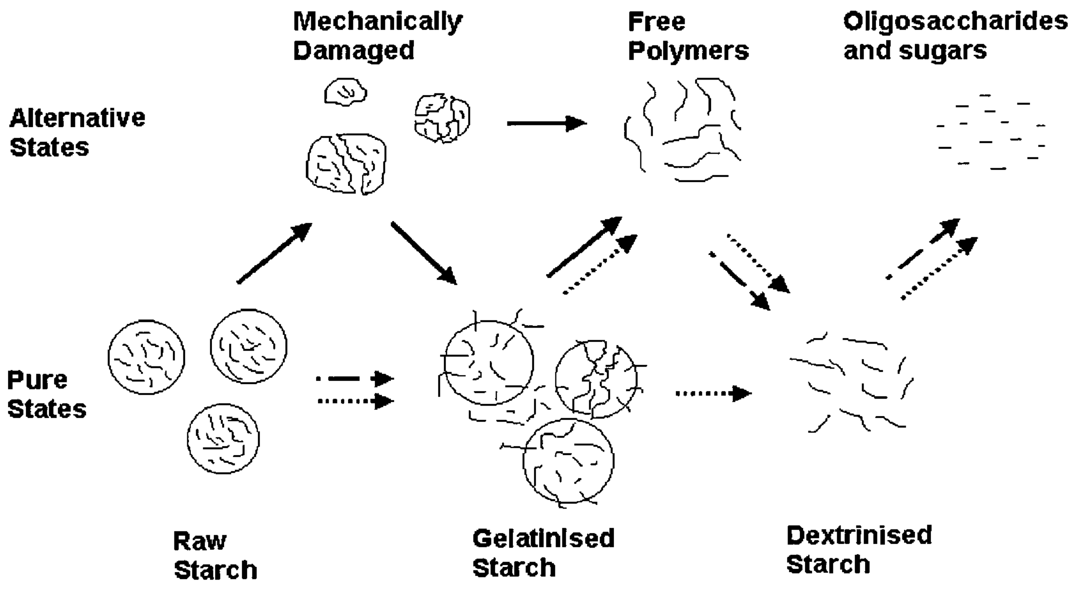

Figure 2.7: Possible starch conversion during extrusion – pure and alternative states created by mechanical and thermal degradation.

2.4. Literature Review Discussion

The work reviewed has shown many acoustic parameters have been studied in relation to food products. In some instances interesting results have been gained and in others simple and expected correlations have been found. The breadth of work does appear to result in some confusion, partly due to a lack of a fundamental understanding. It may be sensible to conduct immediate future research using fundamental acoustic parameters, such as frequency analysis, signal energy and maximum sound pressure, until a greater initial understanding is built. Furthermore initial stages should consider mechanical destruction acoustic emissions to gain a more objective understanding. Mastication acoustic emissions can be incorporated at a later date.

Initial stages of Mars Inc. work considered frequencies to 5000Hz, then later 12000Hz. It was shown information is held up to 12000Hz so should be included in future work. 12000Hz is the upper limit of an adults' hearing frequency range.

Mars Inc. work has also shown different texture/structure extrudates have different frequency spectra. This work used a set method for capturing the mechanical destruction acoustic emission, however to fully interpret results more investigation of this method will be required. It will be important to consider the origin of the peaks in the frequency spectra to ensure they are from the product and not the test rig, something not clarified in the report.

Some work reviewed implied internal (pore) structure as being responsible for differences in acoustic emissions. This relationship was not discussed in any depth and will form a good starting point for future work. It is not currently clear whether geometric properties affect the acoustic emission, but work has suggested it does not. Again, this can be clarified in the initial stages of future work.

Authors have also suggested acoustic vibrations come from the vibrations of the pore walls snapping back to their original position after fracture. This seems plausible, fitting with pore structure affecting acoustic emissions, and could form an interesting starting point for understanding what is vibrating hence creating the acoustic emission. Understanding what is vibrating will allow for the development of production methods capable of controlling product acoustic emissions. Testing whether vibrations are from pore walls could be done by modelling their vibration and comparing these model frequencies to those from actual samples. In order to conduct this work, methods for sample structural characterisation and varying sample pore structure whilst keeping skeletal material constant will be required.

The review made clear that pore structure is the probable link between mechanically measured texture, acoustic emissions and sensory texture. Varying sample pore structure whilst keeping skeletal material constant is also important for understanding this. Findings here may prove extremely valuable for follow-up projects and could show pore structure to be most important with regard to texture, it being the key feature controlling both mechanical and acoustic properties.

Reviewing structural characterisation literature found X-ray Microtomography to be the best technique currently available for structural characterisation, incorporating the use of a 3-D watershed algorithm to close the open porosity extrudates are known to have. Other parameters such as average cell wall thickness and volume fraction porosity are easily calculated from XMT images/data.

Hence, from the review five major objectives were decided;

1. Develop a fully tested mechanical destruction acoustic capture method including investigation of peak origins in the frequency spectra and sample geometry effect.
2. Develop methods for the characterisation of internal extrudate (pore) structure.
3. Develop and test a method for controlling extrusion expansion that has no impact on extrudate skeletal material properties.
4. Investigate the relationships between mechanical measures (real and texture), mechanical destruction acoustic emissions and pore structure.
5. Establish whether pore wall vibrations can account for mechanical destruction acoustic emissions by modelling their vibration.

Acoustic analysis conducted in achieving these objectives will use only fundamental acoustic parameters (maximum sound pressure, signal energy and signal energy build with time) and study frequencies up to 12000Hz, the limit of adult human hearing. This work will now be presented in subsequent sections beginning with Chapter 3, Methods and Their Development.

3. METHODS AND THEIR DEVELOPMENT

This chapter contains all standard methodologies used through the project as well as the development of required methodologies outlined in the previous chapter, those being mechanical destruction acoustic capture, structural characterisation and extrusion expansion control.

3.1. Material and Methods

Here you will find those standard methodologies used through the research.

3.1.1. Extrusion

Many extrudate samples were required for different phases of the work. All samples were extruded as discs on a Buhler BCTG-62mm twin screw extruder equipped with full metering facilities and read out logs. This included five temperature readings at evenly spaced intervals of 248mm along the extruder barrel length. Temp 1 corresponds to the beginning of the extruder barrel whilst Temp 5 corresponds to that at the die face. Prior to extrusion the extruder water injection and solids feed rates were calibrated. Extrudate samples were collected after the process had been stable for 10 minutes. The proprietary extrusion feed recipe was the same for all samples and based on wheat with minor amounts of protein, vitamins and minerals and all the extrudates were coated with a fatty coating. The feed recipe can be seen in Table 3.1. Extruded rods were cut transversely to give finished disc samples having an approximate thickness of 6mm. Due to the extrusion process, the extrudates were not perfect discs and had a side on cross-section similar to that of the extrudate in Figure 3.9b. All extrudates were dried to 4.5 wt% moisture and then coated with a fatty coating. Unless otherwise stated extrudate moisture prior to drying was 20-21 wt%.

Table 3.1: The recipe as percentages used in the production of all extrudates through the report. Water is not included as this varied dependent upon the extrusion conditions and required product properties.

EXTRUDATE RECIPE	%
Wheat Flour	33.12
Maize Meal	33.12
Poultry Meal	19.34
Sun Flower Oil	2.30
Other (Vitamins etc)	4.12
Fatty Spray Coating	8.00

What was perceived as a 'standard starch extrudate' was used for mechanical destruction acoustic capture methodology development/validation. This was extruded under standard conditions and will be referred to as the standard extrudate through the report. For development of structural characterisation methodologies two extrudates of very different porosity were produced. Concern was not given to keeping other parameters, such as structural bonding, constant whilst changing the porosity as the sole aim was to produce structurally/acoustically different samples. The range in porosity was achieved using operational knowledge of product expansion immediately following extrusion. One sample used extrusion conditions to gain high expansion and will be referred to as the porous extrudate whilst the other used conditions to gain low expansion and will be referred to as the dense extrudate. Note that the term "dense extrudate" does not imply zero porosity, but that minimal additional porosity has been introduced by post-extrusion expansion.

One series of experiments involved testing the effect of product diameter alone. Extrudate internal structure had to remain constant, that being extrudate porosity and degree/type of cook; hence skeletal material. Degree and type of cook are dictated by the mechanical to thermal energy ratio (SME:STE) of the extrusion process (McGrane 2000). Extrudate porosity is controlled by extruder expansion which is a manifestation of SME:STE and die hole properties. SME:STE ratio is also affected by die hole properties.

Total die hole surface area affects both expansion and SME:STE. Other die hole properties have a comparatively negligible effect (Guy 2001). Therefore the total die hole surface area was kept essentially constant, which should result in different diameter products having the same internal structure and skeletal material.

SME is calculated from extruder read-out logs as;

$$SME = \frac{screwspeed \times torque}{throughput} \qquad [3.1]$$

Where SME is specific mechanical energy (kWh/tonne), screwspeed is screw revolutions per minute, torque is that applied by the extruder motor (kNm) and throughput is amount of dough exiting the extruder (tonne/hour). STE is calculated via;

$$STE = \frac{\partial t.(((m_s c_s) + ((m_w + m_{wa}).c_w)))}{100} . \frac{1000}{3600} \qquad [3.2]$$

Where m_w is water percentage in dry feed (%), m_{wa} is moisture addition to process compared to dry feed (%), m_s is solids in dry feed (%), c_s is specific heat capacity of solids (taken as $1.5 kJkg^{-1}K^{-1}$ for petfoods), c_w is specific heat capacity of water (4.2 $kJkg^{-1}K^{-1}$) and δt is temperature increase between cold meal and pre-conditioned meal.

Extruder operation restrictions and the maximum number of die holes being four resulted in the range of die hole sizes as shown in Table 3.2. During production all other extrusion parameters (water, steam, temperature profile, screw speed, etc.) remained constant. Through the report the different products will be referred to by their original die hole size, namely 5mm product, 6mm product, 7.2mm product and 10mm product.

Table 3.2: Details of die hole diameters and the total die hole surface areas as used to create extrudates with varying diameter but same internal structure.

Product	5mm Product	6mm Product	7.2mm Product	10mm Product
Die Hole(s) Diameter (mm)	4x5.00	3x6.00	2x7.20	1x10.00
Total Die Hole Surface Area (mm^2)	78.55	84.83	81.43	78.54

One further extrusion method required, as identified during the literature review, was that of expansion control whilst keeping all skeletal material properties constant. It can be hypothesized that expansion control, independent of extrusion conditions, might be achieved by varying the pressure differential across the extruder die plate. A sealed knife housing could be used inside which the pressure can be regulated. By changing the sealed knife housing pressure the boiling point of water as it exits the extruder will change, altering the amount of flash-off, hence expansion; a higher sealed knife housing pressure will increase the water boiling point, producing less flash-off/expansion.

An Expansion Control Chamber (ECC), supplied by Andritz Sprout GmbH, operating on this principle was obtained. The ECC was placed after the die plate and the extrusion setup can be seen in Figure 3.1. Pressure of the sealed knife housing (to be termed ECC pressure from here on) was regulated through application of compressed air or vacuum via the inlet/outlet valves. Pressure inside the sealed knife housing was maintained by a pressure resistant air lock which allowed product to be continuously removed. The sealed knife housing was equipped with a pressure transducer to log ECC pressure throughout extrusion.

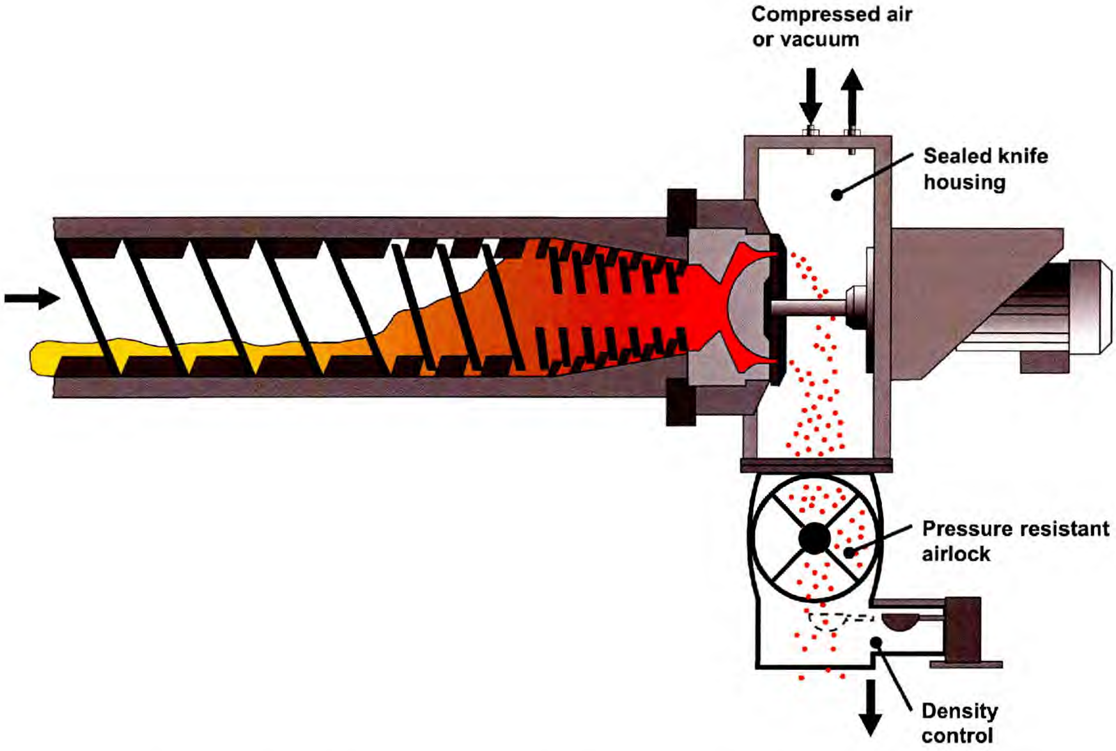

Figure 3.1: Extrusion system with the addition of an Expansion Control Chamber in front of the die face.

Initial tests showed that the ECC pressure was unduly influenced by the pressure resistant air lock. A second pressure resistant air lock, in addition to the first and not detailed in Figure 3.1, rectified the problem resulting in stable ECC pressures from 200 to 2300 mbar.

Eight sample sets were extruded using the same extruder settings (screw speed, feed rate, moisture, etc.). The first five sets of samples were extruded using ECC pressures of 200 (EEC1), 775 (ECC2), 1450 (ECC3), 1950 (ECC4) and 2300 (ECC5) mbar. After shutting-down and starting-up the extruder a further three sets of samples (replicates) were extruded using the same extrusion conditions as previously and repeating ECC pressures of 200 (ECC6), 1450 (ECC7) and 2300 (ECC8) mbar. Sample codes, as may be referenced through the thesis, are given in brackets after the quoted pressure. As well as discs extruded rods were collected for each ECC setting (i.e. not cut transversely) for elastic modulus measurement (see later section 3.1.5.2).

Extrudate samples created for comparison to each other were stored, packaged and transported identically after production until sample analysis to ensure effects such as moisture migration and staling were constant for all products. All sample analysis was conducted with the extrudate in its finished product state, bar that of elastic modulus measurement, meaning no additional preparation was required.

3.1.2. Off-shelf

In some instances food product extrudates as purchased in the supermarket were used. Two products were used and will be described as STD 1 and STD 2.

3.1.3. Ceramic

Ceramic materials were also used in the mechanical destruction tests to generate acoustic emissions for comparison with food products. The two alumina ceramics used were a solid disc and a large foam disc. The large foam discs were all produced to have the same pore structure, made of the same material and had a 20mm diameter. The solid ceramic discs were made identically and had a 10mm diameter.

3.1.4. Mechanical testing

Mechanical testing was conducted using standard food industry texture methodologies and standard material science techniques to gain elastic modulus.

3.1.4.1. Texture

Texture analysis methodologies developed by Mars Inc. (McGrane 2004) were used. Mechanical tests were conducted on a TA.HD machine supplied by Stable Micro Systems (UK). Data acquisition and analysis was done with Texture Expert Exceed software provided with the machine. This software plots a force-time curve for the test and subsequently analyses the data.

The parameters taken from the force-displacement curves, an example of which can be seen in Figure 3.2, were maximum nominal stress (i.e. applied load at fracture divided by sample cross-sectional area normal to load), number of peaks in the force-displacement curve normalised for (i.e. divided by) compression distance [using a peak definition of 20g from the maximum in question to the proceeding minimum] (crispness 1) and ratio of linear distances [length of actual curve divided by length of smoothened curve] (crispness 2). Figure 3.2 details the actual curve (black line) and smoothened curve (red line) which is created via an in-built function of the Texture Expert Exceed software. Implications of using the word crispness should be ignored and the definition given focus. The tests used a 50mm diameter cylinder probe. A test speed of 1mms^{-1} and strain level of 80% was used as this has been shown to provide all fracture information without excessive compression between probe and plate.

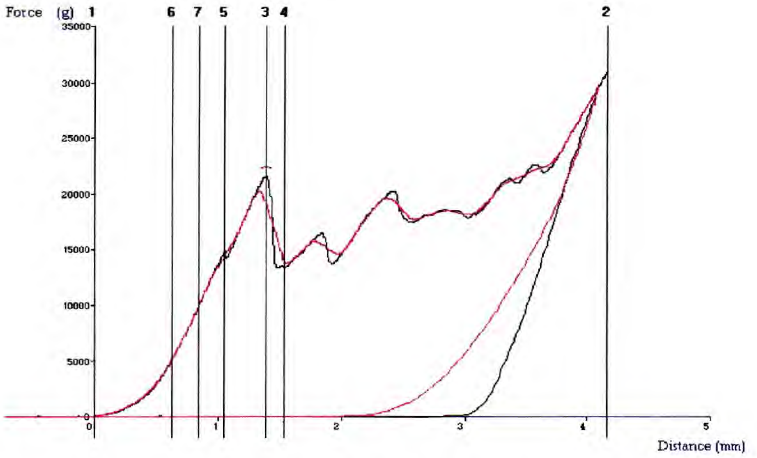

Figure3.2: Example force-displacement curve for an extrudate. The black line is that of the actual fracture and red line that as smoothened by the software for calculation of crispness 2.

3.1.4.2. Elastic modulus

Two methods of measuring elastic modulus were used, one being a four-point bend test and the other an impulse excitation acoustic technique.

The impulse excitation technique used the Grindosonic MK5 frequency meter. A light external mechanical impulse is used to excite the test object and the natural frequency of the subsequent vibration is measured. The excitation is done in such a way as to favour a desired mode of vibration using a transducer to pick up the frequency of that vibration. Both bar and disc samples can be used. The Grindosonic computer software coverts frequency of vibration to elastic modulus, E, using sample geometry (size and shape) input by the user.

Grindosonic tests were conducted on both bar and disc samples, and supported in such a way as to promote a desired vibration mode as shown in Figure 3.3. The frequency for vibration of the fundamental flexural mode will be obtained for the bar sample and disc sample when supported as in Figure 3.3a and Figure 3.3b respectively. Disc samples can also be supported as detailed in Figure 3.3c to promote the torsional mode of vibration. When torsional and flexural modes of vibration are excited for the disc sample Poisson's ratio, υ, and elastic modulus, E, can be calculated.

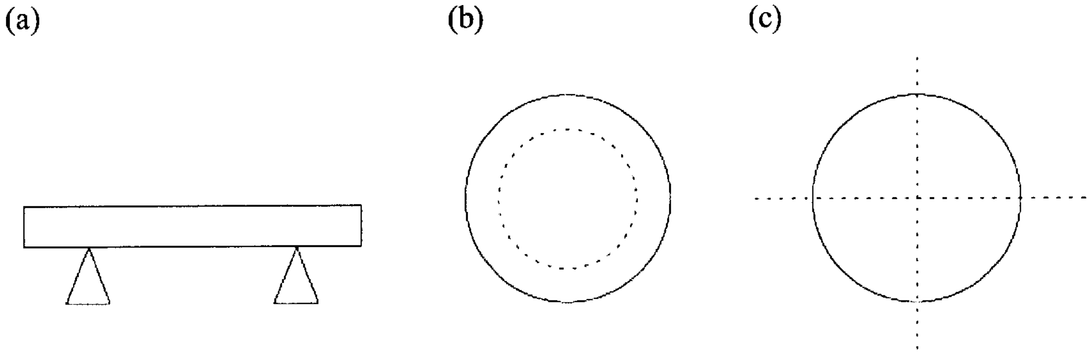

Figure 3.3: Sample support when using bar and disc samples for the impulse excitation technique. (a) is the bar, (b) the disc flexural mode and (c) the disc torsional mode.

Four-point bending was conducted on a Hounsfield 20K-C mechanical testing machine (Hounsfield Test Equipment, UK) capable of applying a force of 20,000N. Elastic modulus, E, is taken directly from the force displacement response from a bar sample using the equation (British Standard BS EN 843-2 2006);

$$E = \frac{PD^2}{Jy}\left(\frac{S_1}{2} - \frac{S_2}{3}\right) \quad \text{and} \quad J = \frac{h^3 d}{12} \qquad [3.3]$$

where S_1 is the distance between the outer loading rollers (22 mm), S_2 is the distance between the inner rollers (11 mm), h is the height of the specimen (5 mm), d its width (approximately 15mm with slight variation due to production technique), P is the load and y is the displacement. The displacement is the relative displacement of the upper and lower rollers, as seen in Figure 3.4, and was measured by a linear displacement transducer connected between the upper and lower parts of the loading jig. To ensure none of the measured displacement was due to compression of the test rig itself the experiment was run using a large 50mm height (and hence non-bending) steel sample. To the maximum forces seen during extrudate four-point bending (60N) no displacement was registered by the transducer. This shows there is no compression of the test rig itself during extrudate testing. The four-point bend rig is shown diagrammatically in Figure 3.4. Friction was minimised by using free rollers located in grooves as specimen support points. A test speed of 0.05mm/min was used in all tests.

Due to the nature of the extrusion process, it is not possible to obtain bars of extrudate sample material directly from extrusion for either the impulse excitation method or the four-point bend test. Bars were fashioned from the extruded cylindrical ropes. A specially designed metal 'mould' and fine sand paper were used to obtain parallel contact surfaces of the bars. Initially samples were cut to length (gently) using a junior-hacksaw then one surface sanded flat. This prepared sample was placed in the metal mould, with the flat surface against the flat metal mould surface and sanded until the metal touched the sand paper producing parallel surface bars of 5mm height. Figure 3.5 shows both a picture and scale technical drawing of the metal mould. Discs as produced direct from extrusion were deemed appropriate for use in impulse excitation.

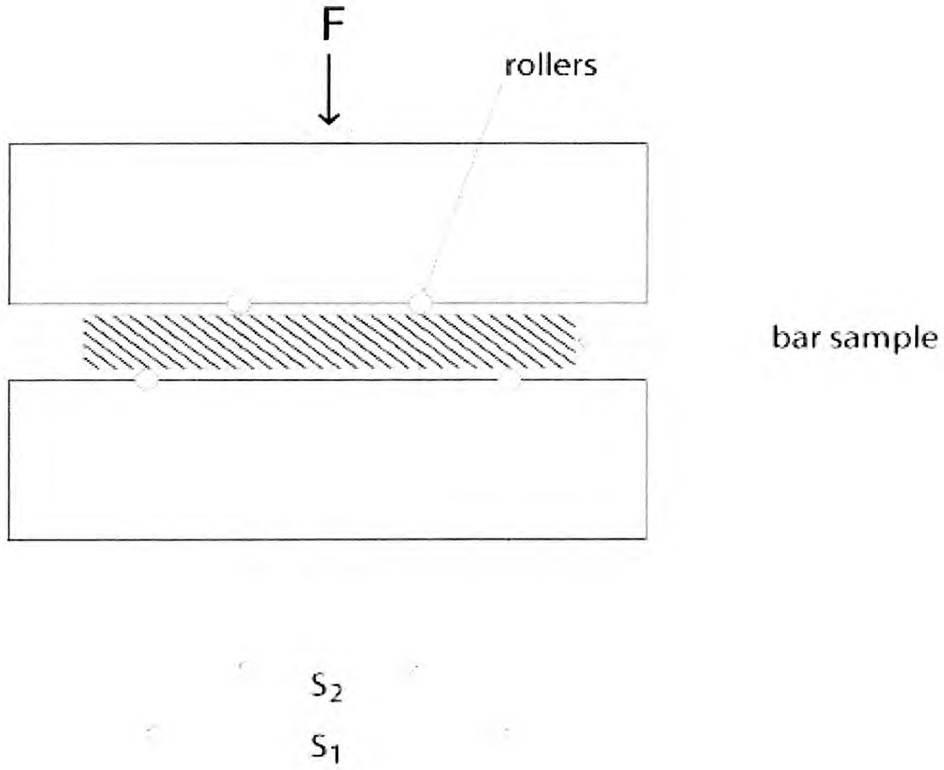

Figure 3.4: A diagram of the four-point bend test rig.

(a)

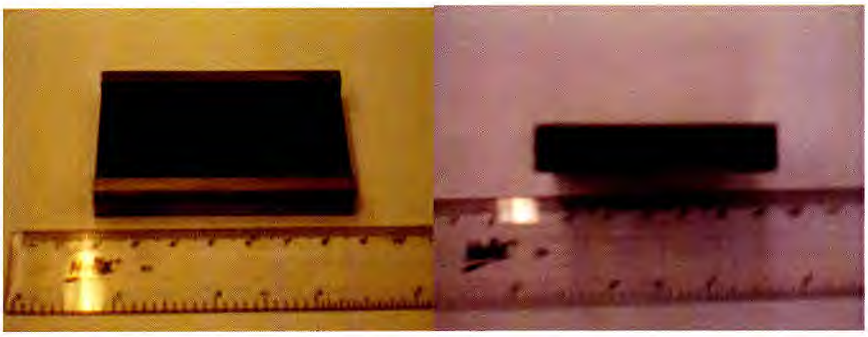

(b)

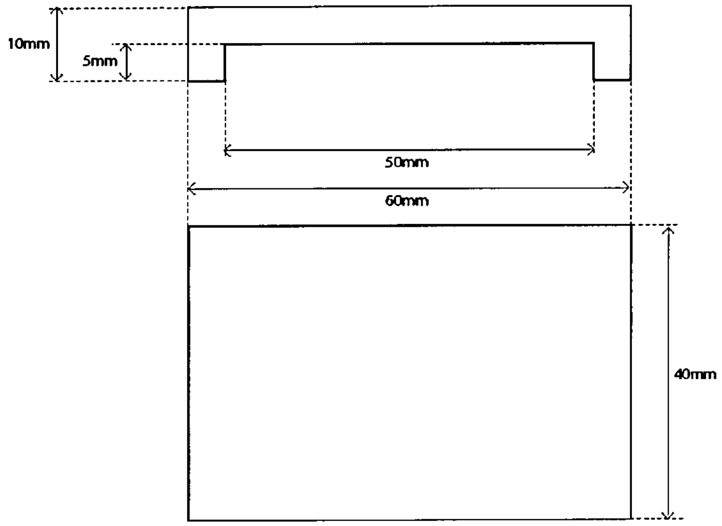

Figure 3.5: (a) A picture and (b) a technical drawing of the metal mould used to make bars with parallel surfaces from extruded cylindrical ropes. The technical drawing shows both elevation and plan views.

3.1.5. Acoustic capture and analysis (preliminary)

Later sections will discuss the development of the acoustic capture method and the subsequent signals analysis. However, for preliminary work a method had to be defined as presented here.

Analysis of microphone pressure signals was done using MatLab 7 [release 14] (and the standard in-built Fast Fourier Transform (FFT) function to give a frequency spectrum. The pressure amplitudes gained for the frequency spectra were squared to give values equivalent to energy. This is true because (assuming a plane wave);

$$I = \frac{{p_{rms}}^2}{\rho_o c_o} \qquad [3.4]$$

Where I is the sound intensity (Wm^{-2}) [a measure of sound energy], p_{rms} is RMS sound pressure (Pa), ρ_o is the equilibrium density of air (kgm^{-3}) and c_o is the speed of sound in air (ms^{-1}).

Ten repeats were recorded for each test and an average spectrum calculated. Recording used a Radio Shack sound level meter set to 70dB sensitivity. This can be considered a microphone that amplifies the signal. The microphone voltage readings are equivalent to sound pressure. However, this was not calibrated hence all units are arbitrary, but relative differences are meaningful. The recordings were done at 44100Hz sample rate in 16bit as .wav files using Cool Edit Pro 2.1 audio editing suite. The microphone had approximately constant sensitivity up to 12000Hz, the upper bound of the frequency range which was analysed.

3.1.6. X-ray microtomography

An entire extrudate disc was mounted on a rotating steel sample holder and imaged using a commercial XMT unit (Phoenix X-ray Systems and Services GmbH) for each sample. The resolutions of the reconstructed extrudate images were similar across all samples with voxel sizes ranging from 13.00μm to 16.25μm. This included excess volume from the sample edge. Details of the XMT process were presented in the literature review section 2.2, however a schematic showing the imaging through rotation and subsequent 3-D structure can be seen in Figure 3.6 – please note this is not an image of a sample produced for this work.

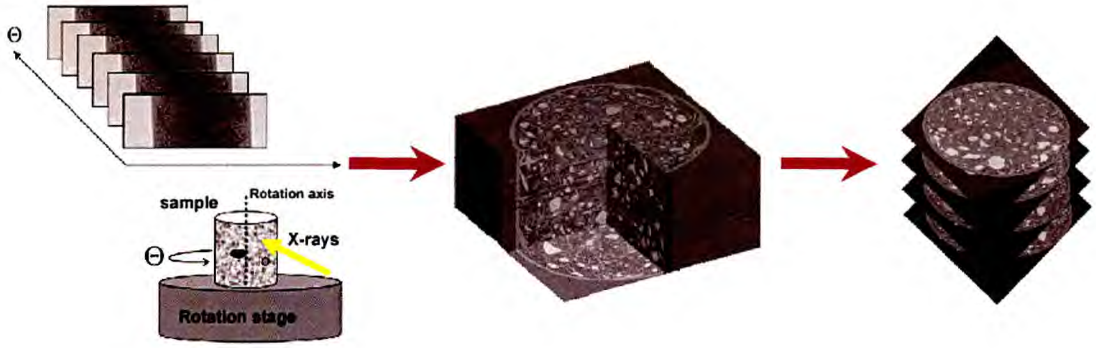

Figure 3.6: Diagram demonstrating the radiograph imaging at different sample rotations, subsequent 3-D reconstruction and 2-D image slices through the sample volume.

3.1.7. Pore size distribution

The interconnected regions were divided into recognizable cells by application of a 3-D watershed algorithm to a distance map. Watershed algorithms find the set of points in a function, considered as a height map, that bind regions in which water flows to the same final point; analogous to the watersheds of a river basin in geography. The algorithm used was developed by Mangan and Whitaker (Mangan and Whitaker 1999).

A median filter was first applied to the image to reduce any noise. The watershed algorithm was then applied to the entire sample image, including the external air space. The inhomogeneous nature of the porosity across the extrudate's diameter, as can be seen in Figure 3.7, means the entire extrudate requires analysis (refer section 2.2 for detail). The application of the algorithm followed the sequence (Atwood, Jones et al. 2004):

1. A threshold was applied to the 3-D image to classify each voxel as either pore or solid.

2. A dilation algorithm was used to grow the surrounding solid to the centre of each pore, noting the number of voxel steps required. The centroid of each pore filled last.
3. Using the centroids and the number of dilation steps as a distance map, a 3-D watershed algorithm (Mangan and Whitaker 1999) was applied to divide the image into individual pores.
4. Voxels with neighbours in two pores were then grouped and defined as apertures between these pores.
5. Pore volumes were obtained by counting the voxels (which were of known volume) in each pore. This gave the true pore volumes to a resolution equal to the voxel size (14.25μm^3 and 16.25 μm^3 for the two samples).
6. The largest pore was air external to the sample. This was removed from the data set.
7. Pore volumes were converted to equivalent spherical diameters for pore size distribution plots. Pore size distribution plots were constructed as both number frequency mm^{-3} and volume fraction (of the entire sample, excluding the external air).

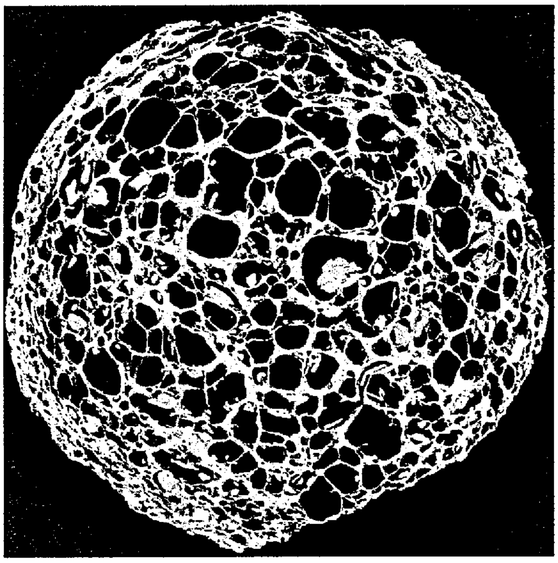

Figure 3.7: XMT 2-D slice of the porous specimen showing the inhomogeneous nature of the porosity across sample diameter. Brightness is proportional to density.

3.1.8. Volume fraction

Three methods of calculating volume fraction were used and compared. These were 2-D image analysis of evenly spaced XMT slices through the sample volume (an average across the image slices was then taken), 3-D image analysis of the entire sample volume, and density analysis using solid and bulk densities. Image analysis methods were calculated by pore area/volume divided by total sample area/volume. Two-dimensional image analysis was conducted using the DIPlib toolbox (Delft University of Technology, NL) running under MATlab, whilst three-dimensional analysis was done using Amira (Mercury Computer Systems).

The equation for calculation of volume fraction of porosity from solid and bulk densities is (Karathanos and Saravacos 1992);

$$\varepsilon = 1 - \frac{\rho_b}{\rho_s} \qquad [3.5]$$

where ε is volume fraction of porosity, ρ_b is bulk density and ρ_s is solid density. Solid density was measured using helium pycnometry. Helium pycnometry operates using a combination of Archimedes principle and the ideal gas equation (pV=nRT, where p is the absolute pressure of the helium, V the volume of the helium, n is the number of moles of helium, R the universal gas constant and T the absolute temperature of the gas) to calculate sample volume. Density is then calculated from this volume and the samples known mass. The calculated density is skeletal density, as opposed to true solid density, and includes any closed porosity contained within the cell walls.

Bulk density was measured using a volume replacement method (Hayter and Smith 1988; Hicsasmaz and Clayton 1992). A large measuring cylinder was filled with a known mass of 30 extrudates, m_e. Glass beads were then added to the measuring cylinder, ensuring all spaces external to the extrudates were filled, to a known volume V_t. The mass of the extrudates and glass beads combined was then measured, m_t. It then follows;

$$m_g = m_t - m_e \quad [3.6]$$

where m_g is the mass of the glass beads. The volume of the glass beads, V_g, is;

$$V_g = \frac{m_g}{\rho_g} \quad [3.7]$$

where ρ_g is the density of the packed glass beads. Hence by subtraction, the volume of the extrudates, V_e, is;

$$V_e = V_t - V_g \quad [3.8]$$

Combining equations [3.6], [3.7] and [3.8], the density of the extrudates is given by;

$$\rho_b = \frac{m_e}{V_t - \frac{m_t - m_e}{\rho_g}} \quad [3.9]$$

The glass beads had to be of small enough diameter to pack tightly and flow into spaces between extrudates whilst being large enough not to fill open pores on the extrudate surface. Figure 3.8 is an SEM image of the porous extrudate surface, the sample with the largest surface pores. The largest surface pores are no greater than 500 μm, hence glass beads of 500 μm diameter were used.

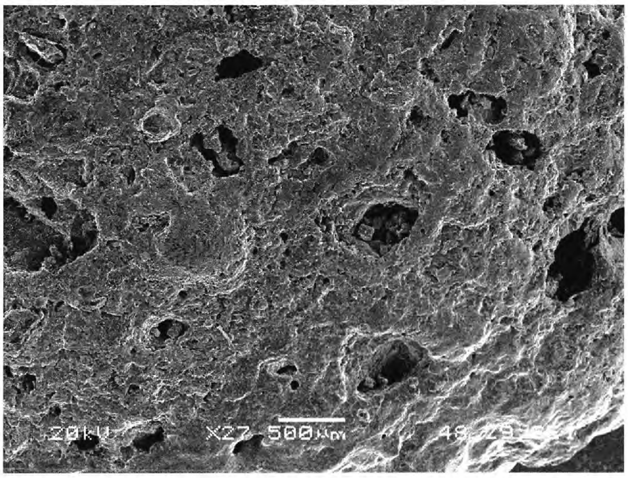

Figure 3.8: SEM of the porous extrudate surface.

3.1.9. Dimension and degree of expansion

The diameter and length of each disc sample was measured. Twenty repeats were taken for each measurement. The degree of expansion was also calculated. This is defined as the final extrudate cross-sectional surface area divided by the individual die hole surface area. Extrudate surface area was calculated using the measured diameter. One standard deviation was used for error analysis in all instances.

3.1.10. Pore wall thickness

Cell wall thickness was calculated from 2-D XMT image slices at evenly spaced intervals through the sample volume. An average across the image slices was then taken. The equation for average cell wall thickness, *t*, of each slice is (Trater, Alavi et al. 2005)

$$t = \frac{A_{sample} - \sum_{i}^{n} A_i}{\sum_{i}^{n} P_i} \qquad [3.10]$$

where A_{sample} is the sample cross-sectional area, A_i is the area of the i^{th} cell, P_i is the perimeter of the i^{th} cell and n is the number of cells. Image analysis was conducted using the DIPlib toolbox (Delft University of Technology, NL) running under MATlab.

3.2. Acoustic Method Development

3.2.1. Acoustic capture

This work is concerned with analysing the acoustic emission as captured during mechanical destruction. Mechanical destruction was conducted with a Stable Micro

Systems (UK) TA-XT2 texture analyser. The TA-XT2, a mechanical test machine, has many variables and the most appropriate method for capturing the acoustic emissions had to be devised. TA-XT2 variables were explored to produce a method that gave the greatest number of frequency peaks. This means it is less likely that vital spectral information is lost and non-relevant information can be ignored in later analysis if necessary.

Vibration can be measured through the mechanical test probe (Taniwaki, Hanada et al. 2006), however a standard air conducted microphone was used in this work to ensure no loss of information due to lack of vibration transmission to the probe. Furthermore, many modes of probe vibration will likely be excited when fracture occurs and stress in the system releases. Measuring acoustic signal through the probe would measure these vibrations if within the frequency range being considered.

3.2.1.1. Test variables

Test variables considered were microphone position [known to have a significant effect on signal intensity (Chen, Karlsson et al. 2005)], attachment type [numerous have been used in the literature (Chen, Karlsson et al. 2005; Gondek, Lewicki et al. 2006; Cheng, Alavi et al. 2007)], attachment speed, number of extrudates fractured simultaneously and extrudate position on the blade line. Each test setting had ten repeats recorded for which there is a frequency spectrum for each. However, only the average spectra are presented here. Differences seen in the averages are common across all repeats contributing to that average.

Two microphone positions were tried whilst using a blunt blade attachment, as seen in Figure 3.9, and blade speed of 2mms^{-1}. The first position was on the left of the blade at an angle of 45° to the horizontal pointing at the extrudate, and the second was in the centre of the blade at an angle of 45° to the horizontal pointing at the extrudate. The closest point of the microphone to the extrudate was 30mm along the horizontal and 30mm along the vertical in both instances. These positions are detailed in Figure 3.9a.

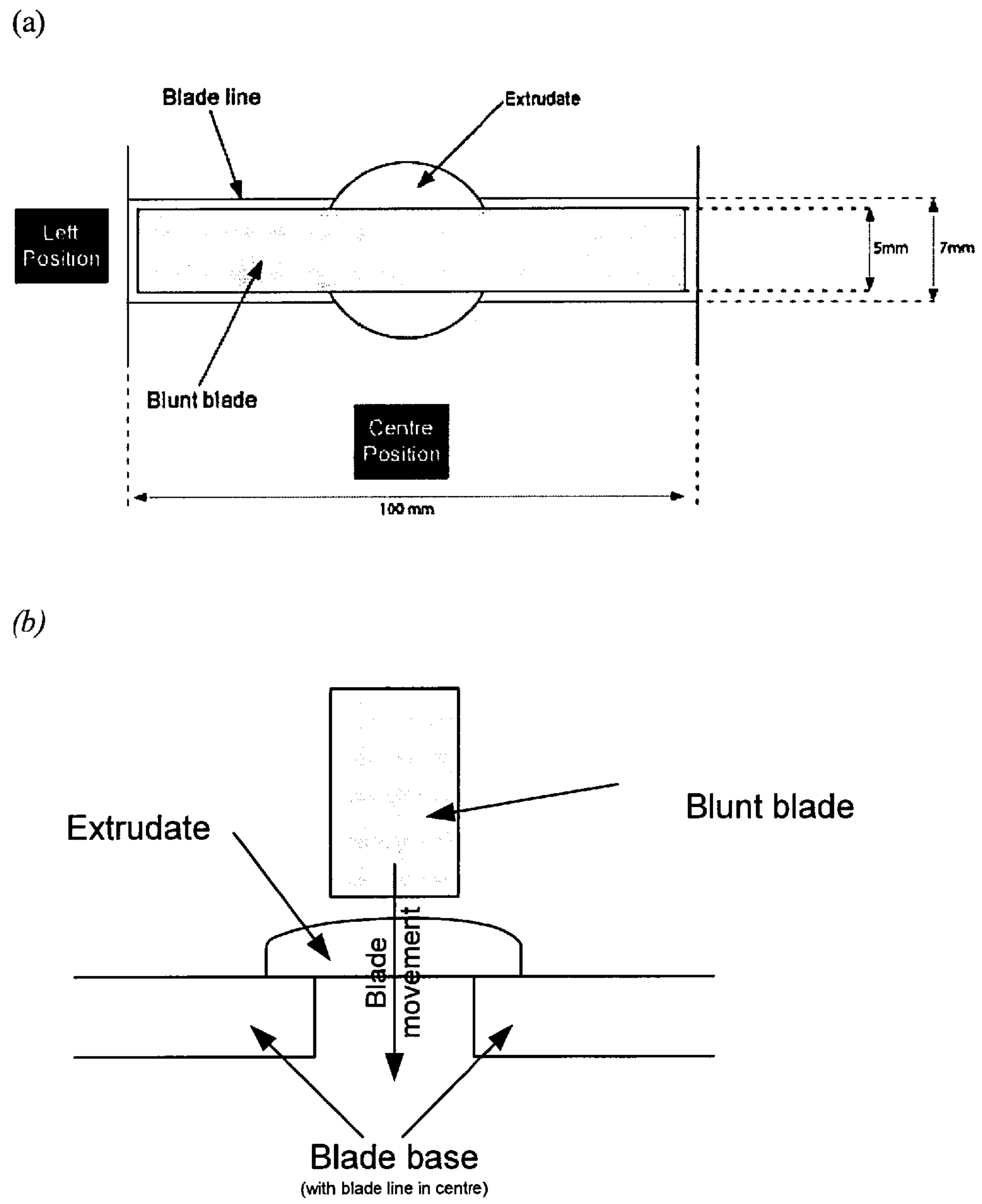

Figure 3.9: A diagram detailing the blunt blade attachment as it would be in operation. (a) gives a birds eye view and details two microphone positions used, whilst (b) gives a side on cross-section of the same setup including the blade movement.

Figure 3.10a and b show peaks are present in the spectrum when the microphone is placed at the centre of the blade attachment, whilst no obvious peaks are present when the microphone is placed at the left of the blade attachment. A value proportional to (as microphone voltage output was not calibrated) the total energy of the emission signals at the point at which the microphone was placed was calculated by integrating the area under the frequency spectra. When the microphone is in the centre there is an acoustic energy of (206±47)×10^3 units and only (8.4±0.67)×10^3 when the microphone is on the left. These energies show little acoustic energy reaches the microphone when it is on the left. The symmetry of the system, as seen in Figure 3.9a, will yield the same results with the microphone on the right as the left. This lack of acoustic energy is likely due to elements of the test rig impeding the travel of the acoustic wave. The microphone should therefore adopt a central position in the final methodology.

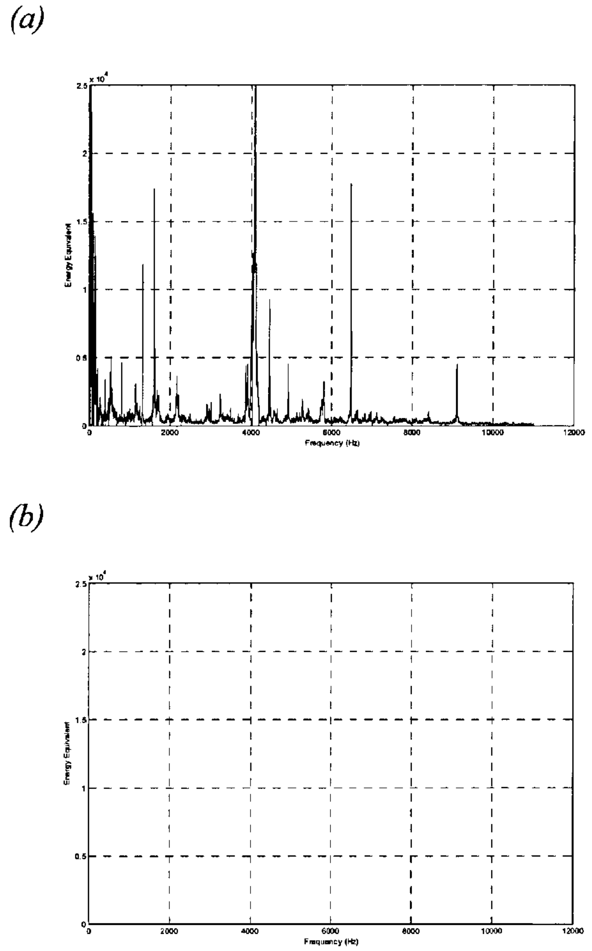

Figure 3.10: Average frequency spectrum, as taken from 10 repeats, with the microphone placed at (a) the centre of the blade attachment and (b) left of the blade attachment.

Figure 3.11 shows the average frequency spectra when different attachments were used on the TA-XT2 – the microphone was placed in the central position and a speed of 2mms^{-1} was used. The attachments tested were a cylindrical 2mm diameter (pin) probe, a cylindrical 20mm diameter (compression) probe, a sharp blade attachment and a blunt blade attachment. The sharp blade attachment is geometrically identical to the blunt blade attachment but with a 45^{o} cutting edge. The dimensions of the pin probe and compression probe correspond to flat-ended product contact surface diameter. Most work reviewed used a standard compression probe for capturing acoustic signals (Cheng, Alavi et al. 2007).

The spectra for each attachment showed both similarities and differences. Peaks for the pin probe were weak compared with the others. Spectra for the blunt blade and sharp blade are very similar but the blunt blade has additional frequency peaks and stronger peaks in general. The compression probe has fewer peaks and different peak positions to the sharp and blunt blade attachments.

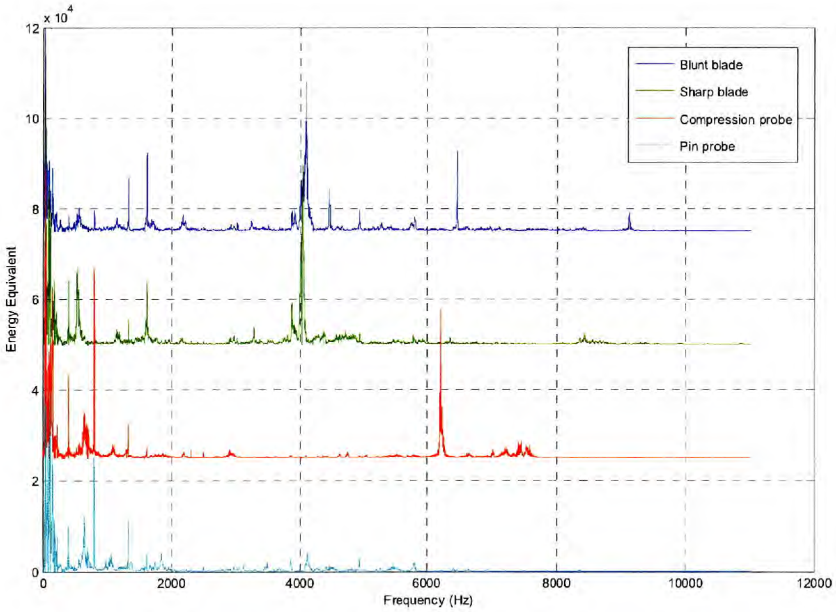

Figure 3.11: Average frequency spectra (from ten repeats) for different attachments on the TA-XT2 machine. Each spectrum is offset on the y-axis by 25000.

Fracture mechanics of the destruction with the blade attachments compared with the compression probe will be different. Friction between fracture pieces under the compression probe may also generate significant acoustic waves. These differences must be responsible for the spectral differences.

Using the criteria of selecting the method giving the most frequency peaks, the blunt blade attachment should be used. However, this method lacks some of the spectral information seen with the compression probe. It can be hypothesised that the blunt blade produces both compressive and bending forces (refer Figure 3.9a and b for operational diagrams of the blunt blade attachment), as would mastication. For this reason the blunt blade attachment will be used in the methodology. The additional peaks in the compression probe spectrum may also be due to the friction mentioned previously. These acoustic emissions are not characteristic of the destruction of the product but characteristic of the test so would not be important.

Attachment speeds were tested from $1 mms^{-1}$ to $10 mms^{-1}$, the range achievable on the TA-XT2 machine. The optimum microphone position and blunt blade attachment were used. Figure 3.12 shows the average frequency spectra for each attachment speed. The same frequency peaks are seen with speeds of $3.5 mms^{-1}$ and above. Below $3.5 mms^{-1}$ some peaks seen at greater speeds are not present. A test speed of $3.5 mms^{-1}$ will therefore be used for the methodology. Differences to the blunt blade spectrum in Figure 3.12 are due to tested samples being produced at different extrusions.

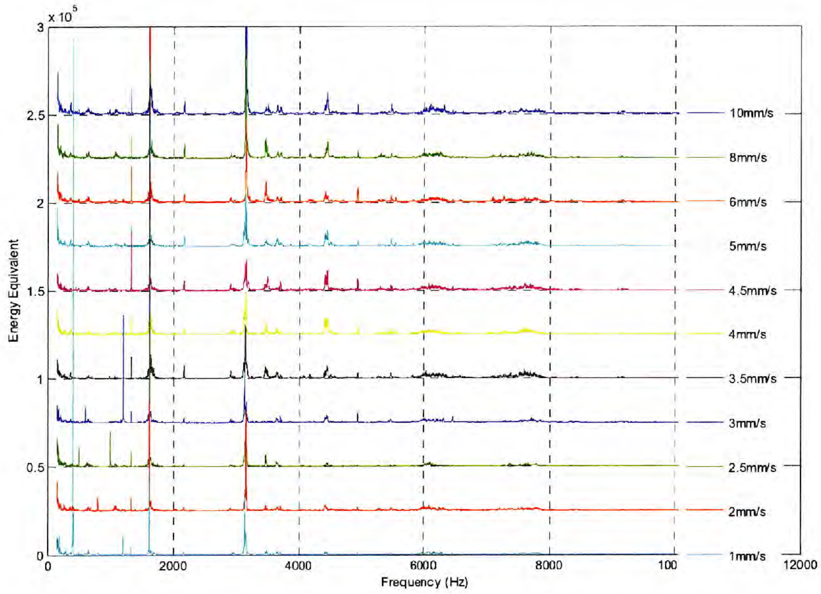

Figure 3.12: Average frequency spectra (for ten repeats) using different attachment speeds in the TA-XT2 test. Different speeds are offset by 25000 on the y-axis.

The number of extrudate samples placed along the blade line was considered, and using one or three samples was investigated. Figure 3.13 shows that there is little difference between using one or three samples, with both spectra showing the same peak locations and similar intensities. With this in mind it was decided that one extrudate would be used for the methodology. Using one extrudate would minimise effects such as interference between acoustic waves possibly simplifying analysis and reducing experimental error. The single extrudate was placed in the centre of the blade line.

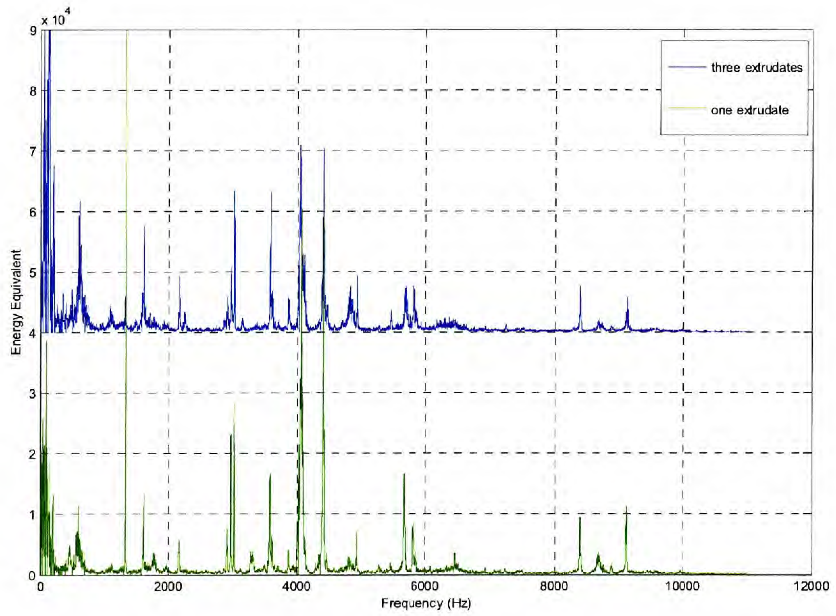

Figure 3.13: Average frequency spectra (from ten repeats) when different numbers of extrudates are placed on the blade line of the TA-XT2 during a test. The spectra are offset by 40000 on the y-axis.

Extrudate position and orientation on the blade line was the final variable to be tested. Test conditions as previously selected were used. All previous tests have placed the extrudate disc on its flat surface in the centre. Here the extrudate was placed on its flat surface in the centre for one test and at the left of the blade line for another test. The symmetry of the system would yield the same results if the extrudate was placed on the right as with the left. The final position was having the extrudate stood on its side in the centre of the blade line.

Figure 3.14 shows having the extrudate on its flat surface and in the centre results in the largest number of frequency peaks and the peaks have greater intensity. When the extrudate was stood on its side, little acoustic vibration was detected by the microphone. This can be seen with total energies of $(279\pm19)\times10^3$ for flat centre, $(169\pm48)\times10^3$ for flat left and $(37.7\pm17)\times10^3$ when stood on its side. The extrudate will therefore be placed on its flat surface and in the centre of the blade line for the methodology.

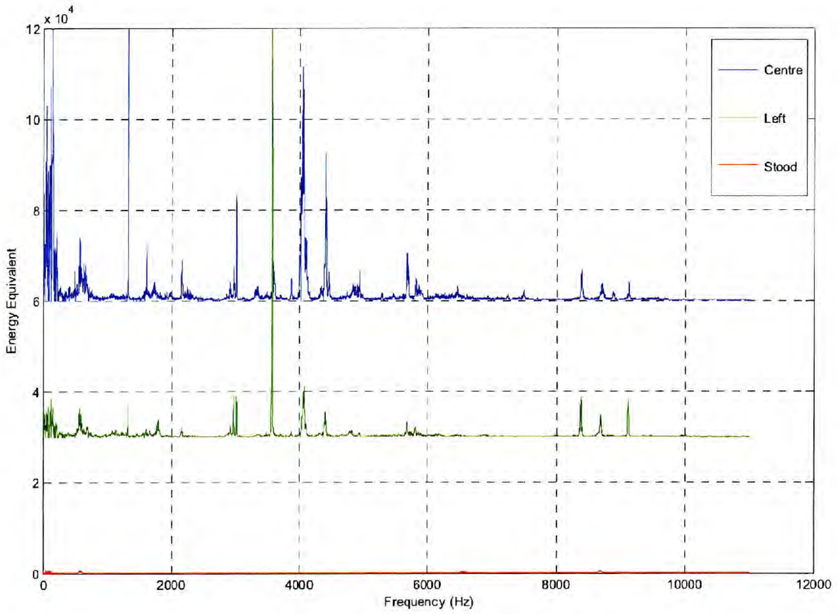

Figure 3.14: Average frequency spectra (from ten repeats) for different positions and orientations on the blade line during the TA-XT2 test. Each spectrum is offset by 30000 on the y-axis.

3.2.1.2. Extrudate fracture pieces

The acoustic information generated from the mechanical destruction of an entire extrudate and the acoustic information from the destruction of a fracture piece from the initial destruction (and so on) was considered for three extrudates. The frequency spectra generated for each mechanical destruction can be seen in Figures 3.15a-c. The test settings as decided in the Test Variables section (3.2.1.1) were used for the mechanical destruction.

(a)

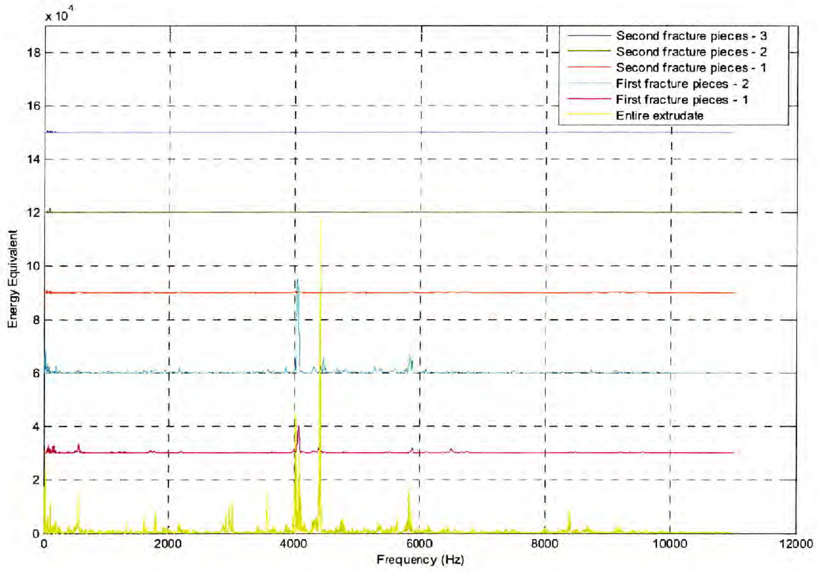
x 10^4
Second fracture pieces - 3
Second fracture pieces - 2
Second fracture pieces - 1
First fracture pieces - 2
First fracture pieces - 1
Entire extrudate
Energy Equivalent
0
2
4
6
8
10
12
14
16
18
0
2000
4000
6000
8000
10000
12000
Frequency (Hz)

(b)

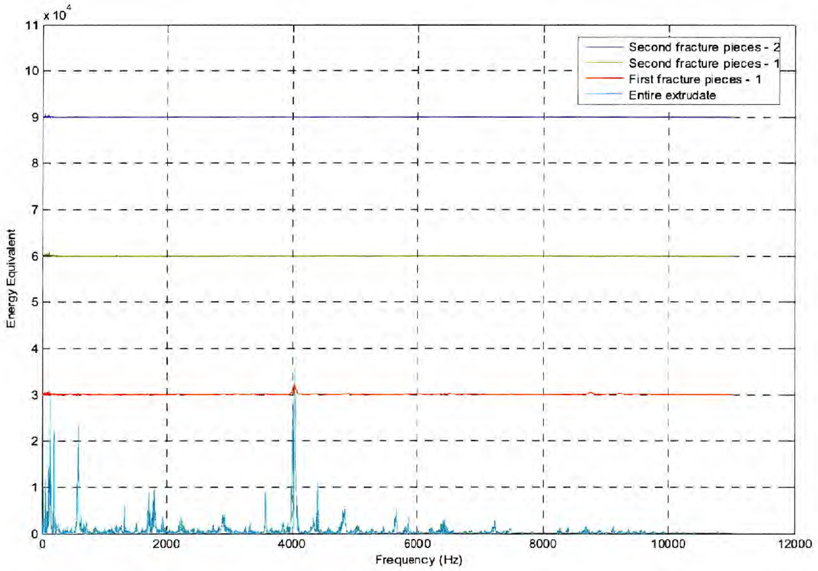
x 10^4
Second fracture pieces - 2
Second fracture pieces - 1
First fracture pieces - 1
Entire extrudate
Energy Equivalent
0
1
2
3
4
5
6
7
8
9
10
11
0
2000
4000
6000
8000
10000
12000
Frequency (Hz)

(c)

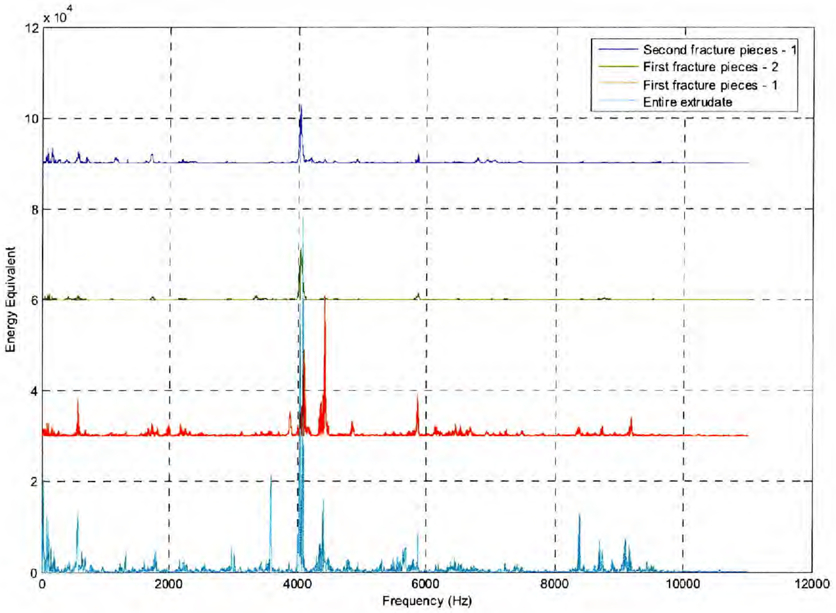

Figure 3.15a-c: The frequency spectra for an entire pellet and its fracture pieces as generated by mechanical destruction using a TA-XT2 machine. Different spectra are offset on the y-axis by 30000. (a), (b) and (c) are three different extrudates.

There are no additional frequency peaks when mechanically destroying fracture pieces when compared with the entire extrudate in all three instances. For all three extrudates the mechanical destruction of the entire pellet is the only acoustic wave with all frequency peaks which are present in the spectra of all fracture pieces. For this reason it was decided necessary to only test the as-produced extrudate disc.

The fact that the emission is lower as the extrudate is broken down shows loss of product structure reduces the acoustic emission. This may be due to geometric properties of the pieces, a weakening of the structure from the initial destruction or a lack of all acoustic vibratory components being contained within the piece. When considering these results it has to be remembered some frequency peaks could come from the test system itself. This will be discussed in more detail in later sections. Figure 3.15c shows the spectrum of the only extrudate whose first fracture piece continues to hold a significant amount of spectral information.

3.2.2. Analysis

The aim in the analysis is to gain acoustic information that can be used to compare different extrudates. This will be done via a number of techniques of data reduction and analysis within the MatLab computer programming software.

3.2.2.1. Acoustic information

The literature demonstrated the breadth of information that has been used to study acoustics in both the food industry and elsewhere. The review showed the time domain is difficult to draw comparisons from and for this reason the work done here will concentrate on comparing the signals in the frequency domain. But it must be remembered there is concern about losing vital acoustic effects as generated by the phase and lag of different frequency waves that are not described when a signal is in the frequency domain.

Although the focus is on comparing the frequency spectra of different tests/samples, further acoustic properties may be discussed as identified in the literature review. These are signal energy, maximum sound pressure and energy build with time. These parameters are only values applicable to the point at which the microphone was placed as it is not known if the acoustic energy is isotropic around the acoustic events origin. As the acoustic signal is further understood additional acoustic parameters may be considered.

The frequency spectrum for each signal was computed using MatLab and the in built Fast Fourier Transform (FFT) computer algorithm. The maximum frequency which can be resolved is known as the Nyquist frequency and is equal to half that of the sample rate used in the recording. All files were recorded using Cool Edit Pro audio editing suite as .wav files with a 44100Hz sample rate at 16bit. In these tests the limiting factor is the microphone which is sensitive to 12000Hz, the limit of adult human hearing.

The number of data points in the frequency spectrum is dictated by the sample rate and the duration of the acoustic wave. The sample rate was 44100Hz and all recordings were zero padded to a duration of 3.4014s giving all acoustic wave files, and ultimately frequency spectra, the same number of data points so that averages could be taken using the frequency spectrum. Zero-padding means the addition of data-points equal to zero in the time domain from the point at which no signal was recorded. 3.4014s was selected as a time after which it was known no acoustic signal would be present for any sample. Ten repeat recordings were taken for each test unless otherwise stated.

The microphone was not calibrated. This means values for sound pressure are not absolute and have no absolute units. The values are suitable for comparison and all terms will be described as equivalent. The FFT algorithm within the MatLab program transforms the acoustic wave to give amplitude equivalents for each frequency step. The square of these amplitudes results in an energy equivalent which is how the data are presented in the frequency spectra through the report.

The signal energy for each recording was calculated using a trapezoidal approximation method to integrate under the energy frequency spectra. The maximum sound pressure was found using the 'find max' function available within MatLab. This was used on the sound pressure data as read from the .wav recording.

Energy build with time was taken by calculating the cumulative energy of the sound pressure-time plot. This was done by squaring the sound pressures to give an energy equivalent. The trapezoidal method of integration was then used to calculate the cumulative energy at each time interval, as dictated by the original signal. Averages were not taken for this data and each signal was considered individually.

3.2.2.2. Time signal reduction

Recording of the acoustic signal results in times with no relevant information both before and after the initial and final fracture. These areas were cut from the original acoustic signal to reduce the amount of non-relevant and background frequencies that were analysed using Cool Edit Pro. This is demonstrated in Figure 3.16. For reasons explained in Acoustic Information (3.2.2.1) the signal was then zero padded to 150000 data points.

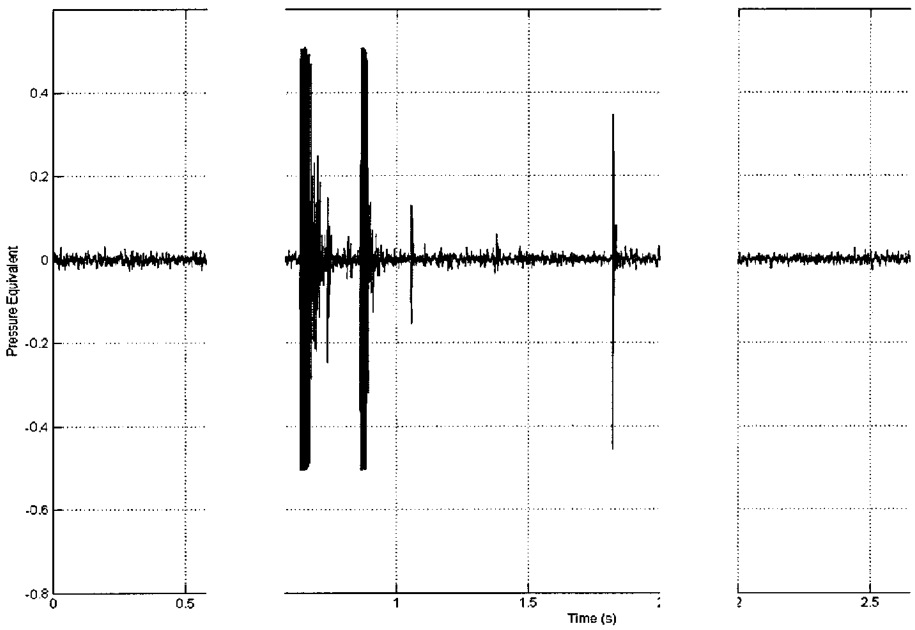

Figure 3.16: An example of how an acoustic file would be cut to leave only relevant information. Only the central section where there is relevant wave-form was kept for analysis.

Cutting and zero padding the wave-form will add a square wave to the signal. This will be seen in the frequency spectra but due to the associated amplitude will be insignificant compared with other more prominent frequencies and hence is not a concern.

Cutting different wave-forms at different points may affect the signal energy for comparison. However, for the signal in Figure 3.16, the parts of the signal that have been cut have energies of 7034units and 4545units whilst the signal bulk has energy of 6.9×10^6 units. The cut parts contribute no significant amount of energy to the energy of the original signal. If considering energy build with time the position of the initial cut does have an effect, however energy build with time will always be analysed with the acoustic wave-form in mind.

Further reduction was attempted by looking at individual acoustic events. The events were separated by eye as seen in Figure 3.17. There are seven distinct acoustic events.

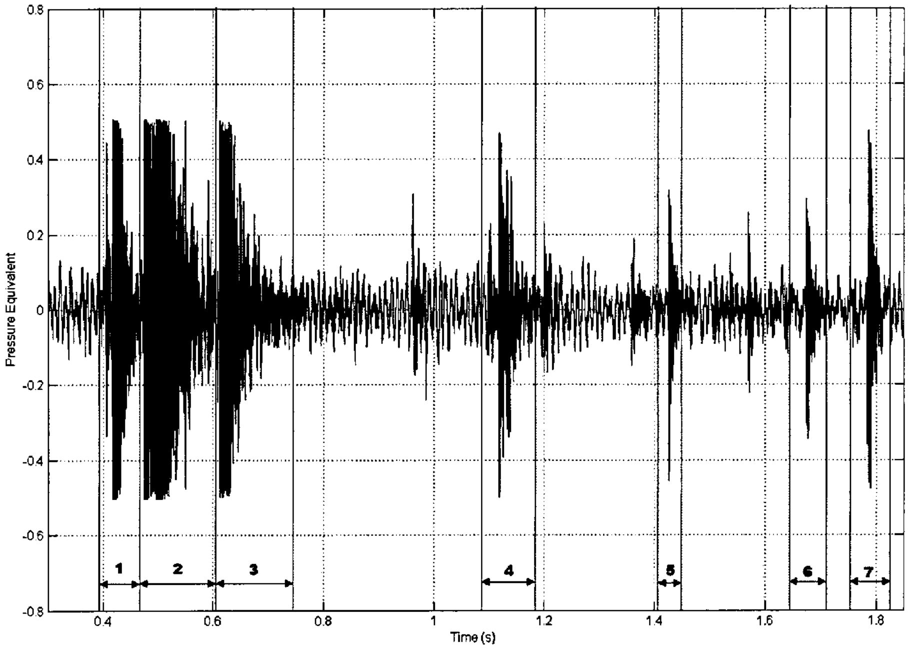

Figure 3.17: An example of how the acoustic wave-form would be sectioned into individual acoustic events. The position at which to section the wave-form was achieved by eye.

The frequency spectra for the acoustic events detailed in Figure 3.17 can be seen in Figure 3.18. Each spectrum is separated by 25000 on the y-axis.

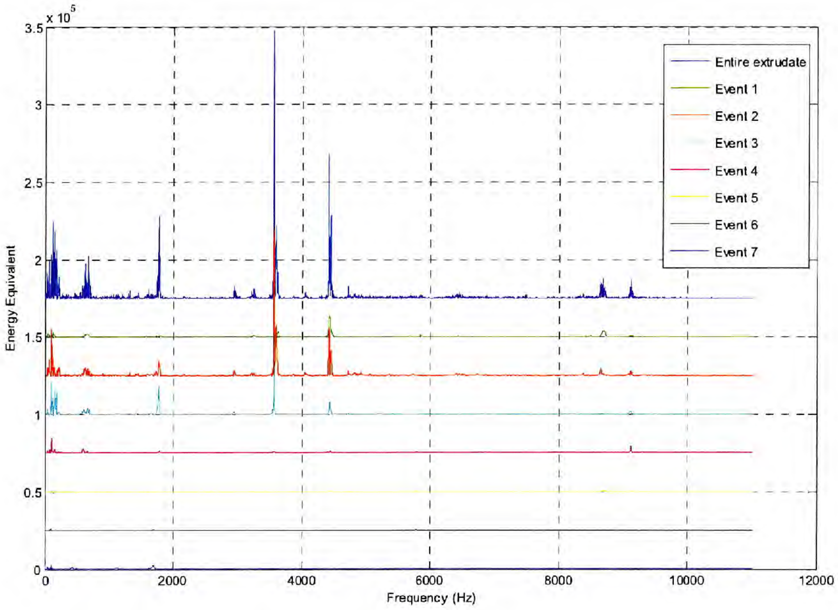

Figure 3.18: Frequency spectra for the entire pellet and individual acoustic events from the destruction of the entire pellet. These individual acoustic events are those as detailed in Figure 3.17. Each spectrum is separated by 25000 on the y-axis.

Events one, two and three have similar frequency peaks to each other and the entire extrudate. Event two has some peaks none of the other events have and most if not all peaks the entire extrudate spectrum has. All peaks in the entire extrudate have highest energies. Because of this the only reliable method of obtaining a frequency spectrum representative of the entire pellet is to analyse the entire acoustic wave-form with all events present. However some of the individual acoustic events do have the majority, if not all, of the spectral information.

The first acoustic event, as shown in Figure 3.18, is not the one with most spectral information. Table 3.3 shows the signal energy for each acoustic event. Event two is the one with most energy, whilst events four, five, six and seven have very little energy. Event one and event three have energy somewhere in-between.

Due to the air-drying method used for extrudates they will have a case-hardened outer surface/shell. Event one, which corresponds to breaking the outer surface 'shell' of the extrudate, had lower energy than both events two and three. This shows additional spectral information and a significant portion of acoustic energy is from the internal structure (i.e not seen in event one).

Table 3.3: Energy equivalent values for the acoustic events as detailed in Figures 3.17 and 3.18.

Acoustic Event	**Energy Equivalent**
1	2030000
2	6500000
3	3040000
4	772000
5	161000
6	156000
7	513000

3.2.2.3. Frequency range

The frequency range studied was 0Hz to 12kHz due to limitations of the microphone sensitivity. However, 12kHz is the limit of adult human hearing, so is suitable from an analysis perspective. Logarithmic scales for the frequency axis were also investigated to emphasise lower frequencies for analysis.

3.2.2.4. Data reduction

Data reduction involved the removal of frequencies present in the frequency spectra but not related to the extrudate itself. These frequency peaks will be due to machine noise, background noise and vibrations in the test apparatus itself. If frequencies are not convincingly identified they are not removed and acknowledgement must be given to this in future analysis.

Whether the blade and blade base were vibrating and creating peaks in the frequency spectra were first to be considered. Figures 3.19a-b show the blade excited by different methods, those being tapping the blade against a block of wood and dropping a ball bearing onto the centre point of the blade whilst being supported by a sponge.

(a)

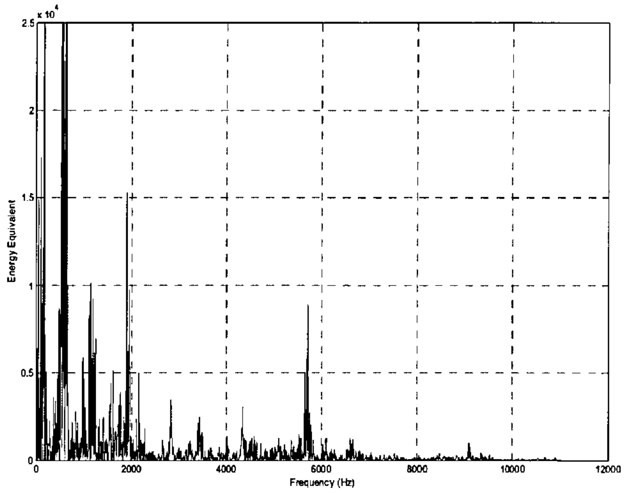

(b)

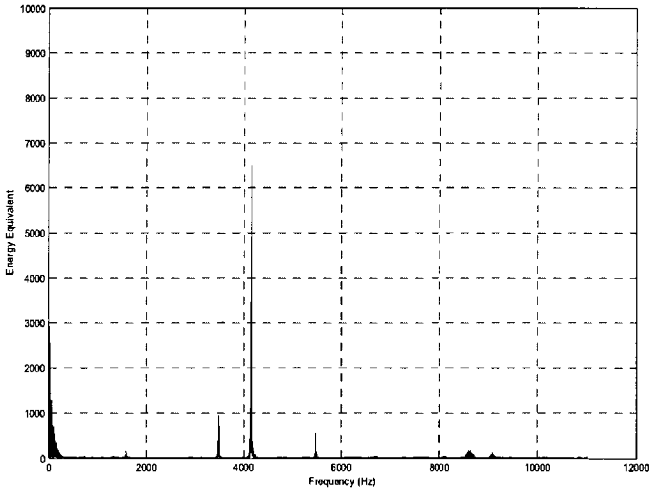

Figure 3.19: Example frequency spectrum of the blade attachment when it is excited by different methods. These methods were (a) excited by tapping it against a block of wood and (b) dropping a ball bearing in its centre whilst on a sponge.

Different frequency peak positions are seen for different methods of excitation due to different modes being excited. Exciting the same modes as those in the test is near impossible as the exact forces applied to the system in the test are not known. This means no frequency peaks can be removed but further investigation will be presented later in this Chapter.

The data can be further reduced via the removal of background frequencies of both the room and those produced by the machine during operation. Figure 3.20 shows the frequency spectra of the background noise plotted on the same y-axis scale as the frequency spectra are usually plot, with both (a) linear and (b) log scales for the x-axis. For comparability to mechanical destruction acoustic emission frequency spectra the acquisition time was set at the maximum a signal could be, 3.4041s.

(a)

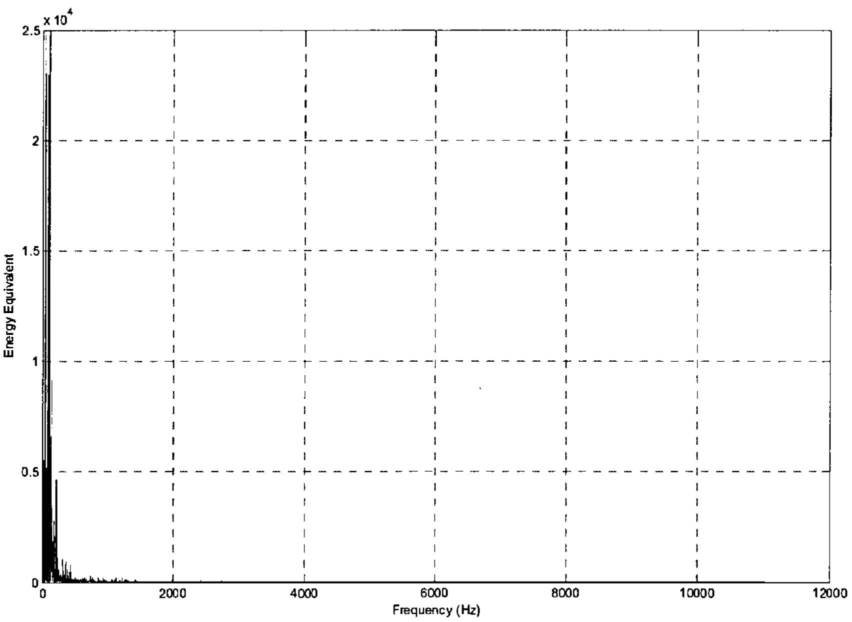

(b)

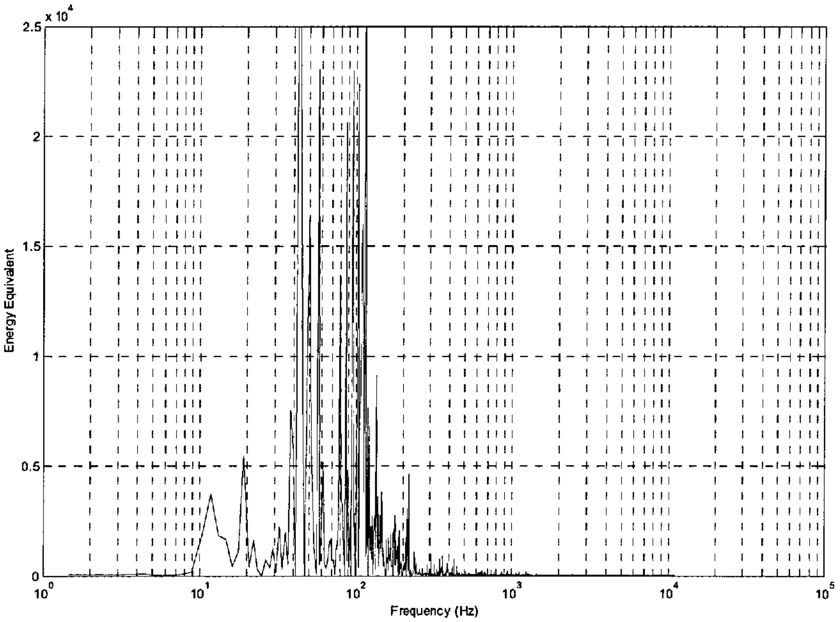

Figure 3.20: Example frequency spectra of the background noise as recorded with the microphone in the same position as when the test is conducted and machine not running (a) on a linear scale for the x-axis and (b) on a log-scale for the x-axis.

All background noise is at low frequencies as the frequency spectrum has near zero energy values after 250Hz. Furthermore, many large background peaks are below 150Hz and closely spaced making removal of these peaks difficult and analysis of additional peaks in this area near impossible. For this reason energy values for frequencies below 150Hz were made equal to zero and this area discounted in analysis. This range will include mains hum and DC levels in the equipment.

Next the machine was considered whilst under load. The machine noise audibly changes when under load. A load was applied to the TA-XT2 during a test by using a material that did not create fracture sounds, tissue paper. The snug fit of the blade in the blade line resulted in a required force similar to that seen with the destruction of extrudates (approximately 20-30N). An example of a frequency spectrum generated by this loaded test is given in Figure 3.21 with frequencies below 150Hz made equal to zero.

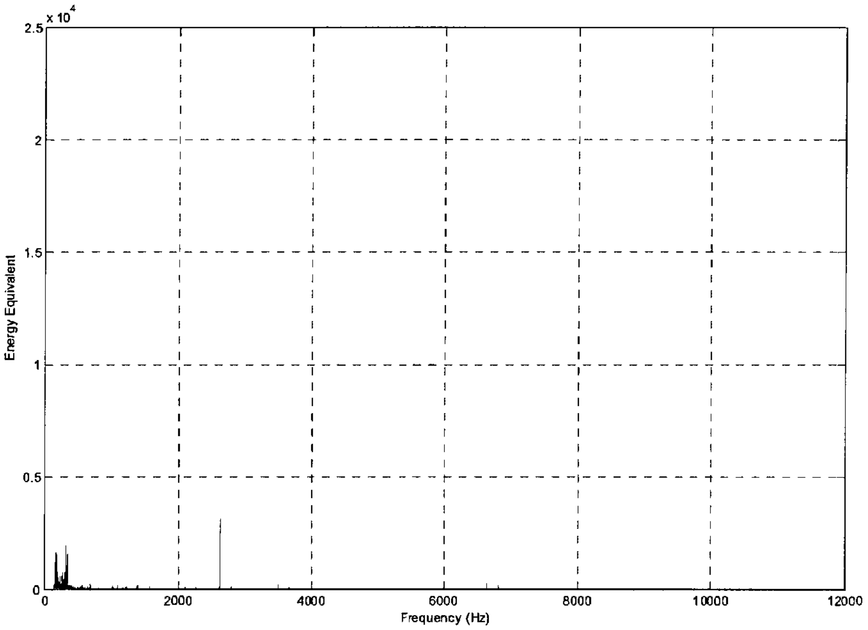

Figure 3.21: An example of the frequency spectrum as generated when the TA-XT2 machine is run under load with a material that produces no fracture sounds. Tissue paper was the material used.

There are some low frequency peaks and only one large peak at 2625Hz. There are small peaks which are not present in the background noise spectrum. As these will be additional peaks due the TA-XT2 under load it was decided all will be removed from the spectra of mechanically destroyed extrudates.

To decide which frequencies should be removed a definition of a peak had to be made. Figure 3.22 shows the loaded machine spectrum as seen in Figure 3.21 with an expanded y-axis scale.

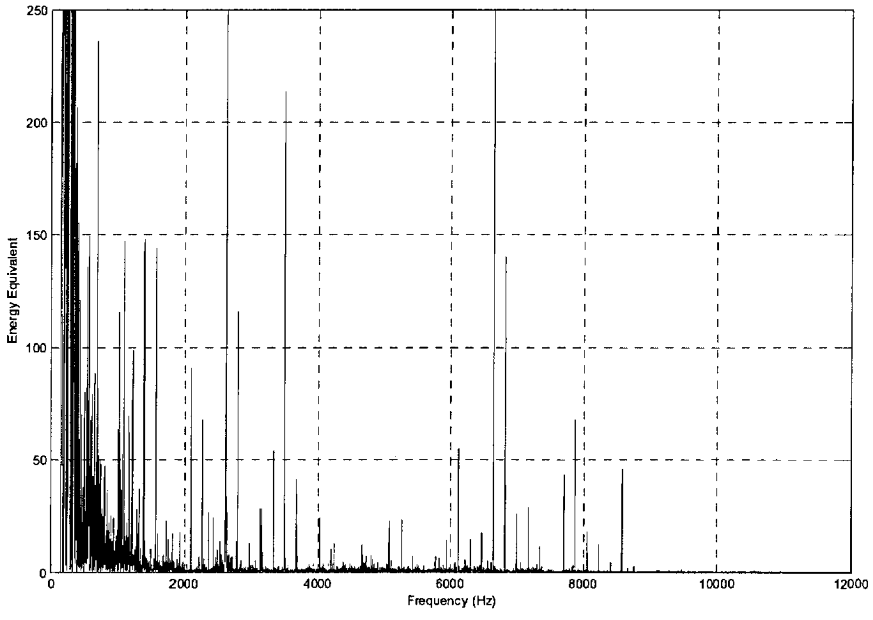

Figure 3.22: An example of the frequency spectrum as generated when the TA-XT2 machine is run under load with a material that produces no fracture sounds. Tissue paper was the material used. The scale for the y-axis has been much reduced compared with Figure 3.21.

To define a peak the frequency range 250-12000Hz was analysed and the background and machine noise compared. Numerous definitions (energy equivalent values) were considered and the frequencies at which the spectra energy values went above this definition were noted. The point at which there were no peaks in the background spectra of all ten repeats that were not present in all ten spectra for the machine whilst under load was taken as the peak definition. This was based on the premise that no peaks should be present in the background noise spectra that are not also present in the spectra of the machine under load. This resulted in a peak being defined as greater than 100units on the energy equivalent scale.

Peaks, as defined above, present across all ten repeats for the spectra of the machine under load were obtained. These were the peaks generated by the TA-XT2 under load. Removal of these peaks was written into the MatLab program.

3.2.2.5. Experimental equipment

The system and equipment used for the test may vibrate when stress in the system is released, hence creating an acoustic wave and frequency peak(s) in any spectra. This was initially discussed in the Data Reduction section (3.2.2.4) with no firm conclusions. To further consider this the two ceramic samples were tested alongside the standard extrudate. It is reasonable to assume that common frequency peaks from very different specimens are likely due to the system as the test will excite the same modes of vibration. The frequency spectra for these can be seen in Figure 3.23.

The frequency spectra for all three tests are different. Audibly, when the test was conducted, the solid ceramic discs sounded more similar to the extrudate fracture than the foam ceramic. This is evidenced in the similarities in peak clarity between the extrudate and solid ceramic disc compared with the foam ceramic disc and may indicate a cleaner more catastrophic (rapid) fracture.

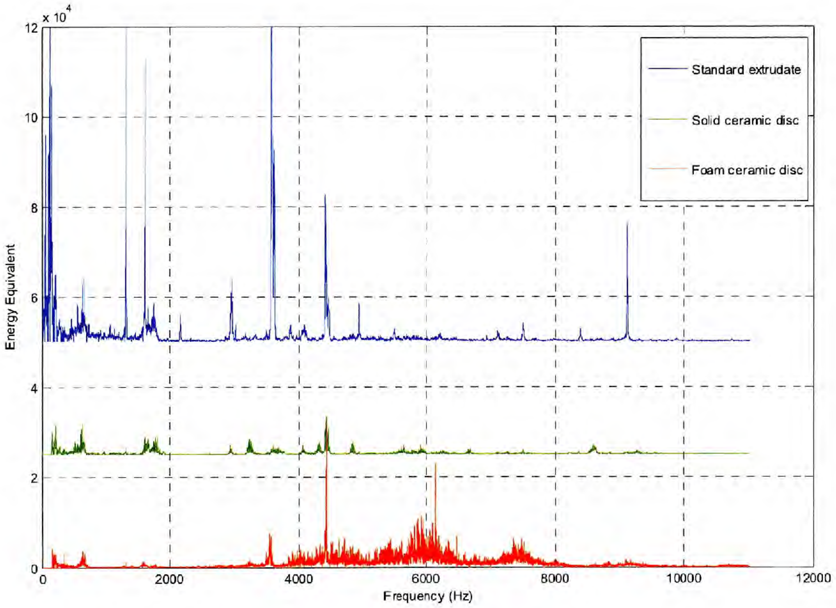

Figure 3.23: The average frequency spectra (from ten repeats) for a standard extrudate, foam ceramic and solid ceramic disc. The spectra are offset by 25000 on the y-axis.

The frequency spectra for the extrudate and solid ceramic whilst having major similarities show differences in both peak position and intensity. Because the fracture of the ceramic foam sample was visually and audibly different, it was assumed acoustic vibration from the system might also be different.

Peaks that are common irrespective of intensity between the solid ceramic and extrudate are <1000Hz, 1600-1800Hz, 4420-4440Hz, and 7510-7520Hz. However, within these frequency bands there are distinct differences in exact peak location. Of these peaks the major similarity is at <1000Hz and 4420-4440Hz in terms of position and intensity, hence it is likely these peaks are from the system. Other similar peaks cannot be unambiguously attributed to the test rig and must be included, and remembered, in the spectral analysis. Figure 3.19 shows how many modes of vibration can be excited for the test rig itself.

3.2.2.6. Do acoustic differences occur?

The Experimental Equipment section (3.2.2.5) has shown that relatively small spectral differences occur when entirely different materials are tested, those differences being in both peak intensity and position. However, it is still difficult to define how important peak position and peak intensity are in describing acoustic differences. This creates two questions: Do spectral differences occur between extrudates? If differences do occur how can they be defined?

To answer the first question, four structurally different extrudates were tested, those being the porous extrudate, dense extrudate, STD1 and STD2. The frequency spectra for these can be seen in Figure 3.24.

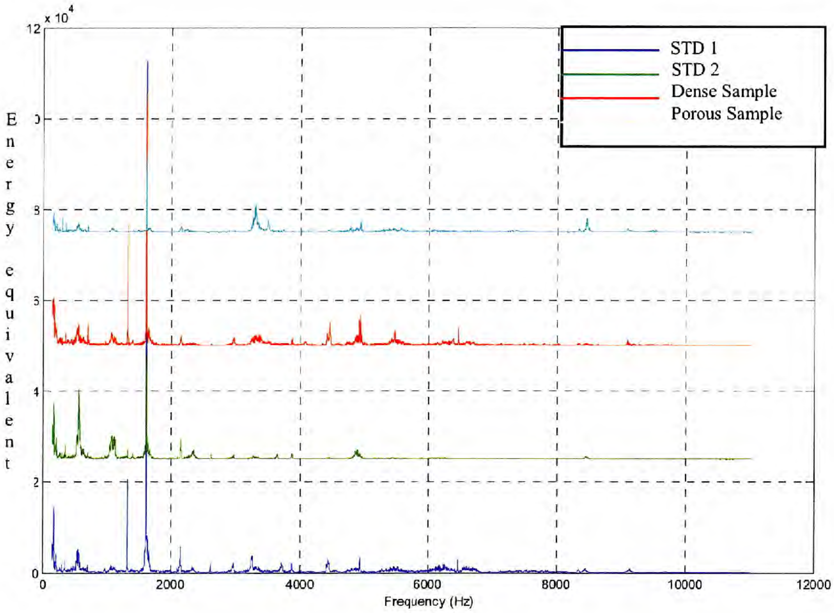

Figure 3.24: Average frequency spectra for four different products. These products were STD1, STD2, the porous product and the dense product. Each spectrum is offset on the y-axis by 25000.

The frequency spectra for all four products are noticeably different. Common and different peaks can be seen for each product. Peak intensities vary and the general 'shape' of the spectra are different. The differences seen are common across all repeats. This demonstrates extrudate frequency spectral differences do occur, including when the same recipe is used as with the porous product and dense product. The differences seen are larger than those between the standard extrudate and solid ceramic in Figure 3.23. The main common frequency peak between 4420-4440Hz in Figure 3.23 is only visibly present in two of the spectra, the dense product and STD1 product.

The spectra show that peak position will be important for defining acoustic spectral differences, as this is where major differences occur between products. The differences seen in peak intensity are often similar to those seen between repeats for the same product. This shows use of peak intensity to define acoustic differences may be difficult. This will be further considered in later sections.

3.2.3. Further analysis ideas

Ring down count (RDC) is an additional acoustic parameter that came to light during reading and thought valuable for the work. RDC is used frequently with non-destructive testing incorporating acoustic emissions (William 1980). It is defined as the number of times a given signal voltage crosses a pre-defined detection threshold. In the case of the acoustic wave-form plots in this report the voltage is the sound pressure equivalent.

Figure 3.25 shows the sound pressure-time plot for the mechanical destruction acoustic emission test rig when under load using a material that does not create fracture sounds, tissue paper. The sound pressure rarely exceeds a value of 0.125. For this reason the RDC threshold was set at 0.125 meaning each count was likely due to the destruction of the extrudate. A program was developed, using MatLab, to measure RDC giving the average of ten acoustic recordings for each sample set.

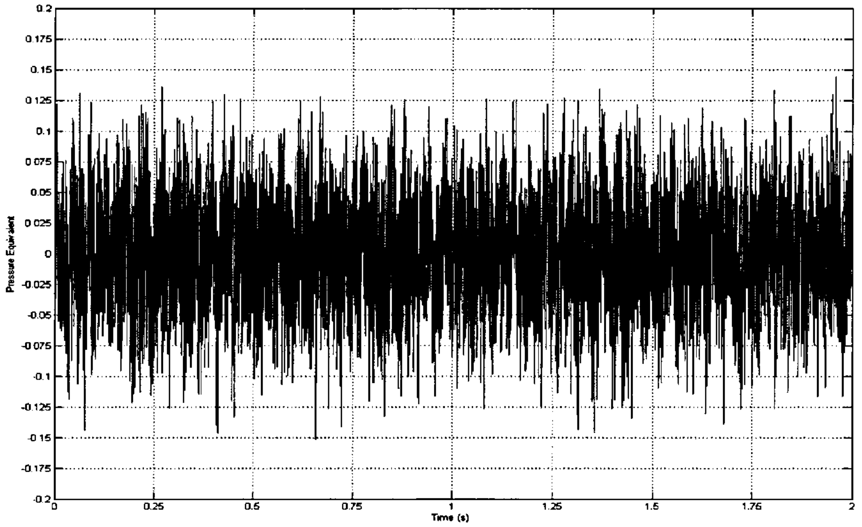

Figure 3.25: Sound pressure-time plot of the mechanical test system when under load with a silent material (tissue paper).

3.2.4. Final acoustic method

The result of the acoustic method development was as follows. The acoustic emission as produced during mechanical destruction was recorded. Mechanical destruction used a TA-XT2 machine provided by Stable Micro Systems with a single entire extrudate on its flat surface. A blunt blade attachment was used for the mechanical destruction with the extrudate placed in the centre of the blade line. A microphone was placed in the centre of the blade line a distance of 30mm along the horizontal and vertical from the extrudate at an angle of 45° to the horizontal. The mechanical destruction test was conducted at a speed of 3.5mms^{-1}.

Recording was done with the microphone connected to a Dell laptop computer. Cool Edit Pro audio editing suite was used for recording and cutting the audio file down to the relevant section. Recording was done in mono at 16-bit resolution with 44100Hz sample rate as .wav files. 10 repeat recordings were taken for each product.

The resulting audio files were analysed to give the frequency spectrum using MatLab. The MatLab analysis program calculated maximum sound pressure, total signal energy, energy build with time and ring down count.

3.3. Structural Characterisation Method Evaluation

The objective of the work described in this section was to develop a suitable image processing method for extracting pore structural parameters from XMT analysis. As discussed in the structural characterisation literature review (section 2.2) and Materials and Methods (section 3.1), the method decided upon was a 3-D watershed algorithm applied to determine pore size distribution. Volume fraction porosity was determined by 2-D image analysis, 3-D image analysis and density measurements. Cell-wall thickness was obtained by conventional 2-D image analysis of XMT image slices. The approach was evaluated by application to two different extrudates, porous and dense, whose characteristic structural parameters are compared.

XMT can be used for both qualitative and quantitative analysis. Solid sections can be tetrahedrally meshed and the internal structure visualised. Figure 3.26 is a tetrahedral mesh of a 1.44 mm^3 section of the internal structure of the porous extrudate created using Amira (Mercury Computer Systems). Structural features can be clearly seen. Furthermore, the tetrahedral mesh can be used as input data for modelling other properties (such as mechanical stiffness).

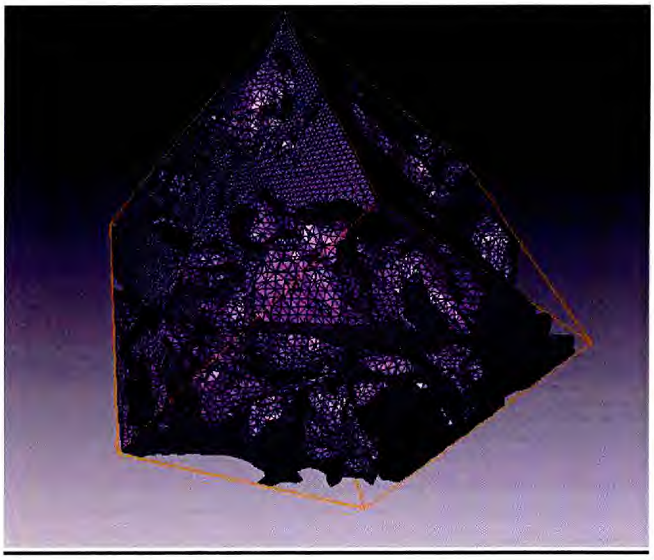

Figure 3.26: 1.44 mm^3 section of a porous extrudate showing its internal structure formed using a tetrahedral mesh (porosity is transparent).

3.3.1. Pore size distribution using a 3-D watershed algorithm

The first step in analysing the image was to select the contrast threshold that distinguishes between solid and pore space. Figure 3.27 shows the contrast histogram for the porous extrudate, emphasising lower number frequencies, with the y-axis representing voxel contrast value. In this representation the higher density voxels have the higher contrast values. It is clear that there are three distinct density phases at different contrast values as detailed in Figure 3.27. Thus, by using the appropriate thresholds, different phases can be studied separately if of interest. Figure 3.28 shows a two-dimensional slice of the highest density phase, thought to be cellulose from wheat kernel casings in the original recipe. Cellulose has greater density than both starch and protein. This work was only interested in extrudate porosity so both the starch and cellulose phases were combined and termed the solid section.

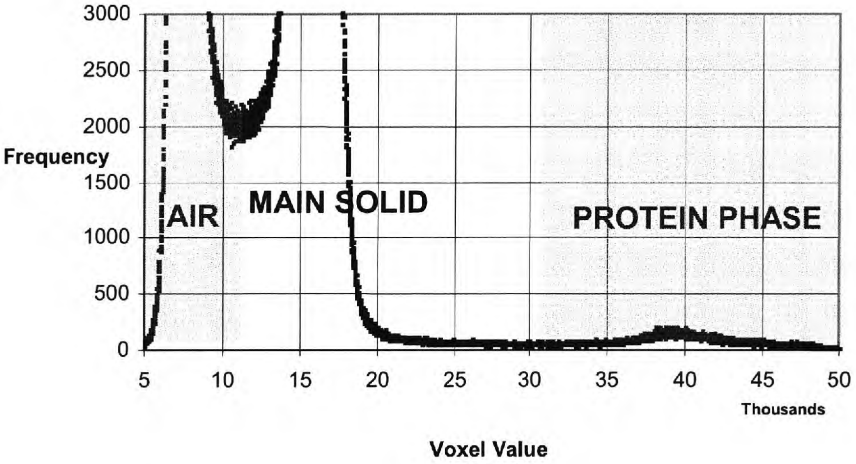

Figure 3.27: Contrast histogram for the porous extrudate showing three distinctly separate density phases.

Figure 3.28: A 2-D slice through the porous extrudate sample showing the distribution of the highest density (protein) phase in grey. Lower density solid and air are black.

The effect of the threshold value (for separating pore space and solid) on the pore size distribution was considered. From the contrast histogram of Figure 3.29 a contrast value of 11,000 was selected as being most appropriate (see later for further details).

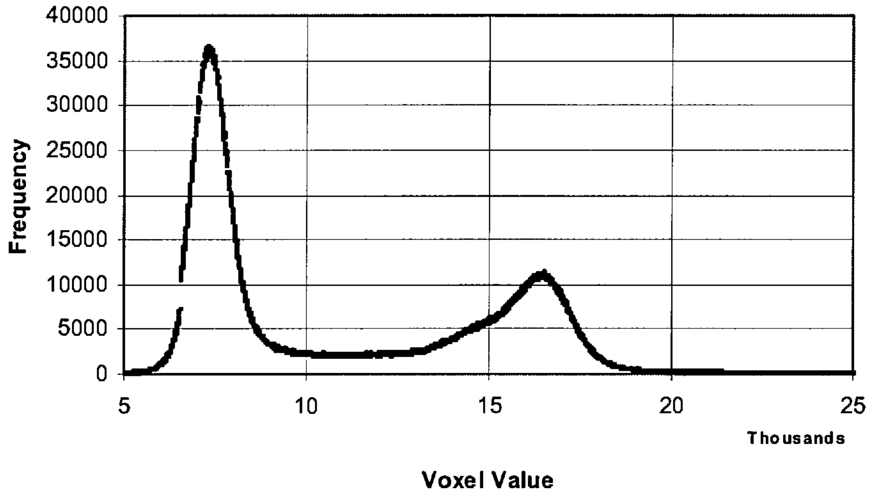

Figure 3.29: Low contrast part of the contrast histogram for the porous sample.

Once the threshold was applied the 3-D image was dilated and the watershed algorithm applied (see section 3.1.8). A 2-D slice through the (watershed) segmented volume of the porous sample can be seen in Figure 3.30. Visual inspection shows the segmentation to be reasonable. However, there are areas where it is difficult to judge the segmentation in two-dimensions. Figure 3.31 shows the same 1.44mm^3 section as in Figure 3.26 but displaying only the segmented porosity and omitting the solid phase. Figure 3.32 shows the solid phase and segmented porosity combined into one image. Visual interpretation of Figures 3.30, Figure 3.31 and Figure 3.32 shows the three-dimensional (watershed) segmentation to be appropriate and located at obvious apertures.

Figure 3.30: 2-D section through porous extrudate showing segmented pores in different colours (i.e. different pores are different colours) with solid and external air being black.

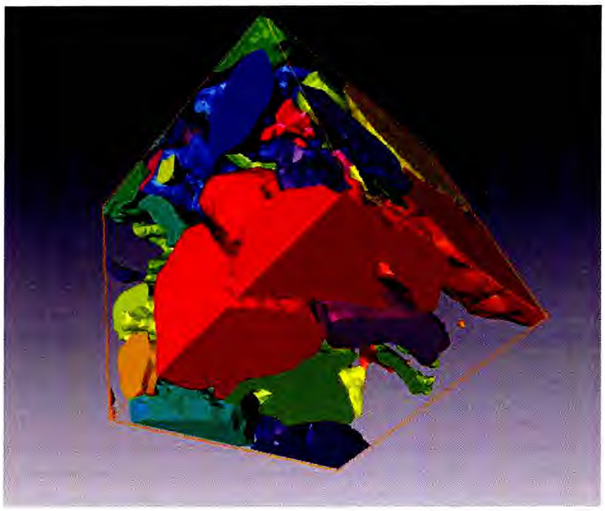

Figure 3.31: 1.44 mm^3 3-D section showing only the pores of the porous extrudate. Segmented pores are shown by different colours.

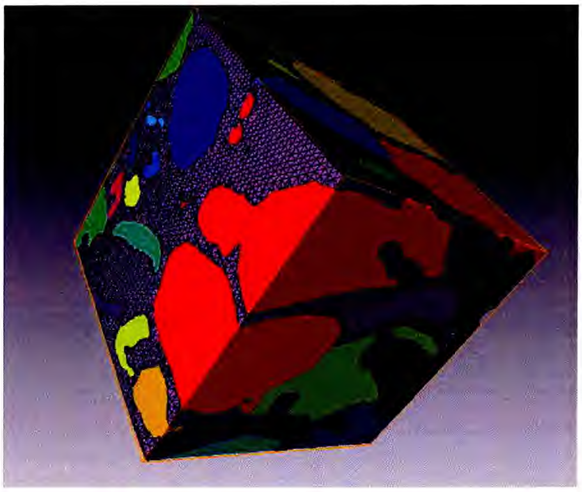

Figure 3.32: 1.44 mm^3 3-D section of the porous sample showing both porous and solid phases. Segmented pores are shown in different colours and the solid phase is meshed (purple).

Pore volumes were taken directly from the segmented 3-D image of the entire sample. Pore size distributions used an equivalent spherical pore diameter, taken from the pore volumes, with a range of 0 mm to 1.75mm. The upper bound corresponds to the maximum pore size observed during analysis. The pore diameter range was split into 20 equal bins of 0.0875mm. Both volume fraction (of the entire sample volume) and number frequency of pores per mm^3 were plotted against pore diameter in order that different dimension and total porosity samples could be fairly compared.

The results can be seen in Figures 3.33 and 3.34. The different plots emphasise different aspects of the pore size distribution, so should be used in combination. Both types of distribution show clear and expected differences in pore structure between the two samples. This shows the strength of using the XMT and watershed technique for obtaining pore size distributions of the entire sample, not just specified volumes of interest.

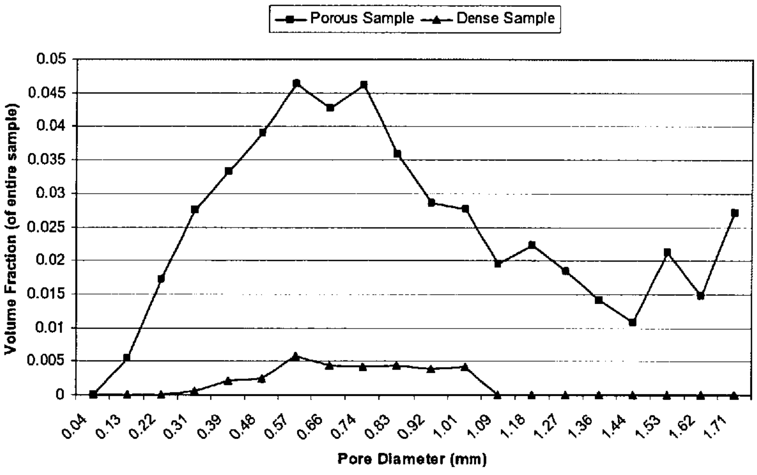

Figure 3.33: Pore size distributions for both the porous and dense samples in terms of volume fraction (of entire sample) versus equivalent spherical pore diameter.

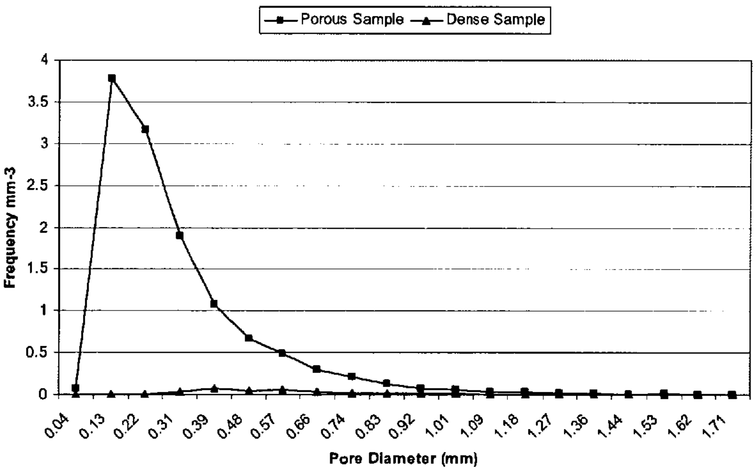

Figure 3.34: Pore size distributions for both the porous and dense samples in terms of number frequency mm^{-3} *versus equivalent spherical pore diameter.*

Pore size distributions for a child volume of the porous product generated using different threshold values are shown in Figure 3.35 and Figure 3.36. The general shape, modal peak positions and y-values of the distributions change very little for different threshold values. This shows that the results are not sensitive to the chosen threshold value (within sensible limits). As the 3-D image is an x-ray of the actual internal structure this shows the accuracy or 'realness' of the pores/pore walls viewed and values extracted from the image. Essentially the results can be seen as 'true'.

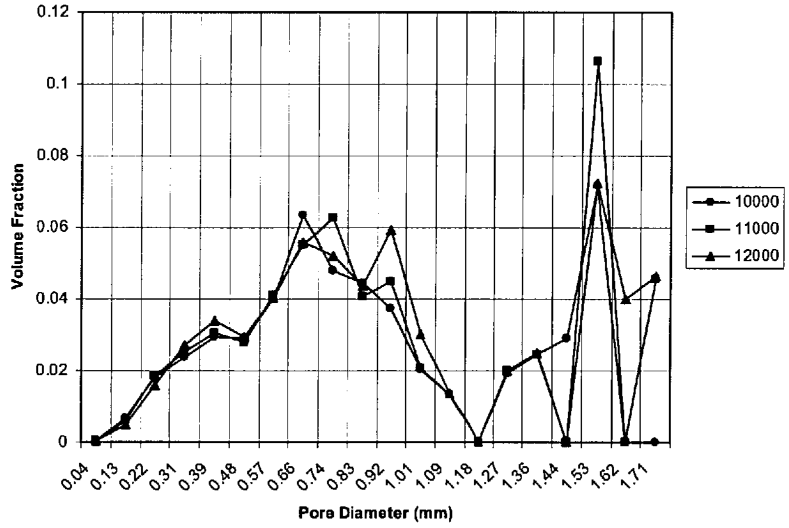

Figure 3.35: Volume fraction pore size distributions for the porous sample using three different threshold contrast values for differentiating between pores and solid phases.

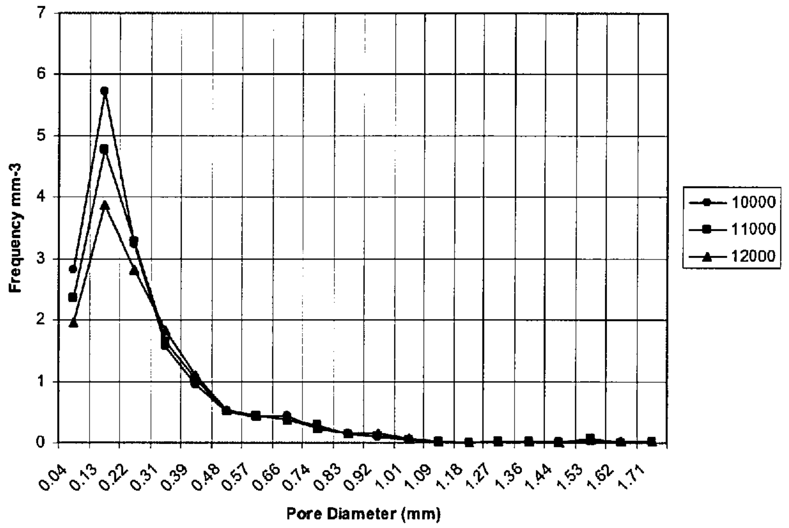

Figure 3.36: Number frequency mm^{-3} pore size distributions for the porous sample using three different threshold contrast values for differentiating between pores and solid phases.

3.3.2. Volume fraction

Results from the three volume fraction methods for both dense and porous samples are shown in Table 3.4. All three methods gave similar (and hence assumed accurate) results. Errors can arise with helium pycnometry of polymeric materials due to helium diffusing into the solid phase thereby under-estimating its volume. The agreement with the image analysis results implies that this is not a significant issue in these materials. However, the threshold contrast value did have a noticeable effect on the pore volume fraction calculated by image analysis. For example the pore volume fraction of the porous sample calculated from 3-D image analysis ranged from 0.43 to 0.55 using the three threshold values mentioned previously (10000, 11000 and 12000). Thus the value from density measurements is likely to be the most reliable.

Table 3.4: Volume fractions of porosity obtained from three different methods for both dense and porous extrudates.

Method	Dense Sample	Porous Sample
2-D Image Analysis	0.04	0.48
3-D Image Analysis	0.04	0.50
Density Analysis	0.05	0.51

3.3.3. Average cell wall thickness

Average pore wall thicknesses were 0.075mm and 1.13mm for the porous and dense extrudates respectively. Manual measurement of numerous pores walls from the three-dimensional tetrahedral mesh confirmed that these values are reasonable. Porous sample walls ranged from 0.043mm to 0.194mm in thickness and dense sample walls ranged from 0.63mm to 5.31mm in thickness.

3.3.4. Structural characterisation discussion and final method

XMT has been shown to be a powerful technique for qualitative and quantitative structural characterisation of open-cell starch extrudates of both low and high relative density/porosity (and assumed all in between). The 3-D watershed algorithm is a suitable method for "closing" open cells and obtaining pore size distributions and interconnecting pore aperture distributions. In addition, the technique can obtain pore size distributions for samples in which the pore structure is not homogeneous throughout the sample. The watershed technique also allows individual pores to be visualised. Volume fractions of porosity from both two-dimensional and three-dimensional image analysis were in good agreement with the results of macroscopic density methods, with density measurement being the preferred method of calculation. Average cell wall thicknesses can also be accurately calculated from two-dimensional image analysis. Combining these methods provides thorough overall characterisation of the internal extrudate pore structure and is ideal for this work where the effect of pore structure on both mechanical measures and acoustic emissions will be considered. These techniques will be used in subsequent sections.

3.4. Expansion Control Chamber Evaluation

The objective of this section is to preliminarily evaluate the use of an Expansion Control Chamber (ECC), supplied by Andritz Sprout, operating on the principle outlined in the extrusion section (3.1.1). The ECC's impact on the extrusion was determined through extruder barrel temperature profile and extrusion pressure. As extrusion parameters were constant the effect of the ECC on extrusion can be judged from the pressure at the extruder internal die face and the temperature profile along the extruder barrel length. Temperature profiles for the eight sample sets are shown in Figure 3.37 with five evenly spaced temperature readings, 248mm apart, along the extruder barrel length. The final temperature (Temp 5) is at the internal surface of the extruder die face. The eight temperature profiles are very similar showing that the thermal energy input during extrusion is not affected by ECC pressure.

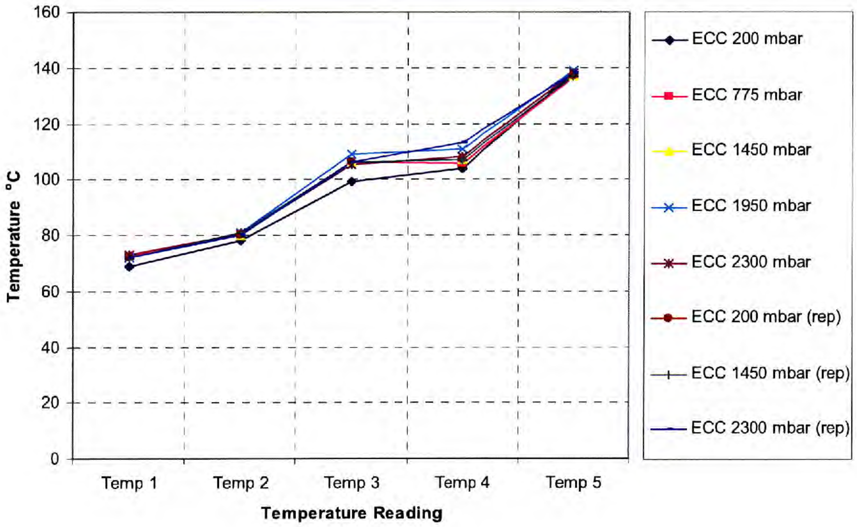

Figure 3.37: Temperature profile along the extruder barrel length for samples produced using different ECC pressures.

Figure 3.38 shows the effect that the ECC pressure had on extrusion pressure. A marginal increase in extrusion pressure was evident only at the lowest ECC pressure. This increase was small (approximately 1 bar) compared with the total pressure inside the extruder (approximately 10.5 bar) and can be assumed to have no significant effect on the extrusion mechanical energy.

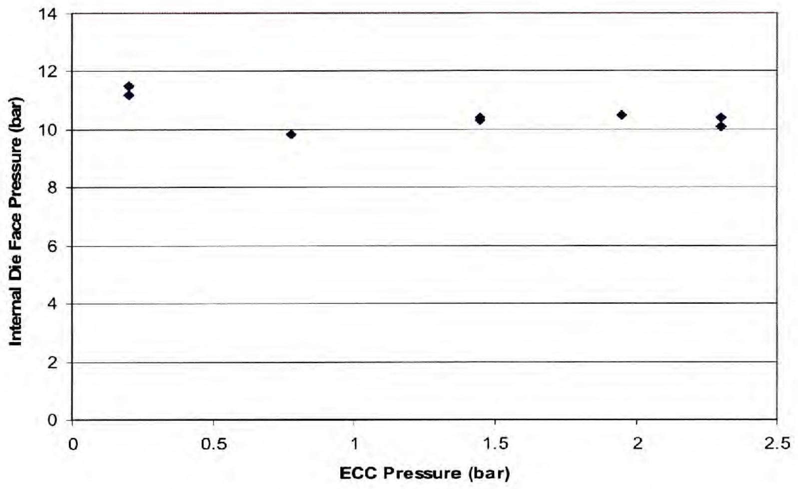

Figure 3.38: Effect of ECC pressure on extrusion pressure (taken at the extruder die face).

Also shown in Figure 3.37 and Figure 3.38 are data for the replicates at the 200, 1450 and 2300 mbar ECC pressures. The temperature profiles and extrusion pressures are seen to be repeatable. These results show the ECC has no significant impact on the extrusion conditions so samples will (nominally), after drying, have the same skeletal material. Prior to drying extrusion moistures ranged from 19.8 to 24.3 wt%, with moisture content increasing with ECC pressure. More information relating to this will be presented in later sections.

4. RESULTS

The Methods chapter (chapter 3) has described the development of methods for capturing mechanical destruction acoustic emissions, structural characterisation and demonstrated the Expansion Control Chamber (ECC) has no significant effect on extrusion. That completes objectives 1-2 as outlined in the Literature Review Discussion (section 2.4), and contributes towards the third objective concerning extrusion expansion control – validation of the ECCs effect on pore structure – which is still required. The completed objectives are;

1. Develop a fully tested mechanical destruction acoustic capture method including investigation of peak origin in the frequency spectra and sample geometry effect.
2. Develop methods for the characterisation of internal extrudate (pore) structure.

Whilst the third objective has been partially addressed;

3. Develop and test a method for controlling extrusion expansion that has no impact on extrudate skeletal material properties (although further evidence will be supplied).

And following on from those objectives are;

4. Investigate the relationships between mechanical properties (real and texture), mechanical destruction acoustic emissions and pore structure.
5. Prove/disprove pore wall vibrations create mechanical destruction acoustic emissions by modelling their vibration.

Investigation of objectives 4 and 5 requires a production method whereby pore structural properties vary in a controlled manner whilst maintaining constant skeletal material properties. It is likely the ECC is the ideal production tool. The sample sets as produced with different ECC pressures will be used to evaluate the effect of the ECC on pore structure. It is hoped this data will then be suitable for use in the investigation of objectives 4 and 5.

One issue in using samples produced with different ECC pressures may arise due to differing expansion affecting geometric properties and in turn acoustic emissions whereas mechanical properties can be normalised for sample size. An initial investigation was therefore conducted into the effect of extrudate diameter on acoustic emissions and is presented next. Further investigation into the effect of the ECC on pore structure and acoustic emissions will then be detailed.

4.1. Geometry

Geometric properties of the extrudate may affect the acoustic emission. Previous preliminary work, as discussed in the literature review, has suggested these properties probably have negligible effect on the acoustic emission. This was investigated in the current study by looking at the effects of sample diameter. Results of this investigation are presented in subsequent sections. If sample diameter does not affect mechanical destruction acoustic emissions and it is later proved that pore walls vibrate creating acoustic emissions, it can be inferred that geometric properties (size and shape) will have no effect on acoustic emissions. This would mean different geometry samples can be compared directly.

4.1.1. Extrusion and dimensions

The theory, upon which the extrusion was based, as discussed in the Extrusion section (3.1.1), should have resulted in similar total energies and SME and STE percentages. Table 4.1 lists the energies as given by the extruder read-outs and logs. Whilst SME energy input was constant, a clear increase in STE, hence total extrusion energy, can be seen for the 7.2mm and 10mm sample sets. This may be expected to impact extrudate internal structure; increased extrusion energy can increase expansion.

Structural characterisation techniques were developed (section 3.3) after completion of this work phase.

Table 4.1: Details of the mechanical, thermal and total energy for the extrusion of four products created to have varying diameter but the same internal structure.

Product	**5mm Product**		**6mm Product**		**7.2mm Product**		**10mm Product**	
SME (Wh/kg)	59.34	62.24%	58.71	61.99%	57.46	52.98%	59.02	54.56%
STE (Wh/kg)	36.00	37.76%	36.00	38.01%	51.00	47.02%	49.15	45.44%
Total Energy (Wh/kg)	95.34	100.00%	94.71	100.00%	108.46	100.00%	108.17	100.00%

Analysis of the results showed the degree of expansion and product lengths were not significantly different for any product. Results can be seen in Table 4.2. This was expected from the experimental design but possibly not due to the differences in extrusion energies shown in Table 4.1. Product diameters were significantly different. Finished product diameters ranged from 7.31mm to 15.40mm as detailed in Table 4.2.

Final product moisture percentage is presented in Table 4.2. The 7.2mm product had significantly lower moisture than the 5mm product and 6mm product. All other moisture comparisons showed no significant difference. The difference for the 7.2mm product is thought due to the limitations in accuracy when using a batch dryer. Due to the combining effect of differences in both product moisture and extrusion energy for the 7.2mm product mechanical test or acoustic emission differences may be expected. It is unclear whether extrusion energy differences alone, as seen for the 10mm product, would be expected to impact on mechanical test or acoustic emission results.

Table 4.2: Product diameter, length, expansion and moisture measurements. The products were produced to be identical bar their diameter.

	Product Diameter (mm)		**Product Length (mm)**		**Degree of Expansion**		**Final Moisture (%)**	
	Average	Std Dev	Average	Std Dev	Average	Std Dev	Average	Std Dev
5mm	7.31	0.24	6.85	0.57	2.14	0.14	6.94	0.36
6mm	9.05	0.37	6.90	0.41	2.27	0.19	7.00	0.61
7.2mm	10.60	0.33	7.10	0.33	2.15	0.14	6.01	0.27
10mm	15.40	0.24	6.95	0.22	2.37	0.11	6.43	0.44

4.1.2. Mechanical (texture) properties

Mechanical test results are summarised in Table 4.3. Figure 4.1 shows the only significant difference in the maximum stress at failure was between the 10mm diameter product and 7.2mm diameter product, with the 10mm diameter product having the lower maximum stress. It is hoped this difference did not impact upon the 10mm diameter product mechanical destruction acoustic emission.

Table 4.3: Mechanical test data for four products produced to have different diameters but the same internal structure.

	Maximum Stress (N/mm^2)		Crispness 1		Crispness 2	
	Average	Std Dev	Average	Std Dev	Average	Std Dev
5mm	0.63	0.17	3.48	0.91	1.66	0.20
6mm	0.56	0.14	2.91	0.60	1.52	0.10
7.2mm	0.60	0.10	9.20	1.37	3.45	0.45
10mm	0.36	0.12	1.61	0.34	1.31	0.07

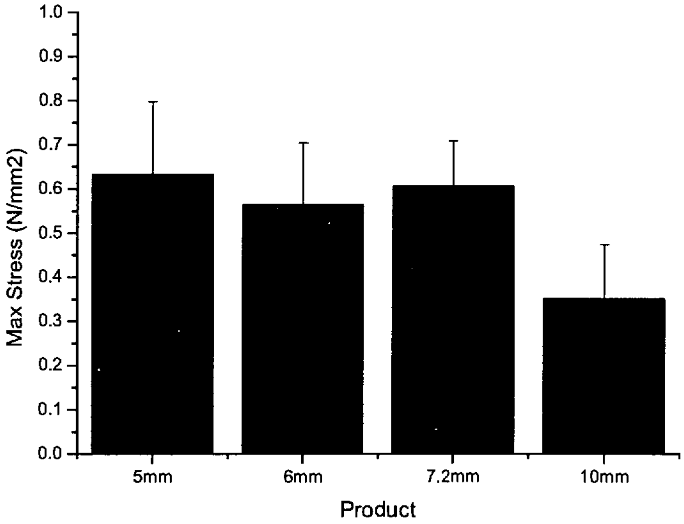

Figure 4.1: The maximum failure stress of four different diameter products. One standard deviation was used as the error limit.

Data for crispness 1 can be seen in Figure 4.2. There is no significant difference between the 5mm product and 6mm product, the 7.2mm product is significantly higher than all three other products, whilst the 10mm product has a significantly lower crispness 1 than all other products. The difference between the 5mm and 6mm products and the 10mm product is small, whilst the 7.2mm product has a much higher crispness than all three other products. Crispness 1 is thought to be directly related to product porosity and has been linked with sample moisture; lower moisture results in higher crispness (McGrane 2004). The higher value for crispness 1 fits with extrusion energy and moisture results presented previously.

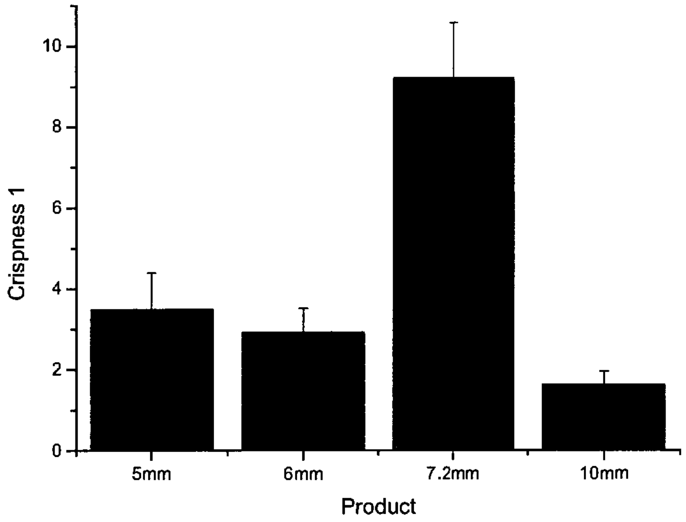

Figure 4.2: Crispness 1 results of four different diameter products. One standard deviation was used as the error limit.

Crispness 2 yields the same relative ranking as crispness 1 as detailed in Figure 4.3. This suggests a definite structural difference in the 7.2mm product, likely due to extrusion energy and sample moisture. Analysis of the internal structure would be required to fully describe reasons for this difference. An increased number of pores is one possibility as crispness values are often proportional to this. Any internal structure difference would be expected to impact upon mechanical destruction acoustic emissions considering previous work.

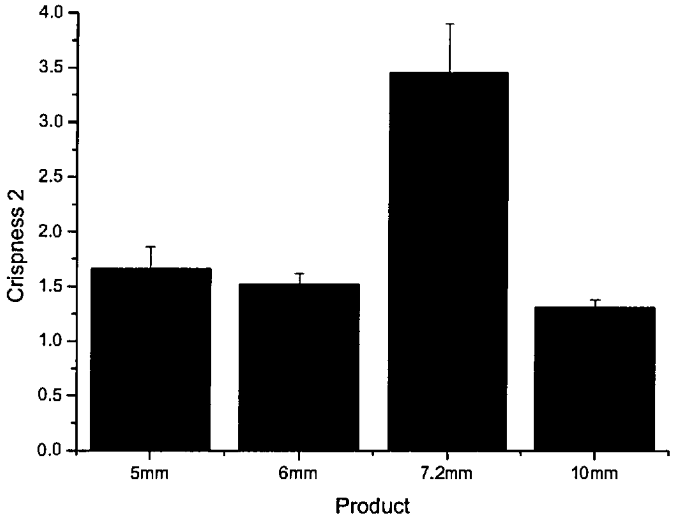

Figure 4.3: Crispness 2 results for four different diameter products. One standard deviation was used as the error limit.

Increased extrusion thermal energy would be expected to increase expansion, hence crispness, if it has any effect. This is not the case for the 10mm product which showed a marginally lower crispness. For this reason the impact of extrusion energy on the 10mm product was assumed negligible.

4.1.3. Acoustic

Figure 4.4, Figure 4.5 and Figure 4.6 represent the average frequency spectra for the products in various graphical formats. All three representations show there to be only small difference in the frequency spectra for each product.

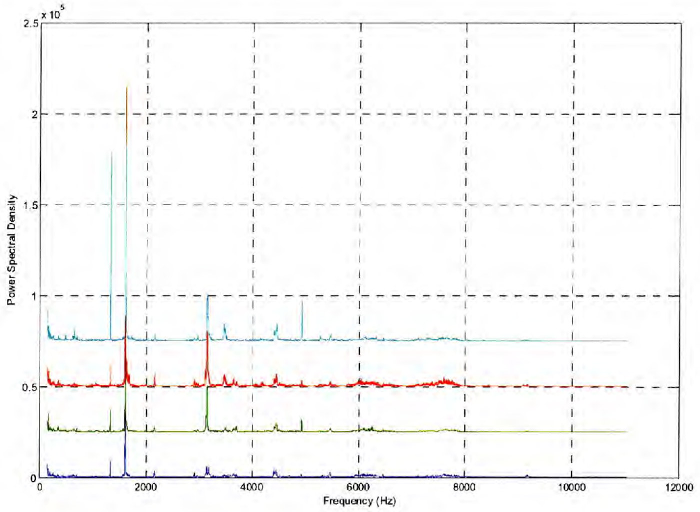

Figure 4.4: Average frequency spectra (from ten repeats) for four different diameter products. The bottom spectrum is that of the 5mm product, the 6mm product spectrum is offset on the y-axis by 25000, the 7.2mm product is offset by 50000 and the 10mm product is offset by 75000.

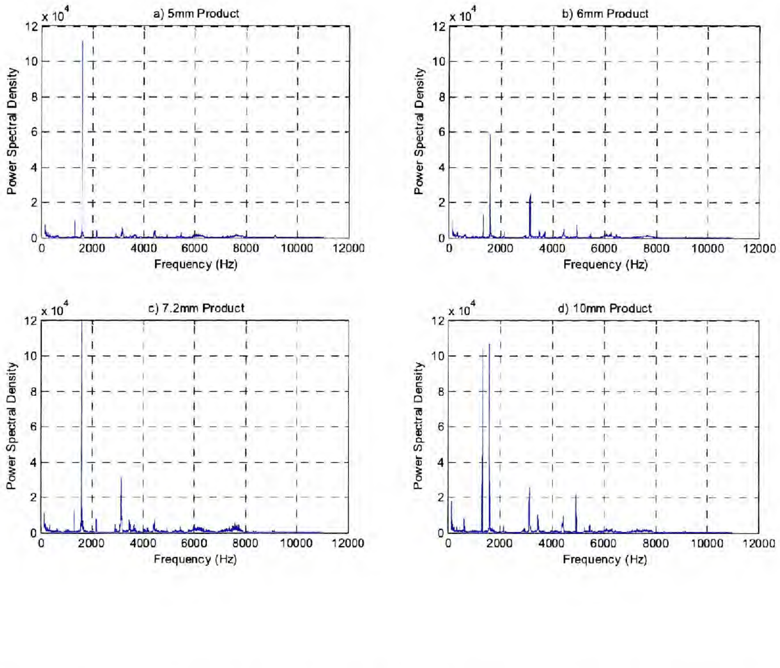

Figure 4.5: The average frequency spectra (from ten repeats) for four different diameter products plotted on the same scale graphs. (a) is the 5mm product, (b) is the 6mm product, (c) is the 7.2mm product and (d) is the 10mm product.

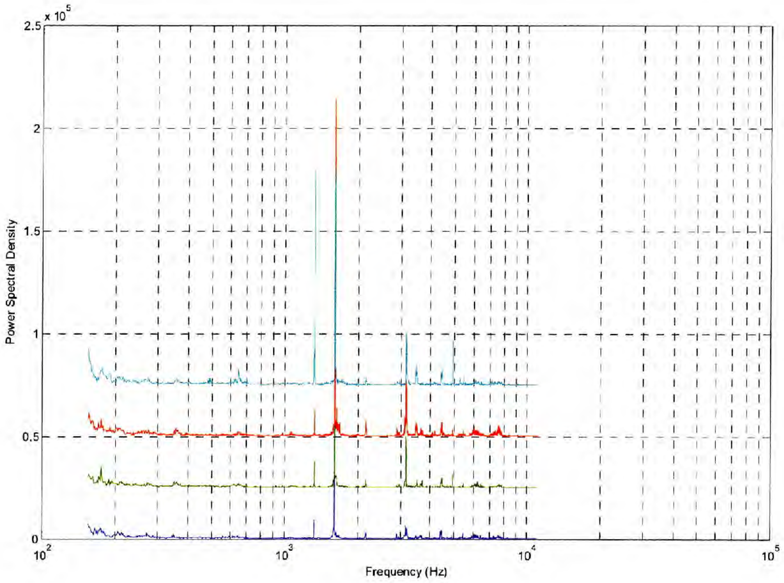

Figure 4.6: The average frequency spectra (from ten repeats) for four different diameter products plotted using a log scale for the x-axis. The bottom spectrum is that of the 5mm product, the 6mm product spectrum is offset on the y-axis by 25000, the 7.2mm product is offset by 50000 and the 10mm product is offset by 75000.

Figure 4.4 and Figure 4.5 show all samples have frequency peaks in the same places, but there are differences in intensities for the same frequency peaks. All peaks, bar at 1700Hz, are distinctly weaker for the 5mm product, and weaker for the 6mm product. This may imply smaller products either have not got enough acoustic energy available or cannot contain all acoustic vibratory components. These differences are common across all repeats.

Figure 4.6 shows the frequency spectra using a log scale for the frequency axis, accentuating the lower frequency peaks. No differences can be seen in the spectra for the different diameter products at low frequencies.

Although Figure 4.4 and Figure 4.5 show the same peak positions, but different peak intensities, it can be noted that the general 'shape' of the spectra and their relative intensities are similar. Figure 4.7 shows the frequency spectra of the repeats for the 7.2mm product and demonstrates this general shape is common for all repeats, but there are marked differences in the intensities for the same frequency across repeats. This begs the question, again, whether peak position, peak intensity or a combination are important. Previous work has described product differences through peak position whilst this study has suggested peak intensity is only important when large differences are seen; larger than the differences in intensity seen in the repeats of the 7.2mm product in Figure 4.7.

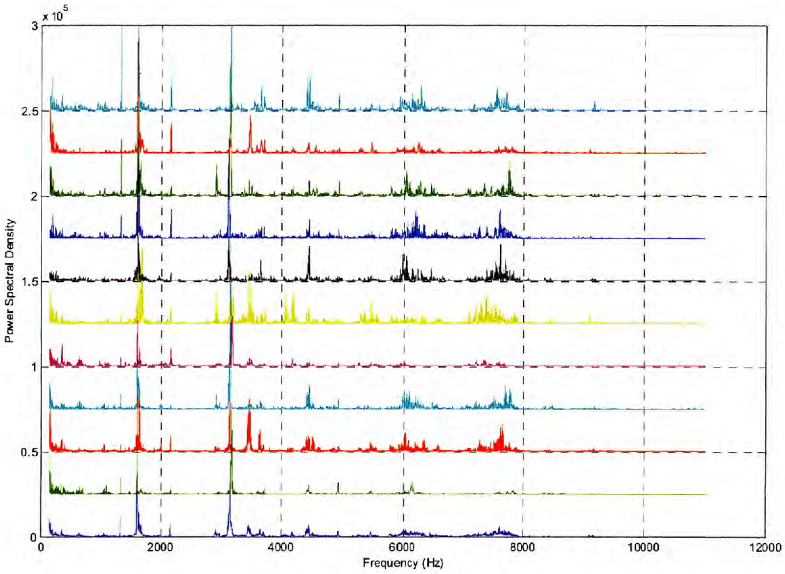

Figure 4.7: The acoustic frequency spectra, as generated by mechanical destruction, of ten repeats of the 7.2mm product. Each spectrum is offset on the y-axis by 25000. The bottom spectrum is the average of the ten repeats.

Figure 4.8 shows all repeats for the 5mm product. It can be seen the peaks are much weaker than those of the 7.2mm product. Furthermore there is much more variability in the 5mm product repeats than those of the 7.2mm product, with each repeat not showing the same general shape and large differences in peak intensity. The similarities as seen with the 7.2mm product are closer to a 'normal' set of data. Issues with the 5mm product may be due to its small size as mentioned previously. These results may imply a lack of all acoustic vibratory components in a single extrudate when the extrudate is so small.

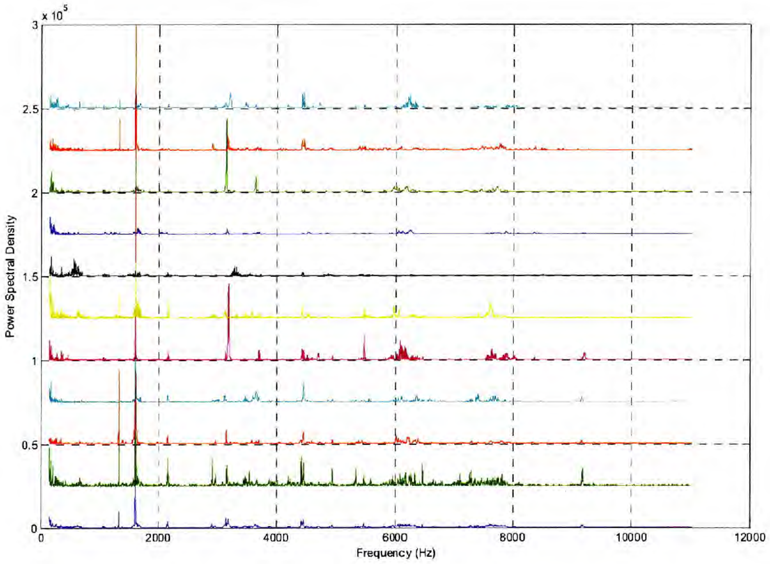

Figure 4.8: The acoustic frequency spectra, as generated by mechanical destruction, of ten repeats of the 5mm product. Each spectrum is offset on the y-axis by 25000. The bottom spectrum is the average of the ten repeats.

Signal energy and maximum sound pressure results can be seen in Figure 4.9 and Figure 4.10 respectively. There is no significant difference in the data for both signal energy and maximum sound pressure. This shows acoustic differences in the 5mm product repeats are not due to the total acoustic energy available being low. Tests on breakfast cereals with different moisture levels have also been shown to have no effect on acoustic signal energy (Gondek, Lewicki et al. 2006).

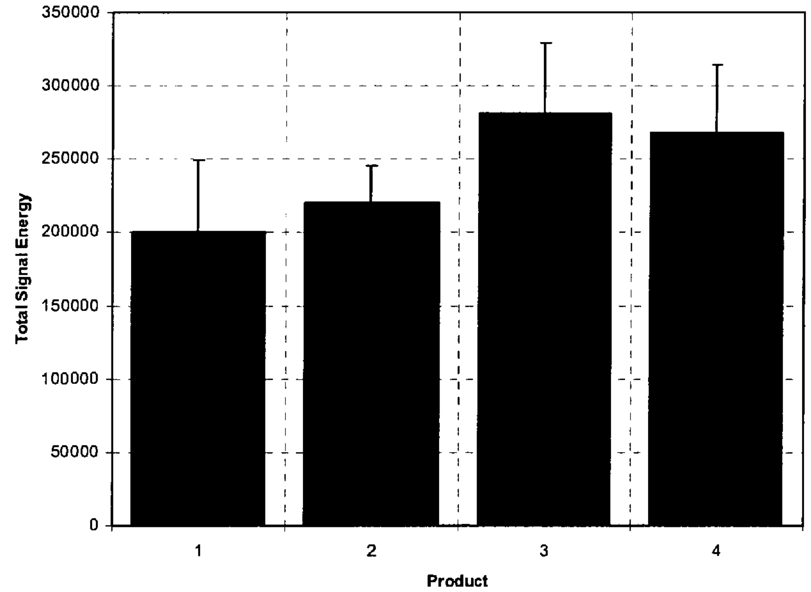

Figure 4.9: The average total signal energy for four different diameter products. 1 corresponds to the 5mm product, 2 the 6mm product, 3 the 7.2mm product and 4 the 10mm product. One standard deviation was used as the error margin.

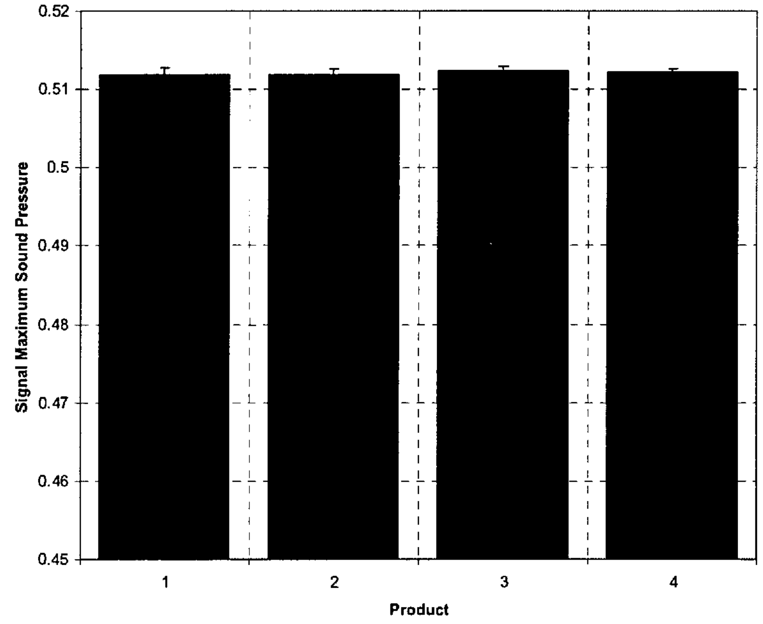

Figure 4.10: The average maximum sound pressure for four different diameter products. 1 corresponds to the 5mm product, 2 the 6mm product, 3 the 7.2mm product and 4 the 10mm product. One standard deviation was used as the error margin.

4.1.4. Diameter trial discussion

Extrusion energies, sample moisture, sample dimensions and degree of expansion have shown sample production was consistent with theoretical expectations bar the 7.2mm product. This should result in a similar internal structure for all except the 7.2mm product.

Mechanical test analysis showed all products to be similar bar the 7.2mm product which had much greater crispness 1 and crispness 2 values. This was not expected from the theory but predicted from other product and extrusion data and may indicate a different internal structure.

The average frequency spectra showed little if any difference with products of different diameter confirming earlier work. Small differences may be seen with the 5mm product but this maybe due to the small size meaning the samples did not contain all acoustic vibratory components.

From the mechanical test data a difference in the acoustic spectrum of the 7.2mm product would be expected. This was not seen in the average spectra. The frequency spectra repeats for the 7.2mm product are shown in Figure 4.7. Figure 4.11 shows the frequency spectra repeats for the 10mm product. It can be noted the 7.2mm product repeats have consistently higher intensities in the 6000-8000Hz frequency range compared with the 10mm product. This was not clearly seen in the averages and demonstrates a weakness in using averages alone.

Defining a spectral difference is difficult. Previous work has shown peak position to be important. The difference in the 6000-8000Hz region of the 7.2mm product demonstrates the importance peak intensity may also play in characterising the acoustic emission. Viewing the repeats as well as the average may be required for analysis, or focussing on specific sections of the frequency spectra.

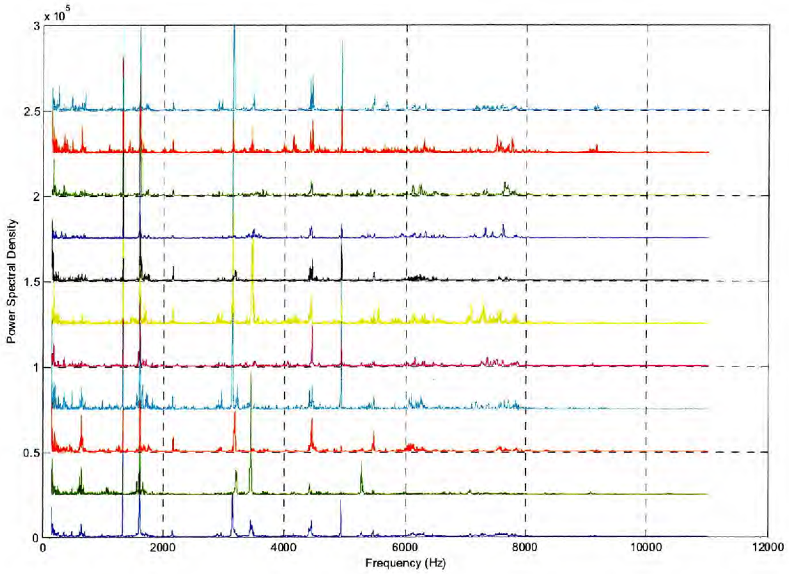

Figure 4.11: The acoustic frequency spectra, as generated by mechanical destruction, of ten repeats of the 10mm product. Each spectrum is offset on the y-axis by 25000. The bottom spectrum is the average of the ten repeats.

In summary, some acoustic emission differences have been seen between extruded products having different diameters and nominally the same internal structure. However, these differences can be assigned to product properties other than diameter i.e. they do probably have differences in internal structure despite being nominally the same. The experiment attempted to keep these additional properties constant. Dimension and extrusion results implied the experimental design was sound, except for differences seen in the 7.2mm product mechanical tests; however these results ultimately fit with additional product and process data. Analysis of sample internal structure will be required to consider this further. However, it does appear extrudate geometric properties do not affect the frequency spectra of acoustic emissions produced during mechanical destruction meaning the acoustic emissions of different geometry samples can be compared directly.

4.2. Expansion Control Chamber Samples

This work has previously shown the ECC to have no significant effect on extrusion conditions (section 3.4). This should in turn mean there is no influence of ECC pressure on extrudate skeletal material. For this section skeletal material and sample expansion were investigated using the characterisation techniques developed in section 3.3 (Structural Characterisation), and related to extruder barrel temperature profile and extrusion pressure.

4.2.1. Effect of ECC on solid material

As the ECC showed no significant effect on extrusion, it follows that the eight samples produced with different ECC pressures should have the same skeletal material after drying to the same wt% moisture. Skeletal densities for all eight samples were within an acceptable range to be considered the same, that being 1.381g/cc to 1.476g/cc [see Table 4.4a], – skeletal density measurements for the same product have been shown to have a range of 0.09g/cc previously [see Table 4.4b] – as well as demonstrating no trend with ECC pressure. This indicates the extrusion had no substantial effect on skeletal material.

Table 4.4: Helium pycnometry data for (a) eight samples produced at different ECC pressures and (b) the repeats taken for one random sample set.

(a) Sample	ECC Pressure (mbar)	Skeletal Density (g/cc)
ECC 1	200	1.4108
ECC 2	775	1.4068
ECC 3	1450	1.4760
ECC 4	1950	1.4479
ECC 5	2300	1.4156
ECC 6	200	1.4679
ECC 7	1450	1.4684
ECC 8	2300	1.3809
Range		0.0951
Std Dev		0.0353

(b) Reading	Skeletal Density (g/cc)
1	1.4074
2	1.4196
3	1.4129
4	1.3731
5	1.4025
6	1.4103
7	1.4454
8	1.4665
Range	0.0933
Std Dev	0.0281

4.2.2. Effect of ECC on pore structure

The pore structures are created by the flash-off of steam, accompanied by expansion, as the dough exits the extruder. Expansion can be quantified using volume fraction porosity and degree of expansion. Figure 4.12 and Figure 4.13 show ECC pressure has a high correlation to both volume fraction porosity and degree of expansion.

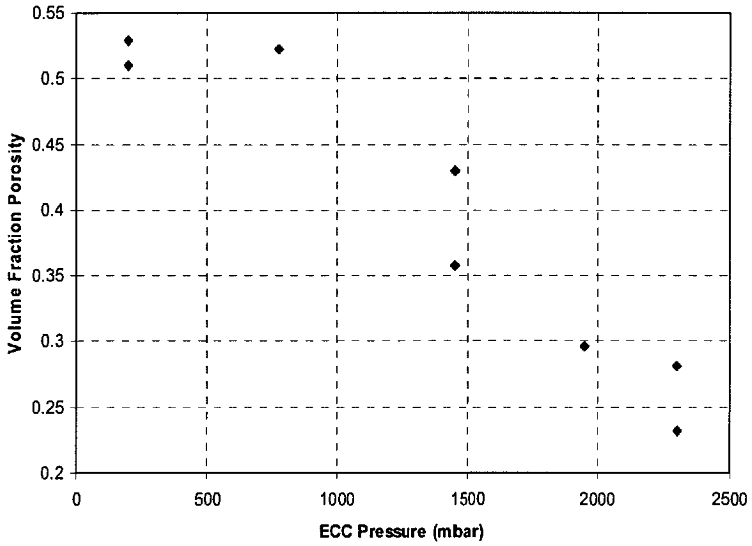

Figure 4.12: A graph showing the effect of ECC pressure on volume fraction porosity.

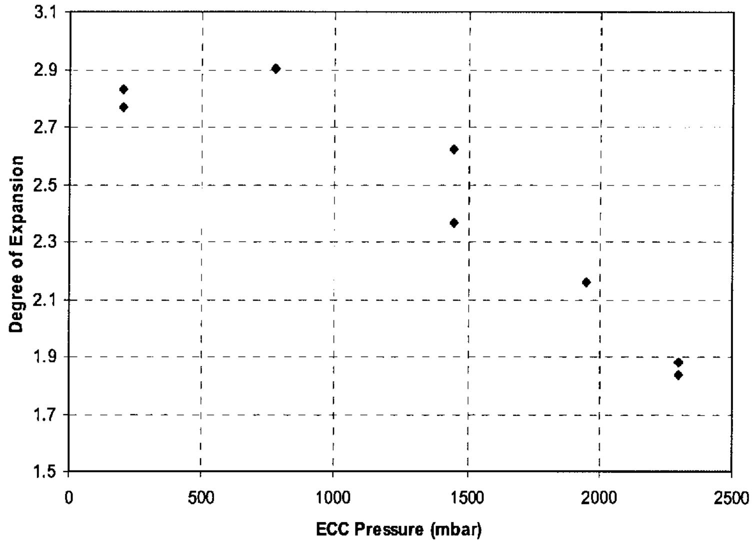

Figure 4.13: A graph showing the effect of ECC pressure on degree of expansion.

Over the range of ECC pressures studied both volume fraction and degree of expansion decrease with increasing ECC pressure. However, both show little response to ECC pressure until after approximately 775 mbar.

Pore size distributions, (frequency and volume weighted) mean pore sizes and average pore wall thicknesses were computed from the XMT data. Figure 4.14 shows the volume fraction (of the entire sample) pore size distributions and Figure 4.15 the number frequency mm^{-3} pore size distributions for all eight samples.

Considering volume fraction pore size distributions there is no clear dependence of the volume of the smaller size pores on ECC pressure with differences appearing random. However, for larger pores it appears a lower ECC pressure generally increases the volume fraction of those pores. This is not true in all cases as one of the 2300mbar samples has a high volume fraction for the largest pore size range.

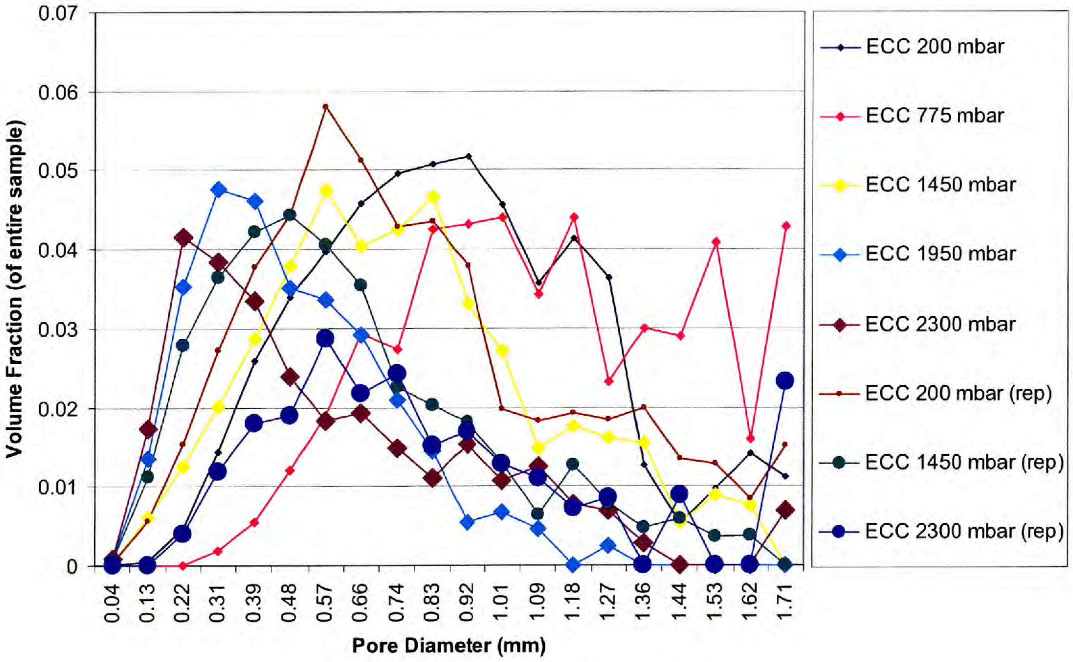

Figure 4.14: Volume fraction pore size distributions for all eight samples produced with different ECC pressure. Increased ECC pressure is represented by increased data-point marker size.

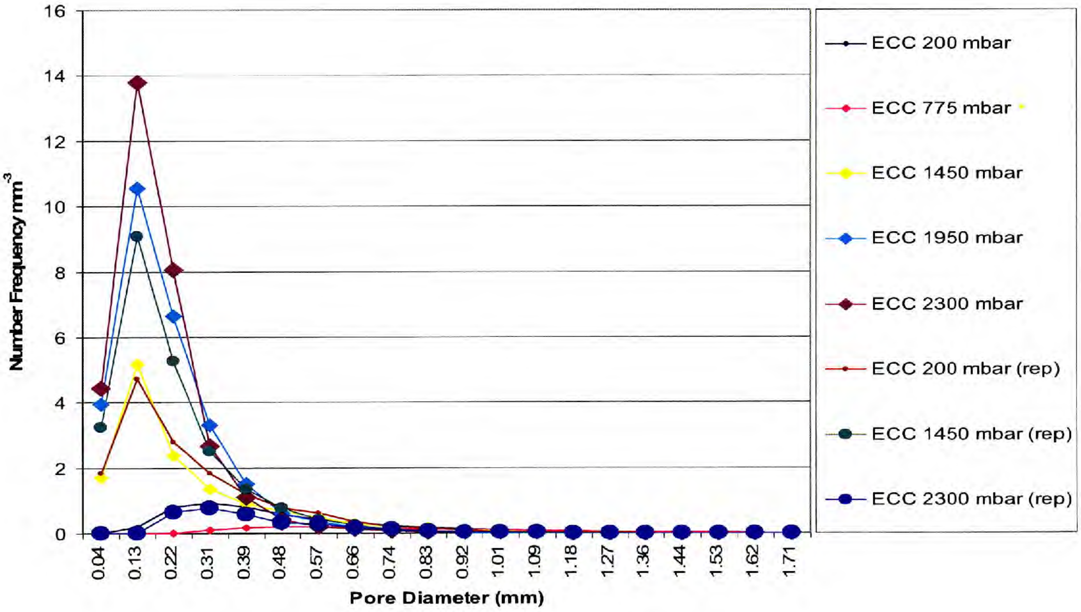

Figure 4.15: Number frequency mm^{-3} pore size distributions for all eight samples produced with different ECC pressures. Increased ECC pressure is represented by increased data-point marker size.

Number frequency mm^{-3} pore size distributions show a tendency for high ECC pressures to produce a greater number of smaller pores. This trend does not hold for all samples. However, as the pores are small they have little impact on volume fraction distributions.

To further understand the pore structure, volume weighted and frequency weighted mean pore diameter were calculated as can be seen in Figure 4.16 and Figure 4.17 respectively. No significant trends can be seen in the data; however, a slight decrease in volume weighted mean pore diameter with increased ECC pressure could be suggested.

Considering both pore size distributions and mean pore sizes there is no clearly definable effect ECC pressure has on pore size. The ECC pressure does appear to have more of an effect on larger pores with a lower ECC pressure giving a greater volume fraction of pores. This is as expected from the theory upon which the ECC is based. However, differences in repeats show an element of randomness in the distributions and imply ECC pressure is not the dominant factor influencing pore size.

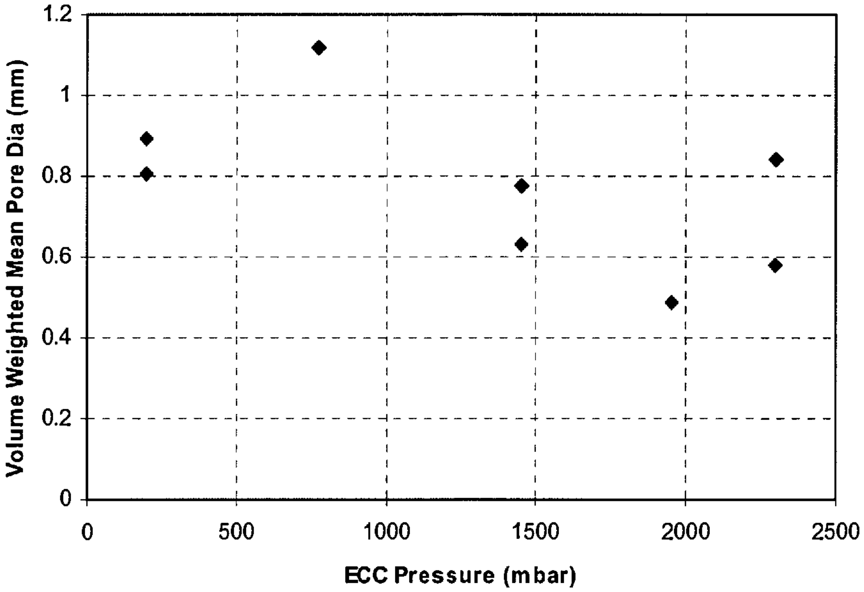

Figure 4.16: A scatter chart of ECC pressure effect on volume weighted mean pore diameter for eight samples produced with different ECC pressures.

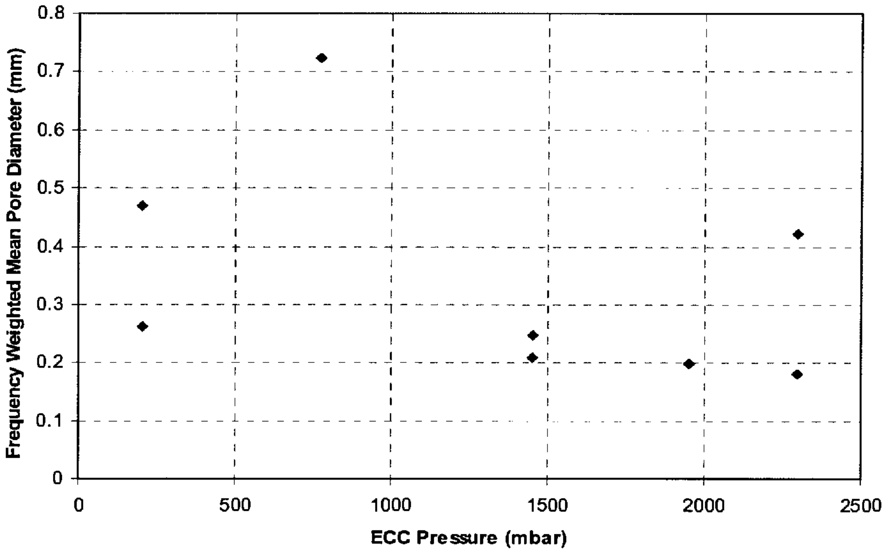

Figure 4.17: A scatter chart of ECC pressure effect on frequency weighted mean pore diameter for eight samples produced with different ECC pressures.

Viewing cross-sectional XMT images reveals that ECC pressure has a distinct effect on the uniformity of the pore structure. Figure 4.18 shows the cross-section of a sample expanded using 200 mbar ECC pressure and Figure 4.19 is that of a sample expanded at 2300 mbar ECC pressure. The higher ECC pressure produced jagged irregular shaped pores, whilst the lower ECC pressure produced more regular shaped smooth "spherical" pores.

Figure 4.18: Cross-section XMT image of the specimen expanded at an ECC pressure of 200 mbar. Both solid and external air shown as black.

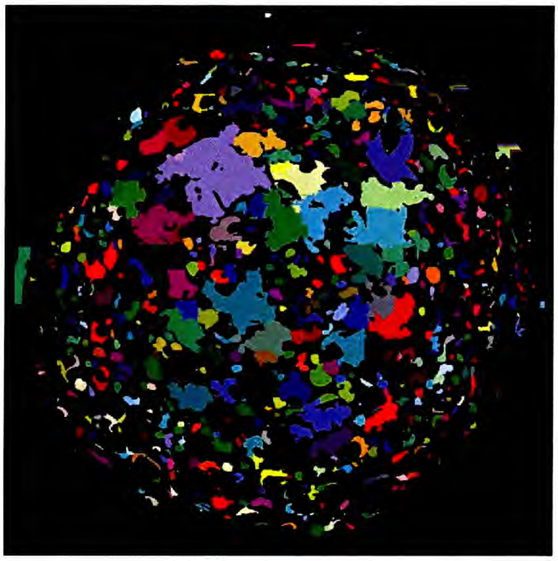

Figure 4.19: Cross-section XMT image of the specimen expanded at an ECC pressure of 2300 mbar. Both solid and external air shown as black.

The average pore wall thickness correlated well with ECC pressure (Figure 4.20). This implies the ECC is a good production tool for controlling average pore wall thickness. Greater ECC pressure increases average pore wall thickness (accompanied by decreased volume fraction porosity and degree of expansion).

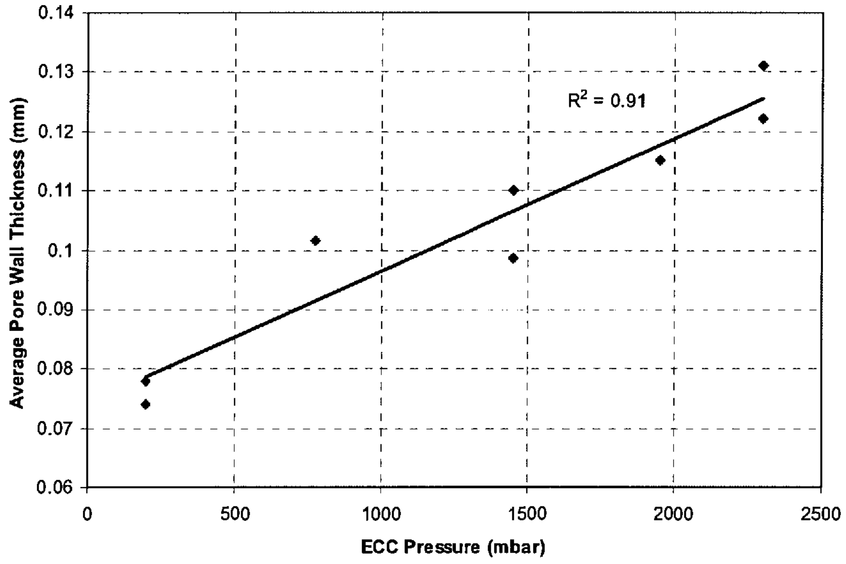

Figure 4.20: The effect of ECC pressure on average pore wall thickness and a linear fit.

4.2.3. Summary

The ECC decreased product expansion as the pressure inside the sealed knife housing was increased with no significant effect on extrusion pressure or temperature, hence skeletal material. This means product expansion for scientific analysis or product production can be controlled. Altering ECC pressure also exhibits a high level of control over average pore wall thickness with increased ECC pressure increasing pore wall thickness. The effect of ECC pressure on pore sizes is not well defined and it appears not to be the primary factor influencing pore size. However ECC pressure does appear to have an effect on the pore volumes associated with larger pores; lower ECC pressures tend to give a greater volume fraction. The ECC can be used as a production tool in this project to investigate the effect of volume fraction and pore wall thickness (but not independently) on acoustic properties, mechanically measured texture and elastic modulus with no effect on skeletal material. The results for products described within this section will be used through the rest of this thesis to aid interpretation of mechanical properties and acoustic emission.

4.3. Acoustic Emission

Capture and analysis of mechanical destruction acoustic wave-forms was conducted as described in section 3.2.4 (Final acoustic method) on the eight ECC samples as discussed in the previous section (and produced as described in section 3.1.1). This provides average frequency spectra, average total signal energy, average maximum sound pressure and average ring down count (RDC) for each sample. Twenty repeat recordings were taken for each sample set. This section presents the acoustic analysis results in their basic form for their use in later sections.

4.3.1. Frequency spectra

Average frequency spectra for the eight ECC sample sets are presented in Figure 4.21 using a normal scale for the frequency axis and Figure 4.22 using a log-scale for the frequency axis.

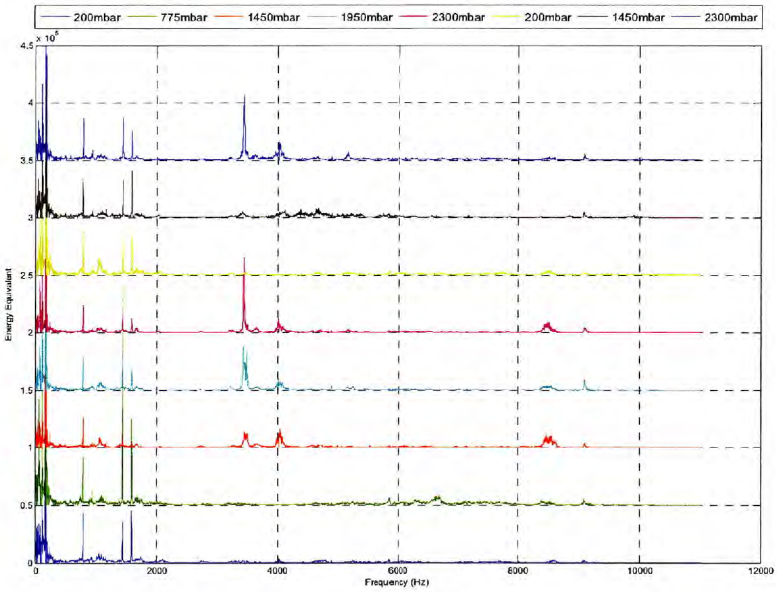

Figure 4.21: Average frequency spectra (from twenty repeats) for eight products extruded at different ECC pressures. Each product is separated by 50000 on the y-axis.

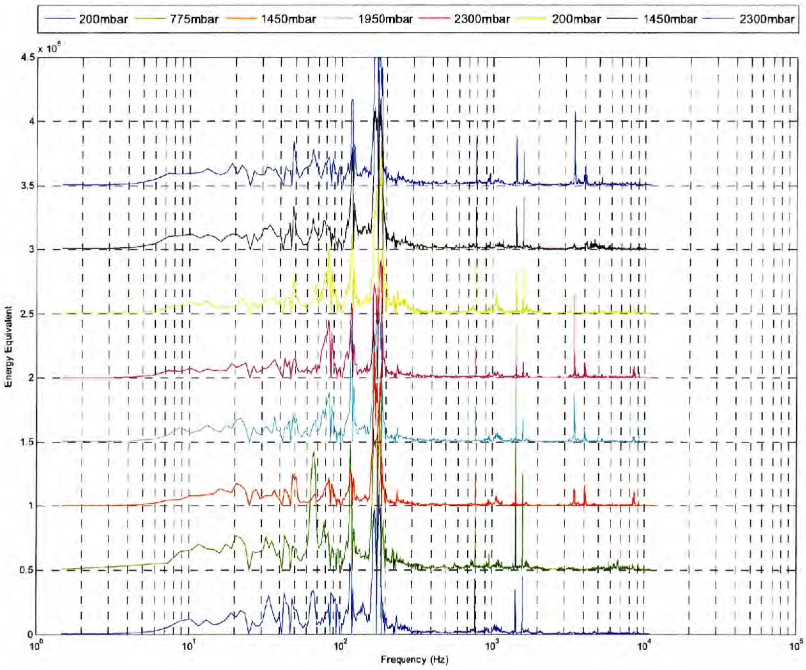

Figure 4.22: Average frequency spectra (from twenty repeats) for eight products extruded at different ECC pressures with the x-axis (frequency) plotted using a log scale. Each product is separated by 50000 on the y-axis.

There are clear differences and similarities in both peak position and peak intensity for different sample sets. Using a log-scale shows no clearly discernable difference between sample sets at lower frequencies (less than 2kHz). Differences and similarities will be discussed in more detail later. Please note, differences and similarities are common across all repeats.

4.3.2. Other acoustic parameters

Numerical data for RDC, signal energy and maximum sound pressure can be seen in Table 4.5. No significant difference, using one standard deviation as the error margin, was seen for any acoustic parameter. However, differences in average values were more obvious with RDC than signal energy and maximum sound pressure. Whilst no significant differences were seen using one standard deviation, analysis of variance (ANOVA) gave significant differences between RDC data sets for different samples.

For these reasons RDC was used in further analysis whilst signal energy and maximum sound pressure were not.

Table 4.5: Average values for the acoustic parameters ring down count, signal energy and maximum pressure of sample sets extruded at different ECC pressures. Standard deviations are also included.

	Ring Down Count		**Signal Energy**		**Maximum Pressure**	
	Average	Std Dev	Average	Std Dev	Average	Std Dev
ECC1	860	250	242000	28000	0.76	0.04
ECC2	960	300	244000	24000	0.74	0.04
ECC3	860	230	270000	35000	0.74	0.05
ECC4	810	270	316000	46000	0.78	0.03
ECC5	740	150	251000	43000	0.77	0.03
ECC6	930	230	267000	41000	0.76	0.04
ECC7	990	190	342000	39000	0.78	0.03
ECC8	890	250	310000	73000	0.76	0.05

4.4. Mechanical Properties

Mechanical testing results are presented in two sections, Mechanical texture (4.4.1) and Elastic modulus (4.4.2). Details and definitions of mechanical test parameters can be found in section 3.15 (Mechanical). Testing was conducted on the eight sample sets produced with different ECC pressures. This section presents the mechanical testing results in their basic form for their use in later sections.

4.4.1. Mechanical texture

Table 4.6 shows results for maximum stress, crispness 1 and crispness 2. Column charts for each parameter are shown in Figure 4.23 through Figure 4.25.

Table 4.6: Mechanically measured textural parameters of maximum stress, crispness 1 and crispness 2 for eight sample sets produced using different ECC pressures.

	ECC Pressure (mbar)	**Maximum Stress (N/mm^2)**		**Crispness 1**		**Crispness 2**	
		Average	Std Dev	Average	Std Dev	Average	Std Dev
ECC1	200	1.0290	0.3202	3.18	0.69	1.34	0.05
ECC2	775	1.0697	0.3740	4.29	0.87	1.48	0.12
ECC3	1450	1.5692	0.6069	3.61	0.79	1.43	0.08
ECC4	1950	1.8880	0.6147	3.08	0.64	1.43	0.09
ECC5	2300	2.0157	0.4669	2.43	0.66	1.37	0.06
ECC6	200 (rep)	0.6669	0.2878	4.48	1.00	1.58	0.11
ECC7	1450 (rep)	2.3693	0.3337	3.47	0.80	1.43	0.07
ECC8	2300 (rep)	1.6895	0.4200	3.43	0.89	1.49	0.08

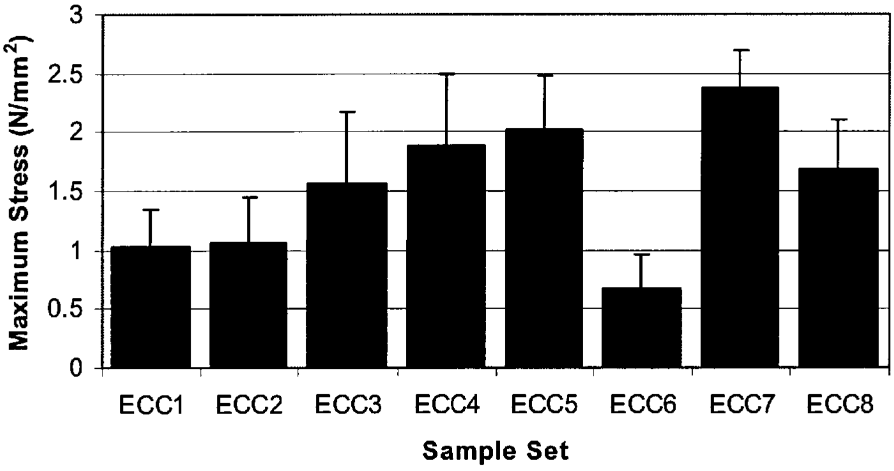

Figure 4.23: Maximum stress for eight sample sets extruded at different ECC pressures. One standard deviation was used for the error limits.

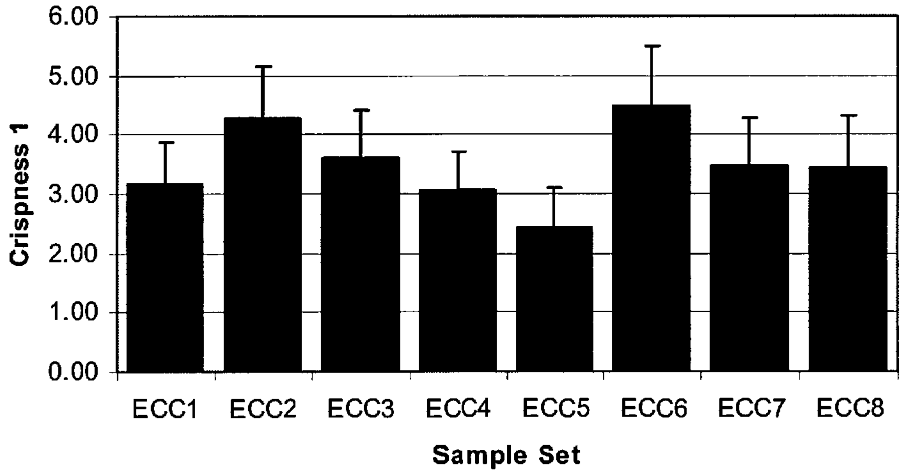

Figure 4.24: Crispness 1 for eight sample sets extruded at different ECC pressures. One standard deviation was used for the error limits.

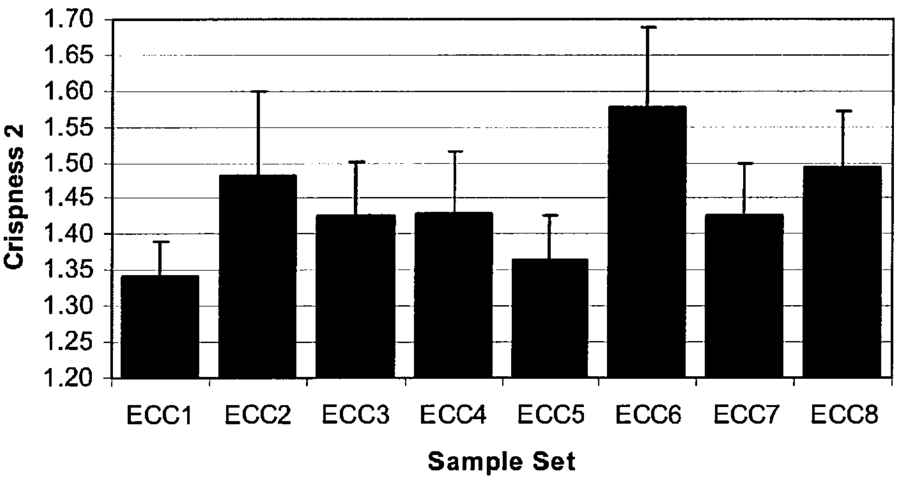

Figure 4.25: Crispness 2 for eight sample sets extruded at different ECC pressures. One standard deviation was used for the error limits.

The range seen for maximum stress was 0.67Nmm^{-2} to 2.37Nmm^{-2}, with significant differences between samples. The range for crispness 1 was 2.43 to 4.48. Some significant differences were seen. Crispness 2 follows the same order of ranking as crispness 1. However, differences between samples are smaller than those seen with crispness 1. Due to this crispness1 was used in future analysis whilst crispness 2 was not. This data will be used in later sections for relationships to pore structure and acoustic emissions.

4.4.2. Elastic modulus

Two standard methods were attempted for measurement of elastic modulus, those being the impulse excitation technique and a four-point bend test as described previously (section 3.1.4.2). Frequency readings, hence elastic modulus measurements, were not reproducible when using the impulse excitation method for both disc and bar samples. This could be due to the inhomogeneous nature of sample porosity (the theory is based on a homogenous zero porosity solid) or peculiar dimensions compared with those of samples normally used. The impulse excitation technique was deemed inappropriate for extrudate materials and therefore not used further.

Bars were fashioned from extruded ropes in order to conduct four-point bend tests. Three photographs of one such bar, taken from different perspectives, can be seen in Figure 4.26. The images demonstrate the accuracy with which parallel surface bars can be made from extruded ropes using the metal 'mould' and fine sand paper.

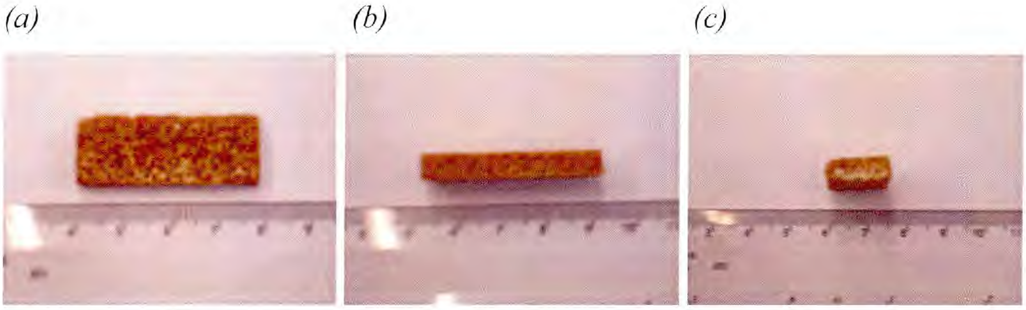

Figure 4.26: Different perspective images showing a bar made from an extruded rope. (a) shows the length and width, d, (b) the length and height, h, whilst (c) shows the width, d, and height, h (refer equation 3.1 for defintions).

When force is applied to an elastic sample the linear range of the force-displacement curve indicates the elastic region. When calculating elastic modulus from four-point bend test data, measurements must only be made over this elastic (and hence recoverable) region of sample deformation. The force-displacement response should be reproducible using the same sample and test conditions, moving up and down the linear elastic displacement range. Figure 4.27 shows the force-displacement curve to the point of fracture for a bar sample extruded at 2300mbar ECC pressure.

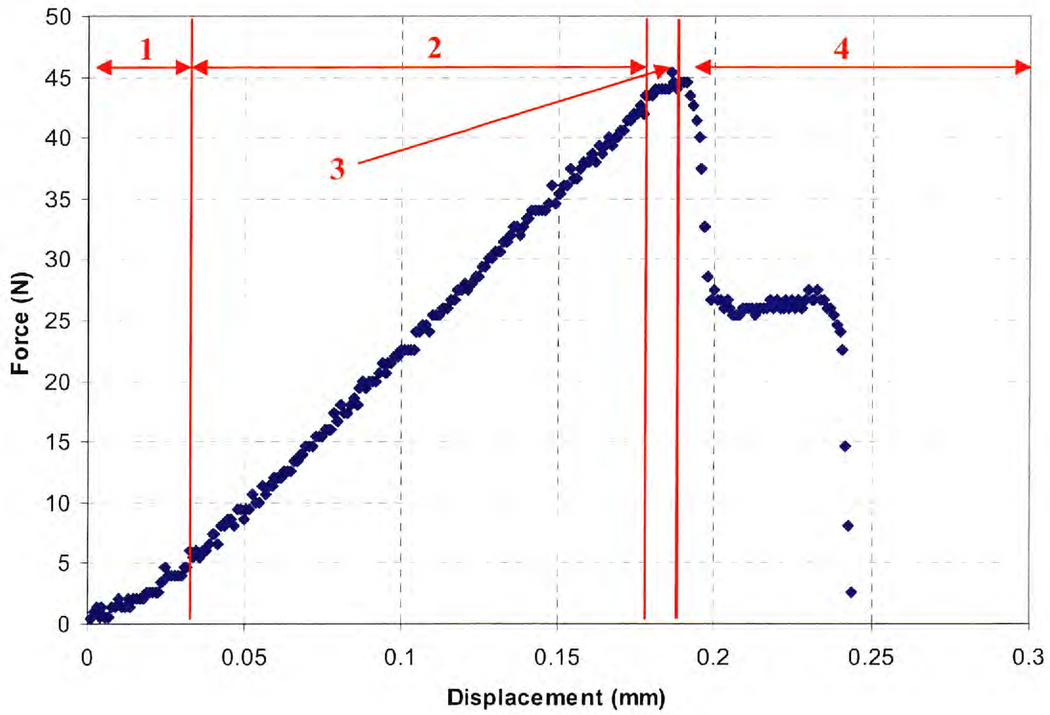

Figure 4.27: Force displacement curve for a bar created from a sample extruded at 2300mbar ECC pressure during four-point bending. The curve is separated into four distinct regions. 1: settling down, 2: elastic, 3: plastic deformation, and 4: fracture.

Four distinct regions can be observed on the force displacement curve in Figure 4.27 (detailed 1-4). Elastic modulus measurement is concerned with region 2, the linear elastic region. When a test is conducted over the elastic region an initial cycle must be completed so the test rig 'settles down' at the contact points, etc. as shown with Figure 4.27 region 1. Following this it should be possible to ramp up and down the elastic region. The elastic limit (boundary of 2-3) of the sample must not be exceeded as after this point plastic deformation occurs and the material properties change. Results from the repetitive cycling of this linear elastic region are shown in Figure 4.28.

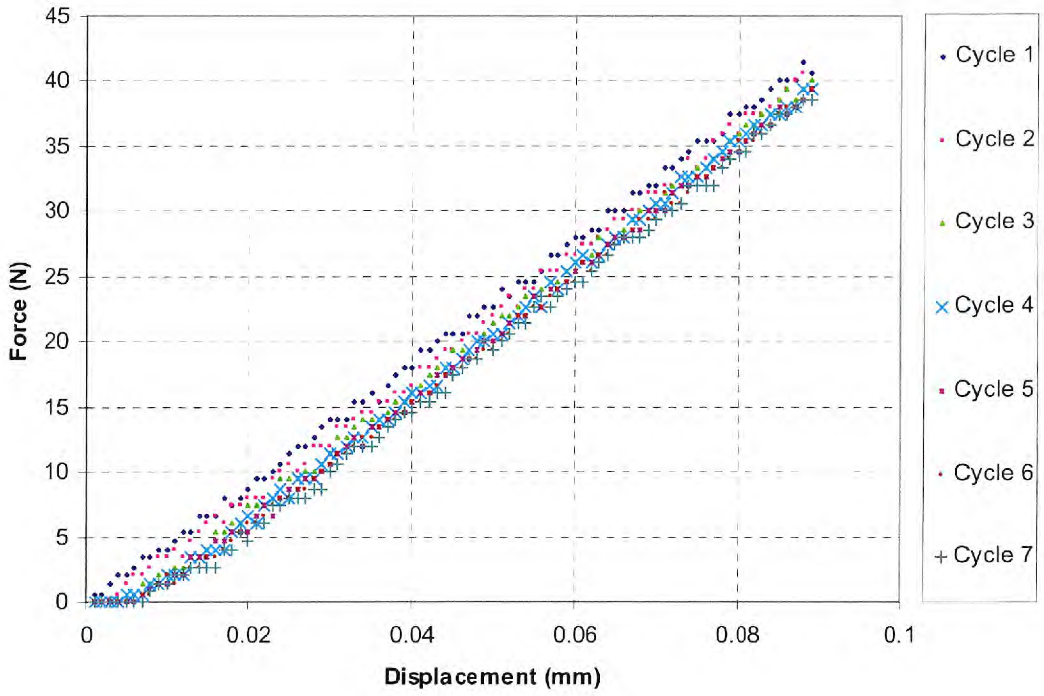

Figure 4.28: Repetitive cycling over the linear elastic region of a force-displacement curve in four-point bending using the same test settings and bar sample. Seven cycles were completed.

The graph shows that, whilst the curve becomes progressively displaced along the x-axis, it is consistently linear and has the same gradient. Elastic modulus calculation uses differences in force per unit displacement (gradient) not absolute values. The reproduced linear slope and gradient demonstrates the sample is repetitively elastic over the region tested. Data for elastic modulus calculation can be taken from the second force-displacement run, after everything has 'settled down', and will be representative for that sample.

To decide the displacement limit during testing one bar for each of the eight ECC samples was tested to fracture. Plastic deformation occurred after 0.125mm displacement for all eight samples. A maximum displacement of 0.09mm was set for all tests .

Four-point bend test elastic modulus results, taking the average of ten bar samples for each of the eight ECC sample sets, are shown in Table 4.7 and Figure 4.29. One standard deviation was used as the error limits. Elastic modulus versus ECC pressure is shown in Figure 4.30.

Table 4.7: Table showing the mean and standard deviation of elastic modulus measurements for eight samples extruded at different ECC pressures.

Sample	ECC Pressure (mbar)	Elastic Modulus (GPa)	
		Mean	Std Dev
ECC1	200	0.097	0.015
ECC2	775	0.101	0.015
ECC3	1450	0.147	0.034
ECC4	1950	0.408	0.068
ECC5	2300	0.318	0.036
ECC6	200	0.098	0.012
ECC7	1450	0.258	0.030
ECC8	2300	0.382	0.031

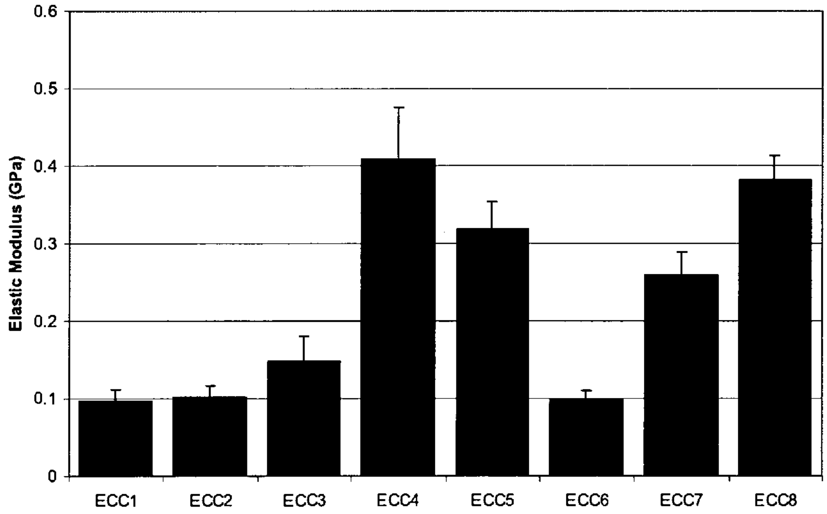

Figure 4.29: Column chart showing the mean elastic modulus for eight sample sets extruded at different ECC pressures. One standard deviation is used as the error limit.

The range in elastic modulus, E, was 0.097GPa to 0.408GPa. Significant differences were seen between data sets. Error margins appear smaller than those seen for the texture mechanical tests. This is likely due to the uniform geometric properties of bar samples compared with extruded discs direct from production (as used in texture mechanical tests). Furthermore, elastic modulus is a clearly defined and meaningful mechanical material property.

The accuracy of the measurements was checked using a material, aluminium, of similar dimensions and known elastic modulus. The test gave an elastic modulus of 65GPa, after accounting for rig deflection, versus 68GPa from the literature. This proves four-point bend tests produce suitably accurate results.

Viewing Figure 4.30 shows the definite trend between elastic modulus and ECC pressure. Elastic modulus increases as ECC pressure increases. This implies, considering knowledge of the ECC's effect on porosity, a relationship between elastic modulus and volume fraction porosity/average pore wall thickness. Discussion of this will be presented in later sections.

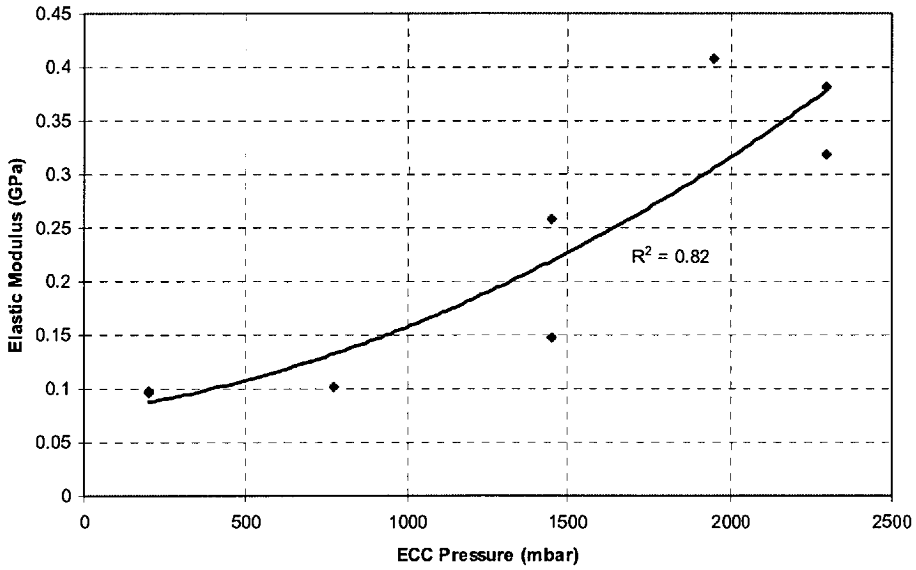

Figure 4.30: A graph showing the relationship between elastic modulus of the sample and ECC pressure. A second order polynomial fit is shown.

5. PORE STRUCURE, MECHANICAL PROPERTIES and ACOUSTIC EMISSIONS

Sensory texture will be judged via a combination of acoustic and mechanical properties. Pore structure is the likely product attribute that links mechanical and acoustic properties, or further still drives sensory texture itself. Previous studies considering the effect of pore structure on mechanical properties have not been able to isolate pore structure alone and mechanical differences were obtained as a function of a particular extruder variable such as moisture (Hayter and Smith 1988). Similar methods were seen for most reviewed food acoustic emission studies. Changing extrusion conditions to alter pore structures will impact skeletal material itself. However, considering pore structure alone is now possible through the use of the Expansion Control Chamber in the production phase which maintains constant skeletal material properties.

Here, Chapter 5, eight samples produced using different ECC pressures are used to investigate relationships between mechanical properties, mechanical destruction acoustic emissions and pore structure. Results as presented in the previous chapter (Results) are used to initially consider the effect of pore structure on mechanical properties followed by a discussion of how acoustic emissions are related to both mechanical properties and pore structure. Further detail of the effect of pore structure on acoustic emissions will be continued in Chapter 6 (Vibration and Acoustic).

5.1. Pore Structure and Mechanical Properties

Most food-based studies of mechanical properties have related them as a function of recipe or process. However, it is common for foamed polymers to consider mechanical properties from a density and pore-structure stand-point. This approach has been adopted by some authors in the study of extrudate mechanical properties showing mechanical properties increase with bulk density in a similar manner to foamed plastics (Hayter and Smith 1988).

Barrett et al. (Barrett, Cardello et al. 1994) looked at extruded snacks. They showed neither density, nor mean cell area alone could be used as an indicator of mechanical strength. Young's modulus has been associated with pore size, pore density (Van Hecke, Allaf et al. 1995; Gao and Tan 1996) and pore wall thickness (Hayter and Smith 1988; Van Hecke, Allaf et al. 1995; Gao and Tan 1996; Agbisit, Alavi et al. 2007).

More recently, greater accuracy and objectivity in microstructural measurements have led to the possibility of applying theoretical models to understand the mechanics of solid food foams (Agbisit, Alavi et al. 2007), the ultimate aim being product design to achieve specific mechanical properties and sensory texture. The Gibson-Ashby model for the mechanical properties of brittle foams uses cubic cell geometry (Gibson and Ashby 1997). It has been used with some success obtaining an R^2 of 0.72 to the model for elastic modulus for extrudates (Agbisit, Alavi et al. 2007). The Gibson-Ashby model uses cellular parameters such as edge length, wall thickness and relative density (ρ_b/ρ_s) with relative density being the most important 'macro' characteristic. A term is also included in the model for the contribution of compressed air inside cells but is relatively small compared with other terms.

In the work done by Agbisit et al. pore wall thickness remained relatively constant for different samples. For this reason the effect of pore wall thickness on mechanical properties could not be investigated, only predicted from the model. An important criterion for the applicability of the Gibson-Ashby model is $\rho_b/\rho_s<0.2$. In the present study ρ_b/ρ_s ranged from 0.4 to 0.7 with samples produced having different ECC pressures. For this reason it is not possible to apply the model to results for these products. Furthermore the Gibson-Ashby model suggests pore walls are beams whereas XMT images suggest extrudate structures in this study are a combination of strut-like beams and membranes.

In this chapter the mechanical properties of maximum stress, crispness 1 and elastic modulus will be discussed separately in relation to identified pore parameters; volume fraction porosity, mean pore size and average pore wall thickness. Please note, due to the definition of volume fraction porosity (see equation 3.2), bulk density would provide no additional information since skeletal density is constant for all sample sets.

5.1.1. Maximum stress

Logical thought hypothesises that mechanical strength of an extrudate is a function of three factors, the amount of skeletal material, the distribution of that skeletal material and the strength of that skeletal material. Skeletal material properties (e.g. strength) are constant for all ECC sample sets. The distribution of skeletal material is highly complex and would include aspects of pore geometry, pore orientation, etc. However, these factors will probably have less significance than the amount and strength of skeletal material in real terms. Also, looking at the XMT images in Figure 4.18 and Figure 4.19 demonstrates how complex these terms would be for different ECC samples. For these reasons it will not be included in further discussion and thought comparatively negligible. It now follows that sample mechanical strength (maximum stress) is a function of the amount of skeletal material for ECC samples. On a fundamental level:

- Decreased volume fraction porosity increases the amount of skeletal material, hence increases maximum stress.
- Increased average pore wall thickness increases the amount of skeletal material, hence increases maximum stress.

The highest maximum stress would be expected for a sample with low volume fraction porosity and thick pore walls.

Figure 5.1 shows a scatter plot for maximum stress versus volume fraction porosity. Volume fraction porosity is a measure of sample expansion. A clear trend is seen between volume fraction porosity (hence expansion) and maximum stress, having an r-squared of 0.60. This is as predicted with decreasing volume fraction producing increased maximum stress, i.e. more solid material per unit volume gives a stronger sample.

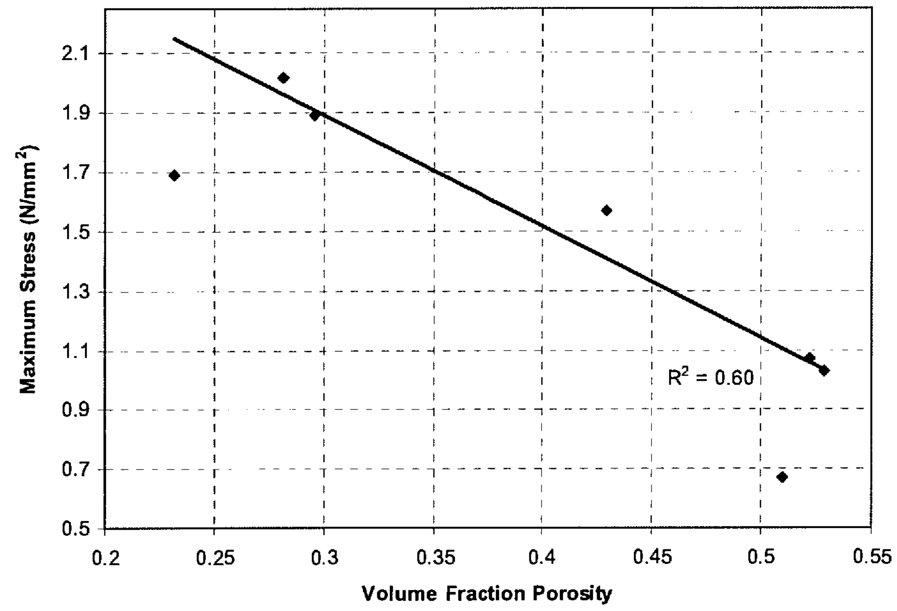

Figure 5.1: A graph showing how volume fraction porosity affects maximum stress for eight samples extruded at different ECC pressures. A linear fit it shown.

Figure 5.2 shows maximum stress has little to no dependence on mean pore diameter (and so assumed pore size) for these ECC samples. However, Figure 5.3 shows maximum stress increases as average pore wall thickness increases. This follows the predictions outlined previously. During fracture it is these walls that must fail. Thicker walls will require a greater force to fracture than thinner walls following that more skeletal material provides greater strength.

Considering volume fraction porosity and average pore wall thickness it has been shown that extrudate maximum stress is dependent upon the amount of skeletal material in the sample; hence inversely to the total amount of air/porosity in the sample. However, as mean pore diameter showed no clear effect it can be implied that the distribution of porosity through the sample does not have as strong an influence as the amount of skeletal material. This supports the discussion at the beginning of this section.

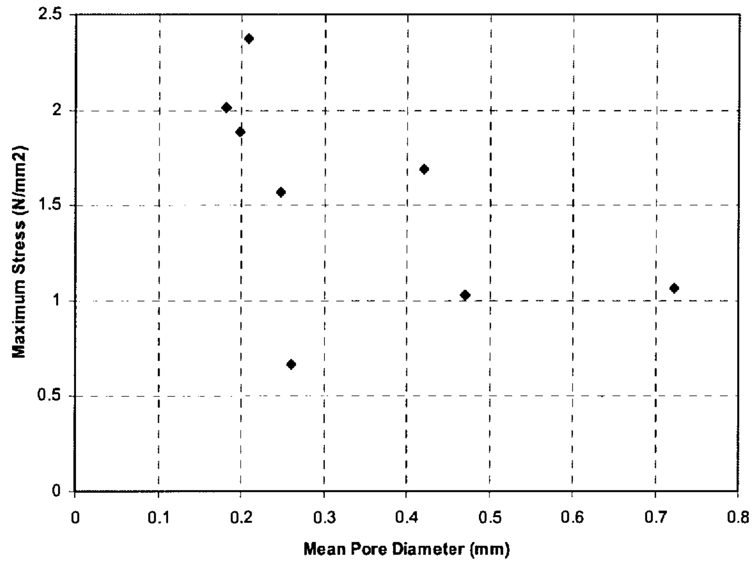

Figure 5.2: A scatter plot of maximum stress versus mean pore diameter for eight samples extruded at different ECC pressures.

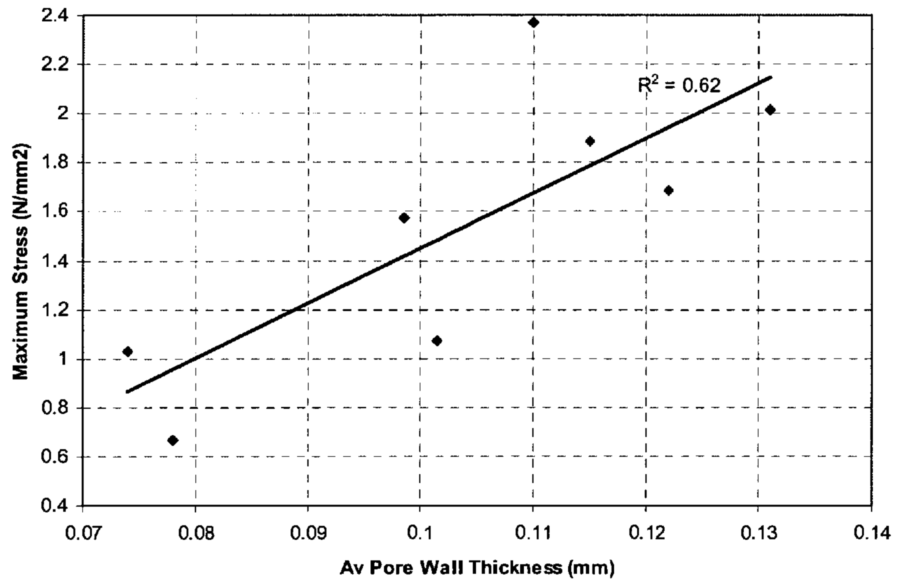

Figure 5.3: A graph showing how average pore wall thickness affects maximum stress for eight samples extruded at different ECC pressures. A linear fit is shown.

With maximum stress being related to both volume fraction porosity and average pore wall thickness, it should follow that they themselves are related when the ECC is used in the production phase. Figure 5.4 shows them to be well correlated with each other, showing good agreement with section 4.2.2 where both volume fraction porosity and average pore wall thickness were dependent on ECC pressure. This shows pore wall thickness to be the dominant factor influencing volume fraction, not pore size when using the ECC. It is still unclear whether it is the amount of skeletal material (volume fraction porosity) or the thickness of the pore walls that drive material strength and maximum stress, since the two are inter-related. To truly consider this, pore wall thickness would have to be varied with constant volume fraction porosity and vice-versa. It is unlikely this will be possible with the extrusion process.

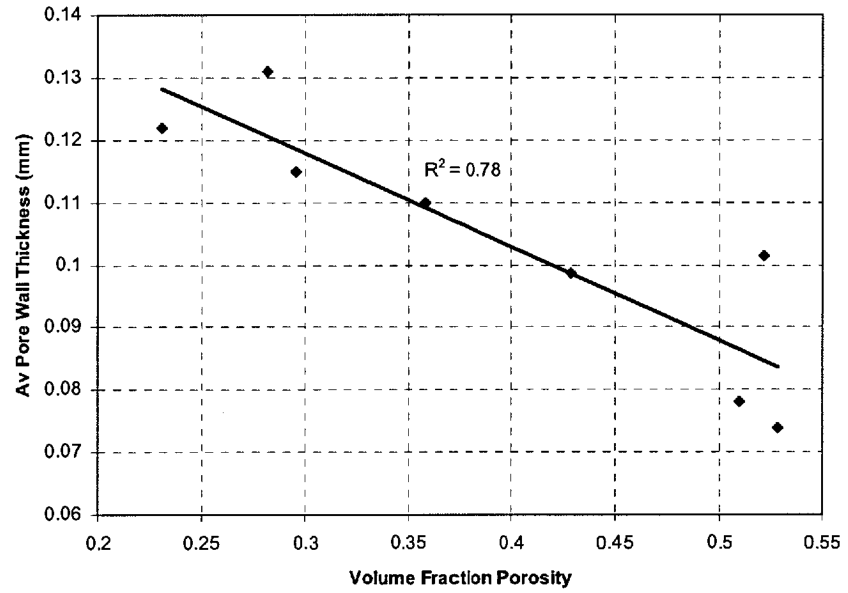

Figure 5.4: A graph showing the relationship between volume fraction porosity and average pore wall thickness for eight samples extruded at different ECC pressures. A linear fit is shown.

Figure 5.5 shows how maximum stress is related to ECC pressure. Knowing the relationships just discussed this is as expected showing maximum stress increases with ECC pressure. Under normal extrusion conditions, with the die exit at atmospheric pressure, it can be assumed that maximum stress would still be a function of volume fraction porosity, and in turn average pore wall thickness, however additional influence may come from changes in skeletal density – i.e. the different extrusion conditions used to vary volume fraction would in turn also affect extrudate skeletal material.

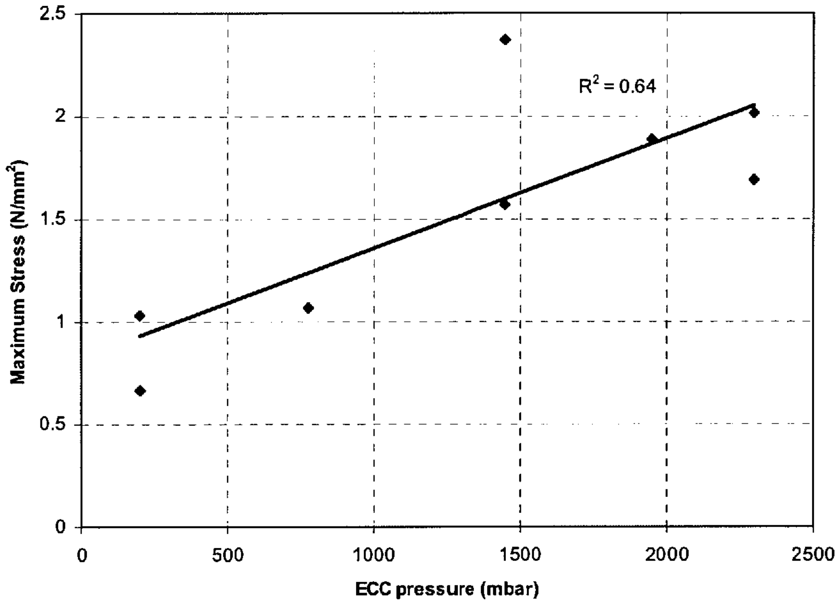

Figure 5.5: A graph showing the relationship between ECC pressure and maximum stress using eight samples extruded at different ECC pressures. A linear fit is shown.

5.1.2. Crispness

Previous work, internal to Mars Inc., has hypothesised crispness is related to the number of pores along the axis of compression during mechanical testing. The definition of crispness 1 is the number of peaks in a force-displacement curve created during a mechanical test. It was hypothesised that each registered peak relates to the fracture of the wall of one pore sequentially through the sample. If the hypothesis were true it would follow that there is a pore size threshold under which that pore is considered part of another pore's wall – i.e. its wall does not fracture alone so has no impact on crispness 1.

Figure 5.6 shows crispness 1 increased, to some extent, as volume fraction porosity increased. It follows that more pores would increase volume fraction porosity increasing crispness. There was no dependence of crispness 1 on mean pore diameter as shown by Figure 5.7. A smaller mean pore size might be expected to give more pores, and hence pore walls in the fracture path. However, mean pore size has to be considered in conjunction with volume fraction porosity (to which crispness 1 shows some dependence) and for the eight ECC samples pore sizes appear random whilst volume fraction porosity is controlled (refer section 4.2.2). Furthermore, mean pore size may be unduly influenced by pores below the theoretical pore size threshold which should be included as pore wall, and not in the mean pore size for this situation.

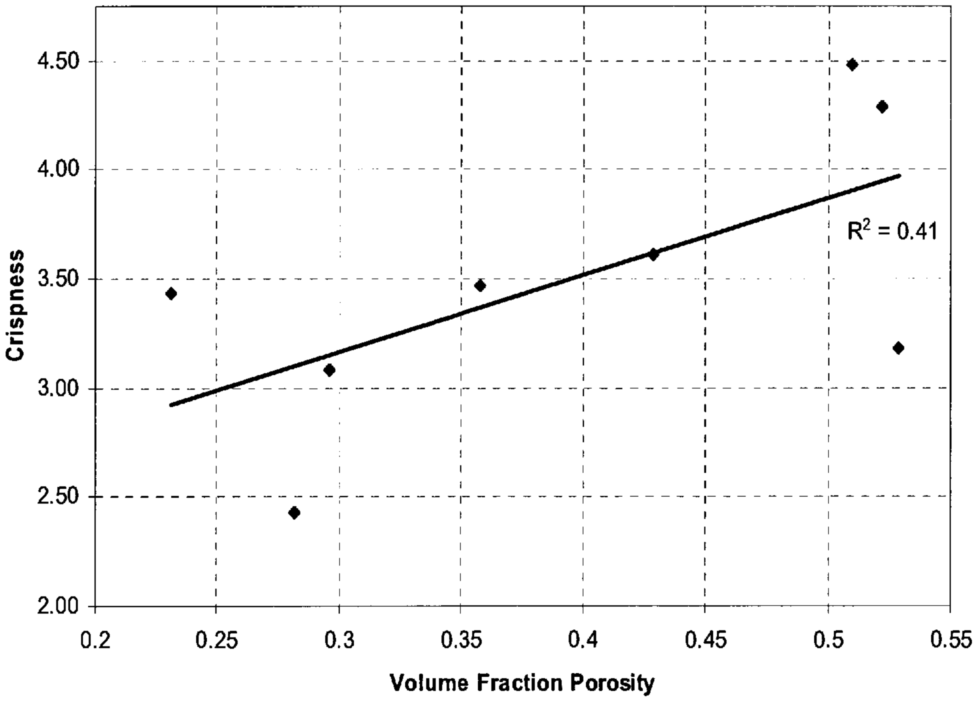

Figure 5.6: Relationship between crispness 1 and volume fraction porosity for eight samples extruded at different ECC pressures. A linear fit is shown.

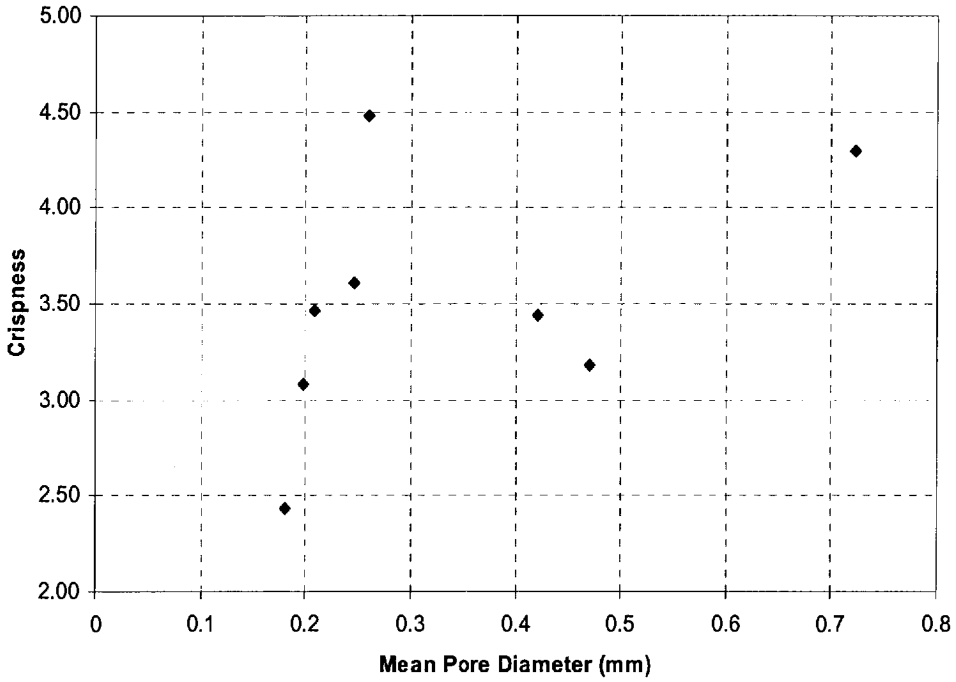

Figure 5.7: A scatter plot of crispness versus mean pore diameter for eight samples extruded at different ECC pressures.

Figure 5.8, crispness 1 versus average pore wall thickness, shows there is a low level tendency for samples with smaller average pore wall thicknesses to have higher crispness 1 values. This follows from results of crispness 1 versus volume fraction porosity as it is not possible to disassociate the two (refer Figure 5.4). So this work has shown that more porosity results in higher crispness 1 and, whilst not proved here, it has been hypothesised this is due to a greater number of pore walls fracturing.

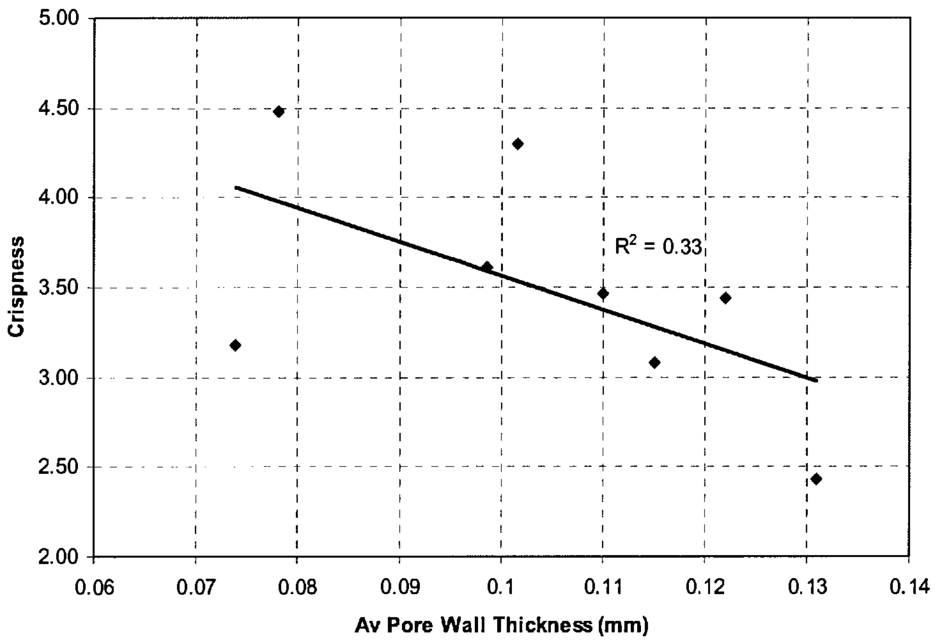

Figure 5.8: Relationship between crispness and average pore wall thickness for eight samples extruded at different ECC pressures. A linear fit is shown.

5.1.3. Elastic Modulus

Elastic modulus should increase as volume fraction porosity decreases towards zero, hence tends towards solid material as seen for other materials (Rice 1998; Pabst, Gregorova et al. 2006). Studies relating elastic modulus to porosity for other materials have done so with varying degrees of complexity (Rice 1998; Pabst, Gregorova et al. 2006). Figure 5.9 shows how elastic modulus depends on volume fraction porosity for the present data set. Results are as expected with elastic modulus decreasing as volume fraction porosity increases. Both linear and exponential fits represent the data well. However, it is likely that the true relationship between volume fraction porosity and elastic modulus is more complex. Factors such as pore geometry etc. may have a significant impact for the same reasons as discussed with maximum stress (section 5.1.1). Detailed investigation of this relationship could form part of future work.

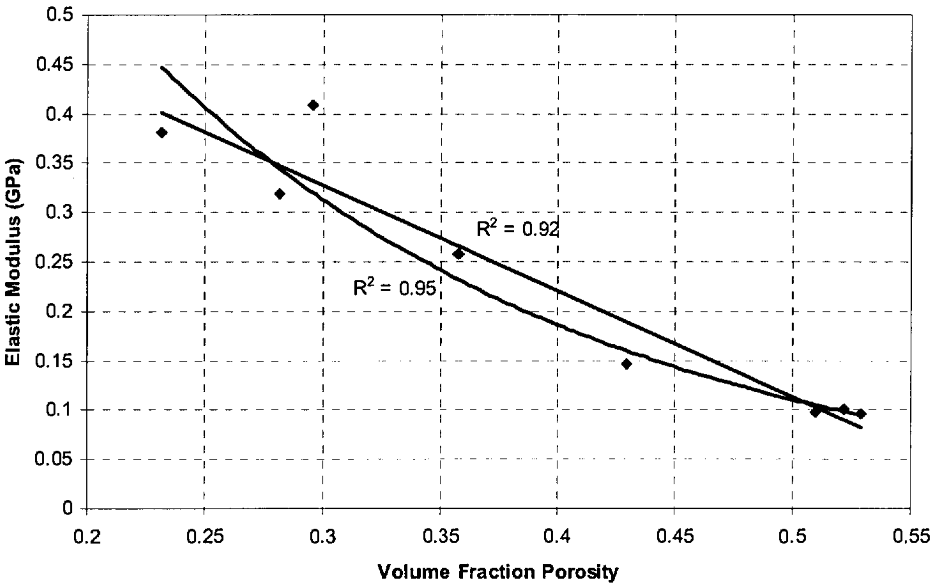

Figure 5.9: A graph detailing the dependence of elastic modulus of volume fraction porosity for eight samples extruded at different ECC pressures. Linear and exponential fits are shown.

For the ECC samples the minimum volume fraction porosity was 0.23 whilst the highest was 0.53. In this range the linear and exponential fits have r-squared values of 0.92 and 0.96 respectively. Please note there are insufficient data to build the complex relationship discussed in the previous paragraph. For this study it is important to obtain a prediction of elastic modulus at zero porosity (i.e. skeletal material) for the modelling of pore wall vibrations in the next chapter. The simple models discussed here were deemed appropriate for this purpose.

The equation when using the linear fit is;

$$y = -1.0662x + 0.6468 \qquad [5.1]$$

meaning zero porosity, or pore wall/skeletal material, elastic modulus is approximated as 0.65GPa. For the exponential fit the equation is;

$$y = 1.4852e^{-5.193x} \qquad [5.2]$$

predicting a skeletal material elastic modulus of 1.5GPa. With the exponential term having been seen for other materials (Rice 1998), the exponential fit was probably the more accurate.

Figure 5.10 shows the effect of average pore wall thickness on elastic modulus. As with maximum stress, the opposite of the relationship to volume fraction porosity was observed. That is, greater pore wall thickness produces a higher elastic modulus. However, the correlation is not as strong. A similar relationship was seen between ECC pressure and elastic modulus. This means the ECC is capable of controlling both maximum stress and elastic modulus. Figure 5.11 shows maximum stress and elastic modulus are reasonably well correlated as would be expected from these results. No correlation is apparent between mean pore diameter and elastic modulus (graph not shown).

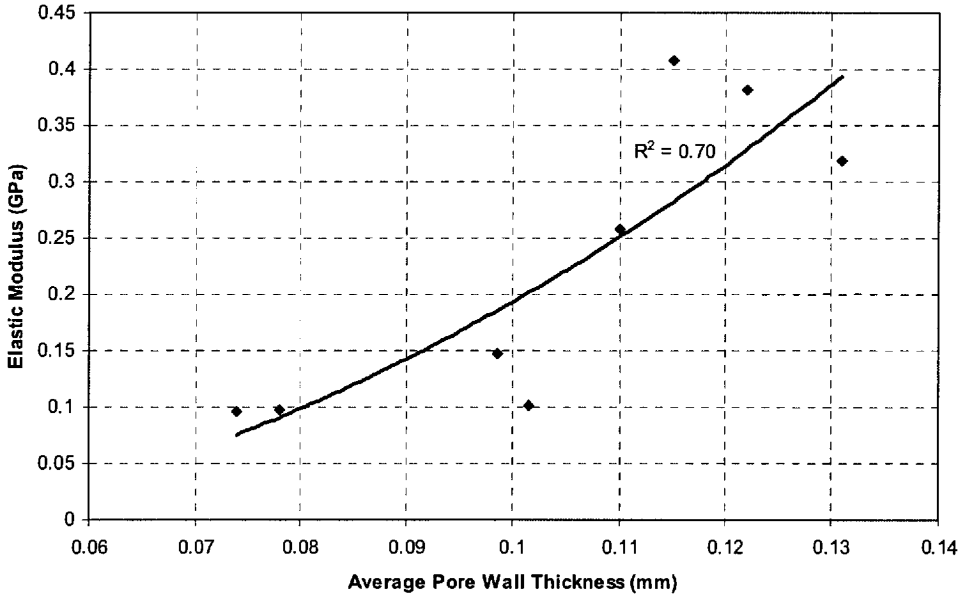

Figure 5.10: A scatter plot showing the effect average pore wall thickness has on elastic modulus for eight samples extruded at different ECC pressure.

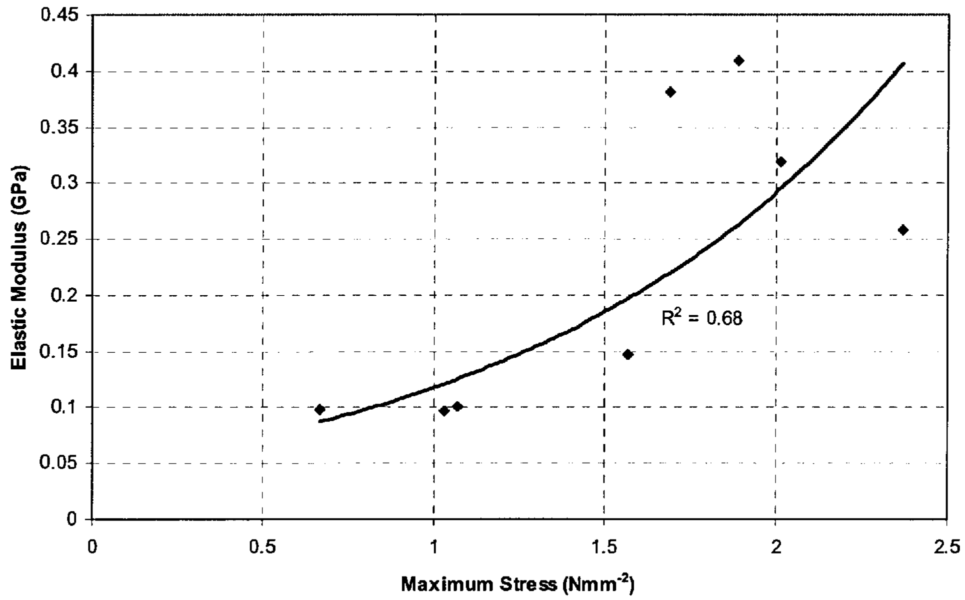

Figure 5.11: A graph showing the relationship between maximum stress and elastic modulus for eight samples extruded at different ECC pressures.

5.1.4. Summary discussion

It is clear that pore structure has a large influence on sample mechanical properties. Volume fraction porosity is the main structural parameter determining elastic modulus, whilst it is unclear whether maximum stress is determined by a combination of both volume fraction porosity and average pore wall thickness or either parameter individually. However, due to the relationship between average pore wall thickness and volume fraction porosity it is difficult to separate the two effects (ideally one would remain constant whilst the other varies, however this is not likely with extrudates). Logical thought may actually imply it is pore wall thickness determining mechanical strength, as this is the critical dimension of what is fracturing; however, volume fraction porosity can be equally well justified. Both relate to the total amount of solid material which may be the ultimate driver. It is clear that both maximum stress and elastic modulus decrease with increased expansion indicating a general weakening of the extrudate structure.

With volume fraction porosity being one minus volume fraction solid it may be that volume fraction porosity is the main driver and average pore wall thickness would only be included if a more complex relationship was built such as that seen for the Gibson-Ashby model were relative density is considered the most important term, but beam length and thickness terms are incorporated; increasing thickness and decreasing length of beams leads to higher stiffness and failure strength. Volume fraction porosity was a much stronger indicator for elastic modulus. The ECC can be used to control the mechanical properties of maximum stress and extrudate elastic modulus. Estimates were made of skeletal material elastic modulus for use in the next chapter.

Crispness 1 was least related to those pore parameters measured. A low level dependence on both volume fraction and average pore wall thickness was seen. It has been hypothesised that crispness is related more to the number of (fractured) pore walls through the axis of compression, or more likely the number of collective fractures if more than one cell fractures at the same time. The number of pores will, as discussed, be expected to be somewhat related to volume fraction porosity and average pore wall thickness.

All results fit well with those seen for extrudates in the past and the general relationships predicted from the Gibson-Ashby model. The not previously tested parameter of pore wall thickness was shown to have an impact on mechanical properties fitting predictions. However, pore wall thickness could not be decoupled from volume fraction porosity.

5.2. Acoustic emissions related to mechanical properties and pore structure

Obtaining numerical values that reliably describe differences in acoustic frequency spectra from different extrudate samples is difficult. However, clearly 'describable' differences have been observed. For this reason it is difficult to build quantitative relationships between acoustic frequency spectra and mechanical measures and pore properties. This section will discuss relationships and trends in general qualitative terms unless considering RDC, the only numerical acoustic parameter where quantitative differences were seen. Please note differences discussed for one sample set's average spectrum are seen for all repeats in that set.

Figure 4.21 (page 103), showing average frequency spectra for eight different ECC samples, revealed that there are clear differences between samples. Peaks positions and differences in peak intensities will now be described for each sample. Descriptions will begin with samples extruded at the lowest ECC pressure (most porous) and finish with those extruded at the highest (least porous). Qualitative descriptions regarding peak intensity are relative to other ECC sample peaks (i.e. mid, low, high).

Both samples extruded using 200mbar ECC pressure have very weak peaks for all frequencies bar those below 2000Hz (refer Figure 4.21 and Figure 4.22). The (one) sample extruded using an ECC pressure of 775 mbar also has weak peaks but does have a range of peaks close to 6900Hz not seen for any other sample. The two 1450mbar ECC pressure samples show different frequency spectra to each other. Other than those frequency peaks below 2000Hz one 1450mbar sample gave few peaks. However, this sample showed a range of small peaks between 4000Hz and 6000Hz not seen for other samples. The second 1450mbar sample has four distinct medium intensity peaks above 2000Hz at 3500Hz, 4000Hz, 8500Hz and 9000Hz. The same peaks are present in the spectra of the remaining (three) samples but with differing intensities. The sample extruded using 1950mbar ECC pressure has medium to low intensity peaks for all bar the 3500Hz peak which is strong and double. The two samples extruded at 2300mbar ECC pressure show the same as the 1950mbar sample except the 3500Hz peak is single and relatively very strong for both.

From this discussion a major point of note is that most samples have the same peak positions (frequency) but differing intensities. High frequency (above 8000Hz) peaks are, to some extent, present in all samples. Frequency peaks at 3500Hz and 4000Hz are increasingly present as ECC pressure increases (thus reducing volume fraction porosity and increasing average pore wall thickness). Differences have been observed in this frequency area with previous work [please note, this work used the same extrusion recipe] (refer Figure 2.5). Viewing Figure 4.22 of the average frequency spectra for each sample set plotted using a log-scale for the frequency x-axis there are few discernable differences in low frequencies below 1200Hz. However, there are two peaks in the 1200-1850Hz range of each sample which it could be argued reduce as ECC pressure increases.

Following this discussion two specific frequency regions on which to focus were defined, those being the frequency ranges of 1200-2000Hz (Range 1) and 3000-4300Hz (Range 2), representing the areas in which peak intensity varied for different samples. Peak position was deemed not important due to the similarities seen for all samples; major differences generally came with peak intensity. Figure 2.5 details frequency spectra for samples produced with the same recipe as those in Figure 4.21. Differences seen are in a similar frequency position near 4000Hz. Figure 3.24 shows samples with different recipes have different peak positions. This implies peak position is heavily determined by recipe. Figure 5.12 and 5.14 show the two defined frequency ranges in more detail.

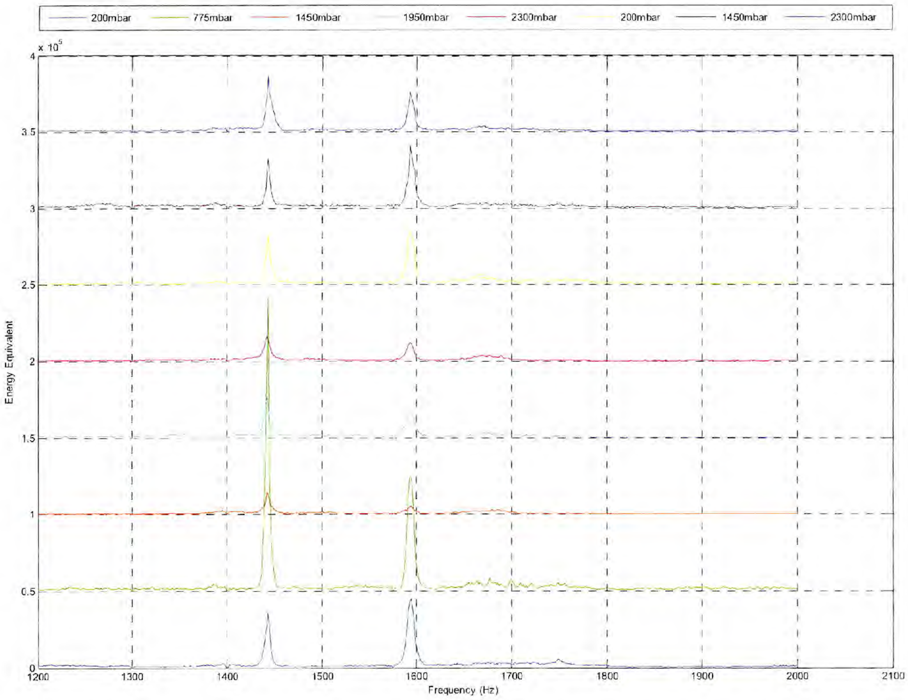

Figure 5.12: Magnified view of different ECC sample average frequency spectra for the frequency range of 1200-2000Hz (Range 1).

Figure 5.12 provided no identifiable trend to ECC pressure, the initial premise having been that the height of the frequency peaks reduced as ECC pressure increased, reducing volume fraction porosity and increasing pore wall thickness. The total energy of the acoustic signal within this frequency range was calculated using the trapezoidal method of integration to obtain the area under the curve. This provides a unit-less energy equivalent having the same order of magnitude as would be seen for calibrated data.

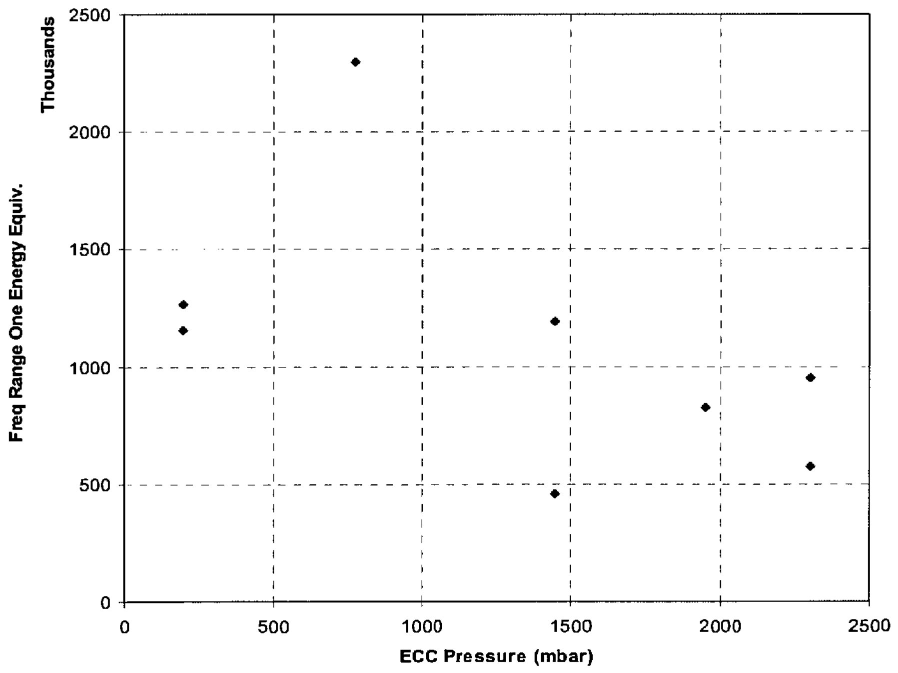

Figure 5.13: Total energy equivalent held in the frequency range 1200-2000Hz (Range 1) for the signal of samples produced with different ECC pressures.

Figure 5.13 could indicate a weak trend for decreasing energy as ECC pressure increases. Clarification of this trend will require additional extrusion work and could be conducted as part of future work. However, the existence of such a trend will be considered through this work.

Figure 5.14 shows frequency spectra for different ECC samples in the range of 3000-4300Hz. Peak intensity noticeably increases as ECC pressure increases, with volume fraction porosity decreasing and average pore wall thickness increasing.

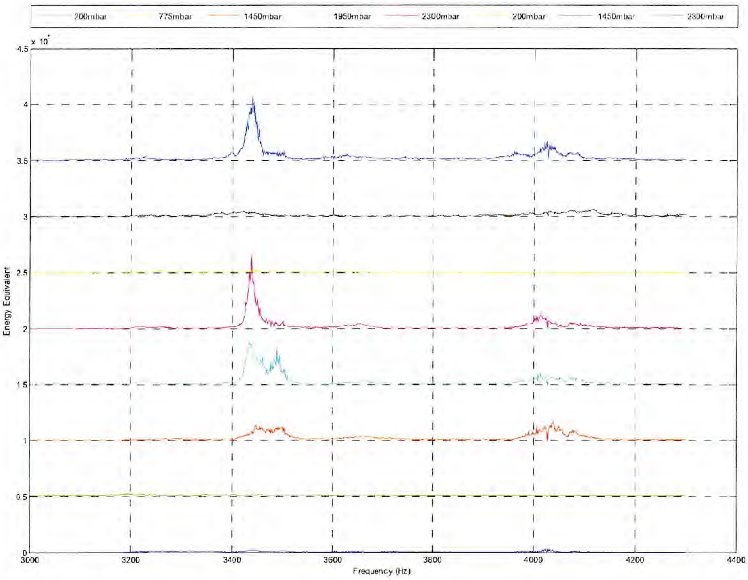

Figure 5.14: Magnified view of different ECC sample average frequency spectra for the frequency range of 3000-4300Hz (Range 2).

Figure 5.15 details the relationship between signal energy in this frequency range for different ECC pressures. Signal energy increased with ECC pressure. These results are as expected from the entire frequency spectra. Referring back to section 3.2.2.5 (Experimental equipment) frequency areas in which peaks may come from the test rig were <1000Hz and 4420-4440Hz, neither of which fall into the ranges of focussed analysis.

Such similar frequency peak positions imply natural vibration of similar size and geometry objects, in the same mode and node, for all samples but in differing amounts. If we assume natural vibration is that of pore walls it would follow that there are, in all sample sets, common sizes and geometries of pore wall created during production with the ECC, and different ECC pressures vary the number (and hence frequency peak intensity) of pore walls at these geometries; that is, the pore wall size/shape and anchoring effects frequency position whilst the number of similar geometry vibratory components produces the energy intensity at that frequency spectrum. This will only hold true when skeletal material remains constant as was the case for these samples.

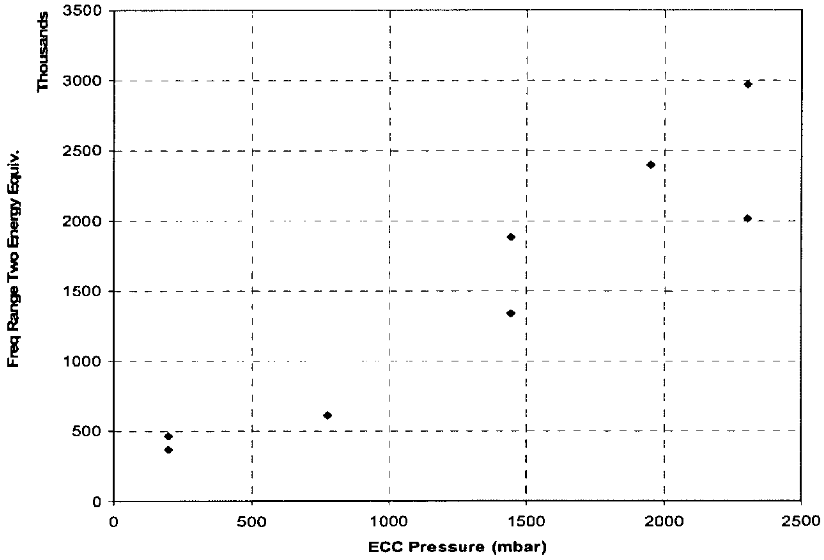

Figure 5.15: Total energy equivalent held in the frequency range 3000-4300Hz (Range 2) for the signal of samples produced with different ECC pressures.

Specifics concerning the vibrations of pore walls and origins of frequency peaks will be expanded in the following chapter. But assuming pore walls are the vibratory component at present we can say as pore wall thickness increases and volume fraction porosity decreases, the number of 3000-4300Hz vibratory components increase and the 1200-2000Hz vibratory components (possibly) decrease.

Referring back to the entire frequency spectra (Figure 4.21) the 200mbar ECC pressure sample has fewer, or at least very low intensity, frequency peaks through the entire frequency range. This could be due to a lack of pore walls to vibrate. The 200mbar sample was the most expanded having less solid and pore wall material per unit volume making this is a plausible explanation.

It is not clear where peaks below 1200Hz originate. They may originate from vibrations of pore walls, some other vibration originating from the extrudate sample, or the test rig and system itself. However, there is little variation in peak position and intensity below 1200Hz so these vibratory components remain constant for all samples. Peaks below 1200Hz will not be discussed any further. Additionally, work by Chen et al. (Chen, Karlsson et al. 2005) has suggested noise below 1000Hz is background and machine noise.

Earlier in this chapter, the major finding between pore structure and mechanical properties was that, as average pore wall thickness increases and volume fraction decreases maximum stress and elastic modulus increase. Therefore it follows that the higher the maximum stress and elastic modulus (of the sample) the stronger frequency peaks between 3500Hz and 4000Hz will be, whilst those between 1200Hz and 2000Hz may become weaker. The reverse correlation was observed for crispness 1, but not as strongly – that is, samples with higher crispness values have less 3500-4000Hz sounds but more lower frequency 1200-2000Hz sounds.

Figure 5.12 and 5.14 have also shown signal energy may play an important role, however, areas of interest must be focussed on. Considering Figure 4.21 this is likely because the similar peaks (to all samples) below 1000Hz contribute most energy. This fits with visual interpretation where we might have expected the 200mbar samples (original and replicate), 775mbar sample and one of the 1450mbar samples (original) to have lower acoustic signal energy. Here it can be noted that, whilst ECC pressure replicates did not have the same absolute value, they did fit with observed trends.

Table 4.5 showed differences in RDC at different ECC pressures, but no dependence on ECC pressure or pore parameters. RDC did, however, increase with crispness 1 as seen in Figure 5.16. Mechanically measured crispness 1 had been hypothesised as relating to sensory crispness (McGrane 2004). Whilst RDC can only be used to approximate mechanically measured crispness 1, it may be suitable for describing sensory crispness better than the mechanical measure. Work incorporating sensory panels could be conducted to test this hypothesis.

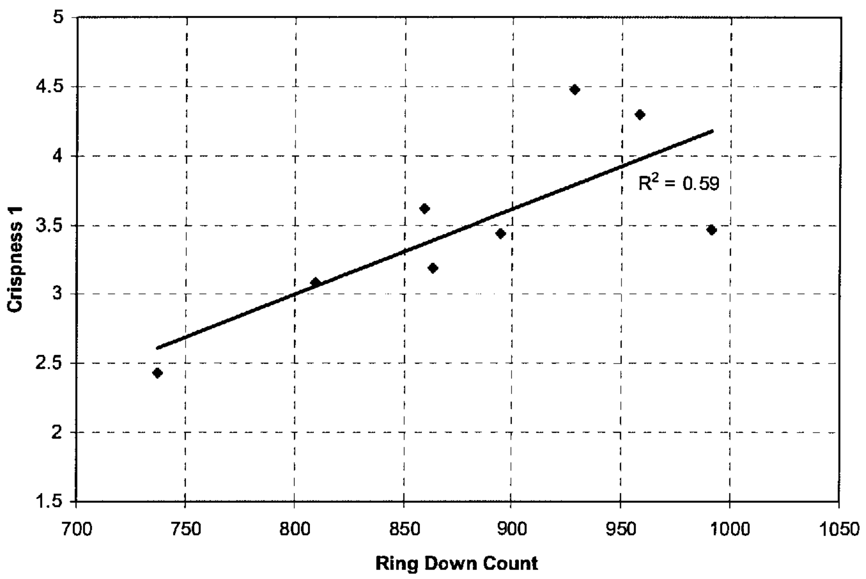

Figure 5.16: The relationship between ring down count from a mechanical destruction acoustic signal and mechanically measured crispness for eight samples extruded at different ECC pressures. A linear fit is shown.

To summarise with regards to acoustic emissions, it is difficult to correlate mechanically measured (or otherwise) textural parameters with acoustic measures. But the acoustic frequency spectra can be used to compare different products on a qualitative basis. The acoustic emissions themselves appear to be influenced by volume fraction porosity and average pore wall thickness as are mechanical properties. Volume fraction porosity is believed to be the primary driver for mechanical properties whereas, a distinction cannot yet be made regarding acoustic emissions. RDC has shown promise as a possible quantitative indicator of sensory crispness.

To understand acoustic emissions from a product design perspective the primary acoustic driver within the pore structure and what is vibrating must be discovered. This chapter has proven pore structure affects acoustic emission frequency spectra. One hypothesis is that the pore walls are the vibratory component creating the acoustic emission. The next chapter explores this in order to try and identify the source of the differences in acoustic emission.

6. VIBRATION AND ACOUSTIC EMISSIONS

6.1. Background

Throughout this project porosity has been indicated, and now proven, as the controlling bulk parameter behind mechanical destruction and acoustic frequency spectra differences for samples with the same skeletal material. However, it is unclear exactly how porosity differences affect frequency spectra, although volume fraction porosity and average pore wall thickness have an impact. It is important to understand this so the acoustic emissions can be controlled through the extrusion process for product improvement and new product development.

Acoustic emissions result from objects vibrating and passing these vibrations to the air as alternate regions of compression and rarefraction. The frequency of the vibrating object will be the frequency of the acoustic vibration. During the mechanical destruction of an extrudate, fractured pore walls probably snap back into position vibrating. The fracture pieces themselves may also vibrate as well as intact structural elements. Knowledge of what is vibrating will be advantageous for production purposes as the acoustic emission frequency spectra can be controlled through manipulation of that product parameter during extrusion.

Pore wall vibrations can be considered by approximate modelling of those vibrations at fracture. Precise modelling of pore wall vibrations would be difficult due to the complex sample porosity (as seen through this thesis). Exact shape, edge conditions, etc. of the vibrating pore wall will be affected by both the porosity and position of fracture which will in turn affect vibration frequency. However, modelling pore walls as the vibration of simplified basic shapes will give a suitable approximation of vibration frequencies to see if they are close to those frequencies seen during mechanical destruction. These models will account for approximate geometries, edge conditions and skeletal material properties. If modelled vibration frequencies fall into the range in which peaks are seen in the frequency spectra it can be that pore wall vibrations are probably responsible for the recorded acoustic emissions.

6.2. Possible Structures

When deciding how to model pore wall vibrations thought was first given to extrudate structure. Porous structures can be considered in two ways depending on the level of porosity in the sample. A highly porous structure (high volume fraction porosity) will likely have pore walls approximating a complex network of struts as described in the Gibson-Ashby mechanical model (Gibson and Ashby 1997). Lower volume fraction porosity will likely result in a more membrane type pore wall (as in a closed-cell foam). Figure 6.1 shows a 1.44mm^3 internal structure of a starch extrudate obtained from XMT. Viewing this helps see how both struts and membranes could be considered reasonable approximations with the reality likely some combination of the two; this was one limiting issue of using the Gibson-Ashby method to model mechanical properties. Figure 6.1 also shows how complex the true edge conditions are, compared with those in the model to be discussed in section 6.3 (Possible Vibrations).

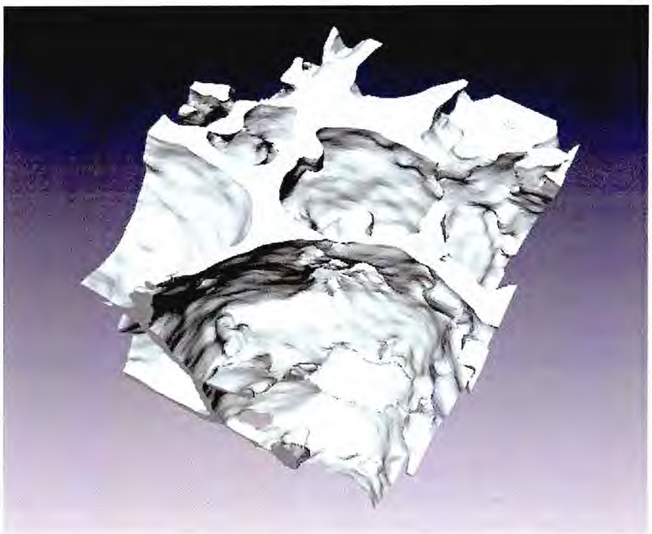

Figure 6.1: Internal structure showing the pore walls of a starch extrudate. This is a 1.44mm^3 section from the centre of a sample.

6.3. Possible Vibrations

Following the discussion of possible structures the basic geometric shapes upon which pore wall vibrations should be modelled were beams (struts) or plates (membranes), both being approximations. Different edge conditions for these shapes will result in different vibration modes. The constraints of the model, discussed in 6.2 (Possible Structures), mean that estimated natural frequencies can only be seen as ball-park approximations. However, this is suitable for our purposes. It must also be remembered that it is not necessarily fractured components that vibrate to create the acoustic emission; all intact structural elements will also vibrate contributing to the acoustic signal.

When modelling pore wall vibrations, changes in skeletal material properties through the sample volume will have an effect. Whilst material properties are unlikely to be 100% homogeneous through the skeletal material volume, for the purpose of this work they will be close enough. Therefore uniformly distributed load and material properties were assumed during modelling. Furthermore, it will be taken that the beam/membrane is of uniform section.

For modelling of vibrations the material properties required are dimensions, mass, Poisson's ratio and elastic modulus (Harris 1988). Material properties are that of the skeletal material and not the entire sample. Dimensions were approximated from analysed XMT pore size data. Skeletal density was obtained from helium pycnometry, Poisson's ratio was approximated from knowledge of materials and elastic modulus was taken to be that as extrapolated to zero porosity using an exponential fit as discussed in section 5.1.3. Zero porosity (as detectable by XMT) was assumed for the skeletal material.

For the beam model the edge condition used was one end being fixed and the other free to vibrate. Three edge conditions were considered for the membrane model, those being clamped all round the edge, clamped in the centre and free vibrating. All edge conditions were evaluated due to the difficulties approximating exact conditions during fracture. Diagrams showing the discussed vibration conditions can be seen in Figure 6.2.

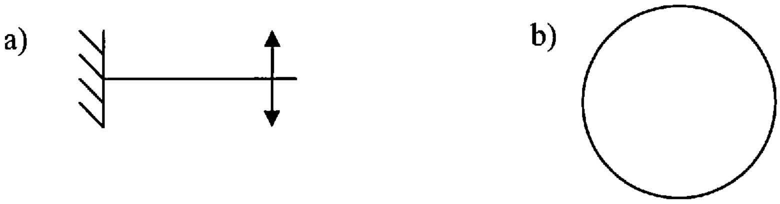

Beam fixed at one end

Free vibrating membrane

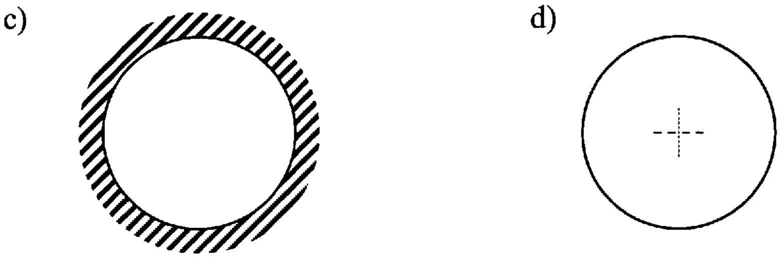

Membrane fixed at edges

Membrane fixed at centre

Figure 6.2: Diagrams showing vibration model shapes and edge conditions.

The natural vibration frequencies of a beam are given by (Harris 1988);

$$\omega_n = A\sqrt{\frac{EI}{\mu l^4}} \qquad [6.1]$$

where ω_n is the angular natural frequency, E is the elastic modulus, I is the area of inertia of the beam cross-section, l is the length of the beam, μ is the mass per unit length of the beam and A is the vibration co-efficient dictated by vibration mode and edge conditions. The first (lowest frequency) mode of vibration was considered. With the pore wall being modelled as a beam fixed at one end, A = 3.52 (Harris 1988). Area of inertia, I , is (Harris 1988);

$$I = \frac{bh^3}{12} \qquad [6.2]$$

where b is beam width and h is the beam height. Natural angular frequency was converted to vibration frequency by dividing by 2π.

The three edge conditions considered for membrane vibration, shown in Figure 6.2, obey a similar equation to give natural frequency of vibration with differences being determined by the vibration co-efficient, B. The equation is (Harris 1988);

$$\omega_n = B\sqrt{\frac{Et^2}{\rho a^4(1-\upsilon^2)}} \qquad [6.3]$$

where t is the thickness of the membrane, ρ is the mass density, a is the diameter of the circular membrane and υ is Poisson's ratio. For a free vibrating membrane B is 6.09, when the membrane is clamped at the edge B is 11.84 and if it is clamped in the centre B is 4.35.

6.4. Vibration Modelling

Approximate beam and membrane geometries were estimated from the microstructural experimental measurements. Figure 6.3 details likely fracture for a sample with same size uniformly distributed spherical pores. Geometric approximations were taken assuming this fracture path. However, it must be remembered that the true situation and porosity is much more complex. It has been assumed, as detailed in Figure 6.3, fracture occurs halfway along pore walls/membranes. Possible membrane diameters (a) with possible anchor points, beam length (l) and membrane thickness/beam height (t/b) are all shown. Beam width (b) is not detailed on Figure 6.3 but was approximated as between half and full pore diameter.

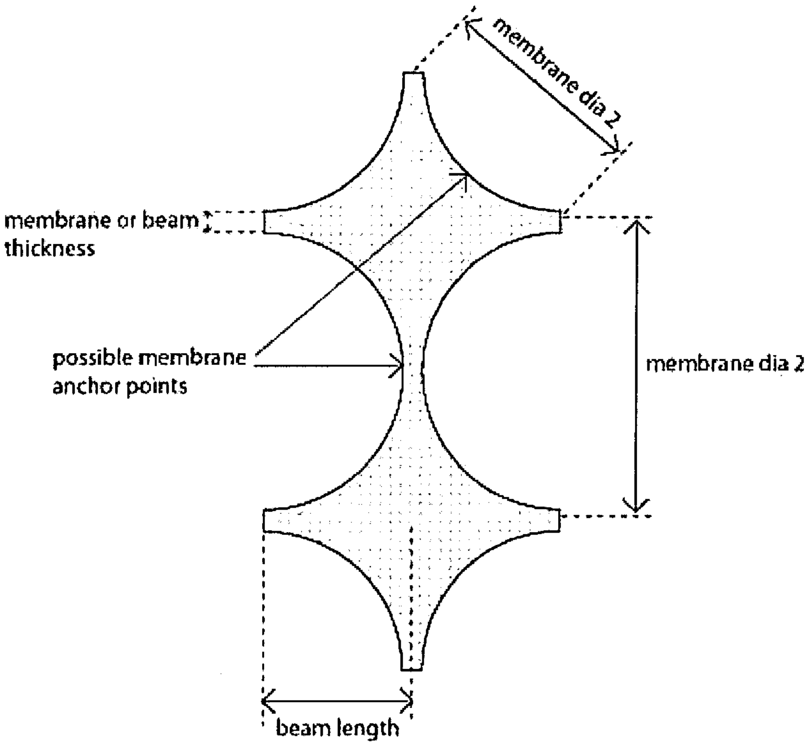

Figure 6.3: Pore geometries in 2-D when pores are assumed spherical. Solid section is shown as the shaded region. The edges are predicted fracture points. Possible geometries for vibration modelling are shown.

Using this diagram, and the measured pore characteristics of pore size and average pore wall thickness, maximum and minimum required pore geometries were approximated. A pore diameter range of 0.13mm to 1.75mm and pore wall range of 0.07mm to 0.13mm were used. Table 6.1 lists the calculated maxima, minima and mid-point for the pore geometries. Model frequencies were calculated using mid-point values on the premise this would produce the most probable vibration frequency. Using maximum and minimum vibration frequency conditions would produce extreme frequencies unlikely to be seen in real conditions and are therefore not representative. The decided pore geometry sizes were input to equations [6.1] and [6.2]. Poisson's ratio was taken as 0.33, normally a reasonable assumption for polymeric foams, estimated from foams with a wide range of densities (Agbisit, Alavi et al. 2007).

Table 6.1: Range of values predicted for the vibration modelling geometries along with the mid-point of the assumed range.

	Minimum (mm)	Maximum (mm)	Mid values (mm)
Beam height (h)	0.07	0.13	0.10
Beam width (b)	0.07	1.75	0.91
Beam length (l)	0.07	0.88	0.47
Membrane thickness (t)	0.07	0.13	0.10
Membrane diameter (a)	0.07	1.75	0.91

Table 6.2 presents the vibration frequency results for the beam and membrane models using the edge conditions described earlier and the mid-range values of approximate fracture geometries assuming spherical pores. The geometries and edge conditions will be more complex in reality and could serve to slightly increase or decrease the vibration frequency.

Table 6.2: Frequencies calculated from vibration modelling of pore walls using different edge conditions and selected geometries.

Edge condition	Frequency (kHz)
Beam (1st node)	3.69
Membrane (centre clamp)	5.08
Membrane (edge clamp)	13.83
Membrane (free vibrate)	6.90

6.4.1. Discussion

When looking at the calculated vibration frequencies it has to be remembered that these are models and not exact. Furthermore, the real life edge conditions will be more complex altering the vibration frequency to some extent. However, the first point to be noted is that the modelled vibration frequencies fall into the frequency range in which acoustic emission peaks were seen during analysis. This is strong evidence for pore walls being responsible for the acoustic vibrations during mechanical destruction. This is not to say that fracture piece vibrations do not contribute to the acoustic signal, but within the audible range studied it is likely due to vibrations of pore walls/membranes.

If we look at the higher volume fraction samples they have more acoustic energy in the 1200-2000Hz region whilst the lower volume fraction samples have more acoustic energy in the 3000-4300Hz range. If we think about these from the point of view of vibratory component, as discussed previously, it is likely the higher volume fraction samples have more strut like elements whilst the lower volume fraction samples have more membrane like components.

Results for the vibration modelling show beams will vibrate at lower frequencies than membranes. The predicted frequency for beams was 3.7kHz whilst membrane structure frequency was predicted at 6.90kHz. Extrudates predicted to have membrane structures show stronger frequency peaks between 3-4.3kHz, fitting more to the modelled beam frequency. However, the reality of the shapes and edge conditions mean these exact frequencies are not important, and being in the correct frequency range is good.

Looking deeper into the data, structures expected to have more beam-like components have increased lower frequency (1200-2000Hz) vibrations and reduced higher frequency (3000-4300Hz) vibrations, whilst structures expected to have more membrane-like features had increased higher frequency (3000-4300Hz) vibrations and reduced lower frequency (1200-2000Hz) vibrations. Vibration modelling showed beams will vibrate at lower frequencies than membranes. This provides strong evidence that frequency peaks come from vibrations of pore walls operating as membranes or beams; as volume fraction porosity decreases the structure moves from struts to membranes.

If true there are only finite frequency ranges in which extrudates of the same skeletal material but different structure can have vibration frequencies. Struts, predominant in extrudates with high volume fraction porosity, vibrate in the frequency range of 1200-2000Hz whilst membranes, predominant in extrudates with low volume fraction porosity, vibrate in the frequency range of 3000-4300Hz. This also implies that the pore structure is constructed from a few basic geometries and edge conditions, formed during expansion and subsequent fracture, and that changing the porosity changes the relative contributions of these basic building units.

Figure 4.21 indicates some differences at other frequencies. This may be due to additional pore geometries not seen in other samples.

In future work it may be possible to build up a complex fracture and vibratory model of the pore structures of extrudates and prove the predicted frequencies are very similar to those seen in the frequency spectra. This would likely be a combination of the models used and could use the 3-D structure generated during XMT. As further evidence to the analysis it would be interesting to obtain a pore wall thickness distribution. This might reveal modal peaks at a few pore wall thicknesses which correspond to the geometries for vibration at the said frequencies. This is achievable through granulometry but was not within the scope of this work and should be considered in the future. Furthermore, the fact that acoustic emissions originate from pore wall vibrations is consistent with the observation that bulk geometry has no effect on sample acoustic emissions. This means different geometry samples can be compared directly.

7. CONCLUSIONS AND FUTURE WORK

This project has studied a wide range of topics, covering analysis of mechanical destruction acoustic emissions, to mechanical properties of food, to the extrusion process itself. The initial stage literature review looked at work on acoustic emissions in the food industry, structural characterisation and extrusion expansion. Following findings from this review theseobjectives were set out for the work;

1. Develop a fully tested mechanical destruction acoustic capture method including investigation of peak origins in the frequency spectra and sample geometry effect.
2. Develop methods for the characterisation of internal extrudate (pore) structure.
3. Develop and test a method for controlling extrusion expansion that has no impact on extrudate skeletal material properties.
4. Investigate the relationships between mechanical measures (real and texture), mechanical destruction acoustic emissions and pore structure.
5. Establish whether pore wall vibrations can account for mechanical destruction acoustic emissions by modelling their vibration.

All of which were completed through the duration of the project.

A suitable method for both the capture and analysis of mechanical destruction acoustic emissions has been developed incorporating the use of a blunt blade attachment to have both compressive and bending forces during fracture. From the literature review it was decided that fundamental acoustic parameters should be initially focussed upon to reduce confusion, those being frequency spectra, total signal energy, maximum sound pressure and ring down count (RDC). These parameters were calculated and applied to further analysis through the project. During method development it was shown that acoustic emission frequency peaks are (likely) to come from extrudate sample fracture and that bulk geometry has no impact on mechanical destruction acoustic emissions; meaning different geometry samples can be compared directly.

Methods for structural characterisation were also developed. Application of a 3-D watershed algorithm was shown to be a suitable method for segmenting connected pores. Pore sizes could then be taken direct from this segmented image. Image analysis of 2-D images was shown to be accurate for measuring average pore wall thickness and density analysis was the optimum method for obtaining volume fraction; helium pycnometry was shown to provide reliable measurement of extrudate skeletal material.

Extrusion expansion was controlled via the use of an Expansion Control Chamber (ECC) which alters the pressure at the extruder external die face; hence pressure differential across the die face and flash-off of steam causing expansion. Results showed that the theory upon which the ECC was based is sound. Temperature profiles, extrusion pressures and skeletal densities showed the ECC to have no significant impact on skeletal material of the extrudate, whilst structural characterisation demonstrated the ECC varied volume fraction porosity and average pore wall thickness in a controlled manner. However, pore size was not controlled. This means the ECC can be used to produce products of different expansion but same skeletal material as it was during this project, ultimately meaning expansion and pore wall thickness can be singled out for investigating their effect on other sample attributes.

Using the samples with different volume fraction porosity and different average cell wall thickness, maximum stress in the texture test was shown to be driven primarily by volume fraction porosity, as was elastic modulus; both increase as volume fraction decreases. It is hypothesised this is due to the amount of solid material to fracture. Trends identified here fit well with previous work. An exponential model was adequate for describing the elastic modulus versus volume fraction data and used to approximate skeletal material elastic modulus at 1.48GPa (which was subsequently used for vibration modelling). Crispness 1 was shown to be marginally affected by volume fraction and average pore wall thickness; however, number of pores along the axis of compression is thought to be the controlling parameter for crispness 1. The

ECC can be used to control elastic modulus and maximum stress. Furthermore, if volume fraction is altered during normal production it will affect maximum stress and elastic modulus as outlined.

Acoustic emissions were shown to probably come from pore wall vibrations. This was proved using approximate models which produced fundamental vibrations falling in the region in which frequency peaks were seen. Through this analysis it has been suggested that, for these particular extrudates and skeletal material, as volume fraction porosity decreases the structure changes from strut like components to more membrane based. This in turn enhances the peak intensities from low volume fraction porosity samples in the frequency range of 3000-4300Hz. Conversely high volume fraction porosity samples show increased activity in the 1200-2000Hz frequency range. Modelling showed membranes to vibrate at higher frequencies than struts. This in turn relates back to elastic modulus and maximum stress. However, the changes in acoustic emission are small and only in relative peak intensity, so their sensory value is currently unknown. RDC has been shown to correlate reasonably with crispness 1 and it has been hypothesised will be correlated well with sensory crispness.

Through acoustic analysis and literature review certain acoustic parameters have been shown to hold important information. Other work has shown maximum sound pressure to be important and this may be the case with extrudate acoustic emissions if more than pore structure is altered. Results from this work and elsewhere have shown the frequency spectra to hold important information. Acoustic signal energy can be important but the relevant frequencies where differences are seen must be focussed on so as not to be drowned out by other signal characteristic frequencies. Finally, RDC holds important information.

The results of this project have bought the possibility of designing extrudates to have specific mechanical and acoustic properties closer, with volume fraction porosity and pore wall thickness being key parameters. There is also evidence that recipe (from testing entirely different products) will have a large(r) impact on acoustic emission frequency spectra. This fits with suggestions by Lillford (Lillford 2000) that acoustic emissions and mechanical properties are determined by both pore structural geometry and the nature of the skeletal material.

From this project there are many avenues that can be pursued with future work. The two areas where extra detail could be obtained are with the relationship of elastic modulus to volume fraction porosity and relationship of RDC to both sensory and mechanical crispness. To expand upon both these areas much larger data sets would be required and could then be used to strengthen analysis done through this work.

When considering the design of products with specific acoustic and mechanical properties two avenues could be pursued. Due to excess cost it is unlikely the ECC will be widely used in production. For this reason it would be suggested that the effect of extrusion conditions on extrudate structure firstly be reviewed and then investigated in detail. With extrusion having so many variables this would be a complex piece of work and would require a good experimental design to harness all information required. From this work targeted pore structures could be obtained.

The second option would be one similar to this but considering the effect of recipe on mechanical and acoustic properties. This would consider all acoustic properties, mechanical properties and look at the elastic modulus of the skeletal material for vibration modelling. A holistic view of acoustic differences that can be achieved through pore structure and material properties would then be provided. For this reason this would be the advised initial path of future work.

Also, at present the frequency spectra have only been considered in a qualitative manner. Since there is plentiful evidence that the frequency spectra contain useful information it may make sense to investigate how the most useful quantitative information can be extracted from the signal. Liu and Tan (Liu and Tan 1999) suggested a method for quantification of the frequency spectra that could form a good starting point for future work. Relationships could then be built to mechanical properties, but more importantly pore-structure for its ultimate control.

The impact of the small acoustic difference seen with different structure could also be considered from a sensory perspective. This is clearly an important piece of work to be conducted at some point in the future, probably after the impact of recipe on acoustic emissions has been established. This essentially verifies the usefulness of the data for product acoustic design; if the acoustic difference are not considered important by the consumer it has no relevance in product design. Ultimately mastication acoustics and their relation to previously generated data could be considered.

8. ACKNOWLEDGEMENTS

This work was funded by The WALTHAM Centre for Pet Nutrition. I would like to sincerely thank both Prof. Alan Atkinson and Dr Scott McGrane for their valuable tutelage during the project. Without them the project would not have been possible. Additional assistance was seen from Dr Robert C Atwood and Prof. Peter D. Lee (Imperial CollegeLondon), Torsten Trampe (Mars Inc.) and numerous members of the Mars Inc. team responsible for sponsoring this project, too many to name in person. Support from friends and colleagues in the Materials Department, and Imperial College in general, has not gone unnoticed. I would finally like to thank my family, girlfriend and cats for putting up with me in (occasional) times of frustration and difficulty.

9. REFERENCES

Ablett, S. (1992). "Overview of NMR Applications in Food Science." Trends in Food Science and Technology **3**: 246-248.

Agbisit, R., S. Alavi, et al. (2007). "Relationships between microstructure and mechanical properties of cellular corn starch extrudates." Journal of Texture Studies **38**: 199-219.

Al Chakra, W., K. Allaf, et al. (1996). "Characterisation of Brittle Food Products: Applications of the Acoustical Emission Method." Journal of Texture Studies **27**: 327-348.

Atwood, R. C., J. R. Jones, et al. (2004). "Analysis of pore interconnectivity in bioactive glass foams using X-ray microtomopgraphy." Scripta Materialia **51**: 1029-1033.

Babin, P., G. Della Valle, et al. (2005). "Mechanical properties of bread crumbs fromtomography based Finite Element simulations." Journal of Materials Science **40**: 5867-5873.

Barnsley, M. F. (1993). Fractals Everywhere. Boston, Academic Press: 171.

Barrett, A. H., A. V. Cardello, et al. (1994). "Cellularity, Mechanical Failure and Textural Perception of Corn Meal Extrudates." Journal of Texture Studies **25**: 77-95.

Bhatnagar, S. and M. A. Hanna (1996). "Effect of talc on properties of corn starch extrudate." Starch/Starke **48**(94-101).

Bouvier, J. M., R. Bonneville, et al. (1997). "Instrumental Methods for the Measurement of Extradite Crispness." Agro-Food Industry Hi-Tech(January/February): 16-19.

Briggs, G. A. (1967). About Your Hearing, Rank Wharfedale.

British Standard BS EN 843-2 (2006). "Advanced technical ceramics - Mechanical properties of monlithic ceramics at room temperature - Part 2: Determination of Young's modulus, shear modulus and Poisson's ratio." British Standard: BS EN 843-2:2006.

Brochettie, D. and M. P. Penfield (1992). "Speech Analysis Techniques: A Potential Model for the Study of Mastication Sounds." Journal of Texture Studies **23**: 111-138.

Campbell, G. M. and E. Mougeot (1999). "Creation and characterisation of aerated food products." Trends in Food Science and Technology **10**: 283-296.

Chen, J., C. Karlsson, et al. (2005). "Acoustic envelope detector for crispness assessment of biscuits." Journal of Texture Studies **36**: 139-156.

Cheng, E. M., S. Alavi, et al. (2007). "Mechanical-acoustic and sensory evaluations of cornstarch-whey protein isoltae extrudates." Journal of Texture Studies **38**: 473-498.

Chinnaswamy, R. (1993). "Basis of Cereal Starch Expansion " Carbohydrate Polymers **21**: 157-167.

Dacremont, C. (1995). "Spectral Composition of Eating Sounds Generated by Crispy Crunchy and Crackly Foods." Journal of Texture Studies **26**: 27-43.

Dacremont, C. and B. Colas (1993). "Effect of Visual Clues on Evaluation of Bite Sounds of Foodstuffs." Sciences Des Aliments **13**: 603-610.

Ding, Q. B., P. Ainsworth, et al. (2003). "The Effect of Extrusion Conditions on Functional and Physical Properties of Wheat-based Expanded Snacks." Journal of Food Engineering **73**: 142-148.

Drake, B. K. (1963). "Food Crushing Sounds. An Introductory Study." Journal of Food Science **28**: 233-241.

Duizer, L. M. (2001). "A Review of Acoustic Research for Studying the Sensory Perception of Crisp, Crunchy and Crackly Textures." Trends in Food Science and Technology **12**: 17-24.

Edmister, J. A. and Z. M. Vickers (1985). "Instrumental Acoustical Measures of Crispness in Foods." Journal of Texture Studies **16**: 153-167.

Elmoutaouakkil, A., L. Salvo, et al. (2002). "2D and 3D Characterisation of Metal Foams Using X-ray Tomography." Adbanced Engineering Materials **4**(10): 803-807.

Falcone, P. M., A. Baiano, et al. (2005). "Three-dimensional Quantitative Analysis of Bread Crumb by X-ray Microtomography." Journal of Food Science **70**(3): 265-272.

Fan, J. T., J. R. Mitchell, et al. (1994). "A computer simulation of the dynamics of bubble growth and shrinkage during extrudate expansion." Journal of Food Engineering **23**(3): 337-356.

Fang, Q. and M. A. Hanna (2000). "Functional properties of polylactic acid starch-based loose-fill packaging foams." Cereal Chemistry **77**(6): 779-783.

Farber, L., G. Tardos, et al. (2003). "Use of X-ray tomography to study porosity and morphology of granules." Powder Technology **132**: 57-63.

Gao, X. and J. Tan (1996). "Analysis of expanded-food texture by image processing. Part II. Mechanical properties." Journal of Food Process Engineering **19**: 445-456.

Gibson, L. G. and M. F. Ashby (1997). Cellular Solids: Structure and Properties. Cambridge, UK., Cambridge University Press.

Gondek, E., P. P. Lewicki, et al. (2006). "Influence of water activity on the acoustic properties of breakfast cereal." Journal of Texture Studies **37**: 497-515.

Guirao, M. and S. S. Stevens (1964). "Measurement of Auditory Density." Journal of the Acoustical Society of America **36**: 1176-1182.

Guy, R. (2001). Extrusion Cooking - Technologies and Applications, Woodhead Publishing.

Haralick, R. M., K. Shanmugam, et al. (1973). "Textural Features for Image Classification." IEEE Transactions on Systems, Man, and Cybernetics **SMC-3**(6): 610-621.

Harris, C. M. (1988). Shock and Vibration Handbook, McGraw-Hill Book Company.

Hayter, A. L. and A. C. Smith (1988). "The mechanical properties of extruded food foams." Journal of Materials Science **23**: 736.

Hermansson, A., M. Langton, et al. (2000). "New Approaches to Characterizing Food Microstructures." MRS Bulletin: 30-36.

Hicsasmaz, Z. and J. T. Clayton (1992). "Characterization of pore structure of starch based food materials." Food Structure **11**: 115.

Hicsasmaz, Z. and J. T. Clayton (1992). "Characterization of the pore structure of starch based food materials." Food Structure **11**: 115-132.

Jones, D., R. Chinnaswamy, et al. (2000). "Physiochemical properties of ready-to-eat breakfast cereal." Cereal Foods World **45**: 164-168.

Jones, J. R., P. D. Lee, et al. (2004). "Hierarchical Porous Materials For Tissue Engineering." Phil. Trans. A **364 (1838)**: 263-281.

Juodeikiene, G. and L. Basinskiene (2004). "Non-destructive texture analysis of cereal products." Food Research International **37**: 603-610.

Kalab, M., P. Allan-Wojtas, et al. (1995). "Microscopy and Other Imaging Techniques in Food Structure Analysis." Trends in Food Science and Technology **6**: 177-186.

Kapur, K. K. (1971). "Frequency Spectrographic Analysis of Bone Conducted Chewing Sounds in Persons with Natural and Artificial Dentures." Journal of Texture Studies **2**: 50-61.

Karathanos, V. T. and G. D. Saravacos (1992). "Porosity and Pore Size Distribution of Starch Materials." Journal of Food Engineering **18**: 259-280.

Kumagai, H., H. Kumagai, et al. (1993). "Critical Bubble Radius for Expansion in Extrusion Cooking." Journal of Food Engineering **20**(4): 325-338.

Lai, L. S. and J. L. Kokini (1990). "The Effect of Extrusion Operating Conditions on the On-line Apparent Viscosity of 98% Amylopectin (Amioca) and 70% Amylose (Hylon 7) Corn Starches during Extrusion." Journal of Rheology **34**(8): 1245-1266.

Lee, S. Y. and K. L. McCarthy (1996). "Effect of Screw Configuration and Speed on RTD and Expansion of Rice Extrudate." Journal of Food Process Engineering **19**(2): 153-170.

Lee, W. E., A. E. Deibel, et al. (1988). "Analysis of Food Crushing Sounds During Mastication: Frequency-Time Studies." Journal of Texture Studies **19**: 27-38.

Lee, W. E., M. A. Schweiter, et al. (1990). "Analysis of Food Crushing Sounds During Mastication: Total Sound Level Studies." Journal of Texture Studies **21**: 165-178.

Lillford, P. J. (2000). "The Materials Science of Eating and Food Breakdown." MRS Bulletin **December**: 38-43.

Lim, K. S. and M. Barigou (2004). "X-ray micro-computed tomography of cellular food products." Food Research International **37**: 1001-1012.

Liu, X., C. S. L. Chuah, et al. (2002). "Compressive Elastic Modulus and its Relationship to the Structure of Hydrated Starch Foam."

Liu, X. and J. Tan (1999). "Acoustic Wave Analysis for Food Crispness Evaluation." Journal of Texture Studies **30**: 397-408.

Lund, F. (1998). "Sound and Fracture." Material Science **279**(5357): 1652-1653.

Maire, E., A. Elmoutaouakkil, et al. (2003). "In Situ X-Ray Tomography Measurements of Deformation in Cellular Solids." MRS Bulletin: 284-289.

Maire, E., A. Fazekas, et al. (2003). "X-ray tomography applied to characterization of cellular materials. Related finite element modeling problems." Composites Science and Technology **63**: 2431-2443.

Mangan, A. P. and R. T. Whitaker (1999). "Partitioning 3D Surface Meshes Using Watershed Segmentation." IEEE Transactions on Visualization and Computer Graphics **5**(4): 308-321.

McGrane, S. (2000). "Starch State and Extrusion Cooking." Internal masterfoods industry report produced during Scott McGranes work.

McGrane, S. (2002). "The Relationship Betwen Cat Mastication Acoustic Emissions and Mechanical Destruction Acoustic Emissions." Mars Inc. Confidential Report.

McGrane, S. (2004). "Validation of Extrudate Texture Methodologies." Mars Inc. Confidential Report.

Mohamed, A. A. A., R. Jowitt, et al. (1982). "Instrumental and Sensory Evaluation of Crispness : 1. In Friable Foods." Journal of Food Engineering **1**: 55-75.

O'Brien, J. (1992). "NMR Applications in Food Research." Trends in Food Science and Technology **3**: 177-178.

Owusu-Ansah, J., F. R. Van de Voort, et al. (1983). Cereal Chemistry **60**: 319-324.

Pabst, W., E. Gregorova, et al. (2006). "Elasticity of porous ceramics - a critical study of modulus-porosity relations." Journal of the European Ceramic Society **26**(7): 1085-1097.

Piazza, L., J. Gigli, et al. (2006). "On the application of chemometrics for the study of acoustic-mechanical properties of crispy bakery products." Chemometrics and Intelligent Laboratory Systems **86**: 52-59.

Plews, A. G. (2003). "An Investigation into the Effect of Extruded Food Product Diameter on the Acoustic Emission Produced during both Mechanical Destruction and Mastication." Mars Inc. Confidential Report.

Rice, R. W. (1998). Porosity of Ceramics. New York, Marcel Dekker.

Roudaut, G., C. Dacremont, et al. (1998). "Influence of Water on the Crispness of Cereal Based Foods: Acoustic, Mechanical and Sensory Studies." Journal of Texture Studies **29**: 199-213.

Ryu, G. H. and C. E. Walker (1995). "The Effect of Extrusion Conditions on the Physical Properties of Wheat Flour Extrudates." Starch/Starke **47**(1): 33-36.

Seymour, S. K. and D. D. Hamann (1998). "Crispness and Crunchiness of Selected Low Moisture Foods." Journal of Texture Studies **19**: 79-95.

Sherman, P. and F. S. Deghaidy (1978). "Force-Deformation Conditions Associated with the Evaluation of Brittleness and Crispness in Selected Foods." Journal of Texture Studies **9**: 437-459.

Shiffman, S. (1977). "Food Recognition by the Elderly." Journal of Gerontology **32**: 586-592.

Speaks, C. E. (1999). Introduction to Sound. San Diego, Singular Publishing: 2-43, 155.

Srisawas, W. and V. K. Jindal (2003). "Acoustic testing of snack food crispness using neural networks." Journal of Texture Studies **34**: 401-420.

Stock, S. R. (1999). "X-ray microtomography of materials." International Materials Reviews **44**(4): 141-164.

Sun, H., J. Yang, et al. (2004). "A fast watershed algorithm based on chain code and its application in image segmentation." Pattern Recognition Letters **26**: 1266-1274.

Taniwaki, M., T. Hanada, et al. (2006). "Device for acoustic measurement of food texture using a piezoelectric sensor." Food Research International **39**: 1099-1105.

Tek, H. and H. C. Aras (2004). "Local watershed operators for image segmentation." MICCAI: 127-134.

Tesch, R., M. D. Normand, et al. (1996). "Comparison of the Acoustic and Mechanical Signatures of Two Cellular Crunchy Cereal Foods at Various Water Activity Levels." Journal of Science in Food and Agriculture **70**: 347-354.

Thymi, S., M. K. Krokida, et al. (2005). "Structural Properties of Extruded Corn Starch." Journal of Food Engineering **68**: 519-526.

Trater, A. M., S. Alavi, et al. (2005). "Use of non-invasive X-ray microtomograhy for characterising microstructure of extruded biopolymer foams." Food Research International **38**: 709-719.

van Dalen, G., H. Blonk, et al. (2003). "3-D Imaging of Foods Using X-Ray Microtomography." G.I.T. Imaging and Microscopy.

Van Hecke, E., K. Allaf, et al. (1995). "Texture and structure of crispy-puffed food products. I: Mechanical properties in bending." Journal of Texture Studies **26**: 11-25.

Van Vliet, T. (2002). "On the Relation Between Texture Perception and Fundamental Mechanical Parameters for Liquids and Time Dependant Solids." Food Quality and Preference **13**: 227-236.

Vickers, Z. M. (1985). "The Relationship of Pitch, Loudness and Eating Technique to Judgements of the Crispness and Crunchiness of Food Sounds." Journal of Texture Studies **16**: 85-95.

Vickers, Z. M. and M. C. Bourne (1976). "A Psychoacoustical Theory of Crispness." Journal of Food Science **41**: 1158-1164.

W Al Chakra, K. A., A B Jermai (1996). "Characterisation of Brittle Food Products: Applications of the Acoustical Emission Method." Journal of Texture Studies **27**: 327-348.

Wilkinson, C., G. B. Dijksterhuis, et al. (2000). "From Food Structure to Texture." Trends in Food Science and Technology **11**: 442-450.

William, R. V. (1980). Acoustic Emission. Bristol, Adam Hilger Ltd.